國 立 交 通 大 學

光電工程研究所

博士論文

具氮化鎵與氮化鋁布拉格反射鏡之氮化鎵面射型雷射之研究

Study of GaN-based Surface Emitting Lasers with AlN/GaN Distributed Bragg Reflectors

研 究 生：陳　士　偉　　Student: Shih-Wei Chen

指導教授：郭　浩　中　　Advisor: Hao-Chung Kuo

盧　廷　昌　　Tien-Chang Lu

中華民國 九十九 年 八 月

具氮化鎵與氮化鋁布拉格反射鏡之氮化鎵面射型雷射之研究

Study of GaN-based Surface Emitting Lasers with AlN/GaN Distributed Bragg Reflectors

研 究 生：陳 士 偉　　Student：Shih-Wei Chen

指導教授：郭 浩 中　　Advisor：Hao-Chung Kuo

盧 廷 昌　　Tien-Chang Lu

國立交通大學

光電工程研究所

博 士 論 文

A dissertation
Submitted to Institute of Electro-Optical Engineering
College of Electrical Engineering and Computer Science
National Chiao Tung University
In Partial Fulfillment of the Requirements
For the Degree of
Doctor in Philosophy
Electro-Optical Engineering
August 2010
Hsin-chu, Taiwan, Republic of China

中 華 民 國 九 十 九 年 八 月

具氮化鎵與氮化鋁布拉格反射鏡之氮化鎵面射型雷射之研究

研究生：陳士偉　　　　　　　　　　指導教授：郭浩中　教授

盧廷昌　教授

國立交通大學光電工程研究所

摘要

過去幾十年來，由於氮化鎵材料具有直接能隙與強鍵結力等優點，因此吸引許多學界與業界的目光並且廣泛的製作成各種光電元件，如發光二極體、雷射二極體與光偵測器等，並且應用於日常生活中的照明、光儲存、平面顯示及生物科技中。本論文旨在設計並製作具混合式布拉格反射鏡之電激發氮化鎵垂直型共振腔面射型雷射與具氮化鎵與氮化鋁布拉格反射鏡之光激發氮化鎵光子晶體面射型雷射。

首先，我們成功的製作出室溫電激發氮化鎵材料之垂直型共振腔面射型雷射。本雷射結構具有一組氮化鋁與氮化鎵布拉格反射鏡、七倍的光學波長與一組氧化物反射鏡。為了增加載子的復合效率與減少光之損耗，我們在七倍的光學波長共振腔中穿插一層氮化鋁鎵電子阻擋層與一層約 30 nm 的極薄 ITO 薄膜層，兩層結構均位於多重量子井的上方。本雷射在室溫所量測出來的臨界電流為 9.7 mA，相對應之臨界電流密度約 12.4 kA/cm^2，其輻射波長為 412 nm 且半高寬約 0.5 nm。極化程度與雷射發散角分別為 55 %與 8 度。在 CCD 影像中，本雷射光點約為 2 μm，原因在於 InGaN 材料本身的不均勻特性所導致。此外，自發輻射耦合效率約為 5*10^{-3}，此結果與一般的邊射型雷射相比約高達 100 倍之高，代表其效率被微共振腔結構大幅提高。

其次，我們也成功的製作出具有單一雷射模態與較小雷射發散角之光激發氮化鎵光子晶體面射型雷射。藉由設計不同週期的光子晶體結構(190 nm-300 nm)，這些光子晶體雷射元件出射之雷射波長範圍可從 395 nm 調變到 425 nm。利用平面波展

開法模擬其 TE 能帶圖與布拉格理論，本雷射結構所激發出的雷射波長所相對應之正規化頻率正好相對於 TE 能帶圖三個能帶邊界(Γ1，K2，M3)，而從極化方向也可證實雷射模態確實存在此三個能帶邊緣模態。從變角度光致發光系統的量測中，我們得到雷射模態 Γ1，K2 及 M3 的雷射出射角度，相對於垂直方向，分別為 0°, 29° 及 59.5°，其雷射發散角分別為 1.2°, 2.5°及 2.2°。此外，Γ1 模態的雷射臨界操作功率均小於 K2 與 M3 模態，藉由二維耦合波模型所計算之雷射耦合係數，此結果可歸因於 Γ1 模態具有最大的雷射耦合係數。

由於氮化鎵垂直型共振腔面射型雷射與光子晶體面射型雷射具有許多優越的光學特性，我們相信此結構可以應用在可見光及藍紫光雷射等高功率、大範圍及多用途之光電元件中。

Study of GaN-based Surface Emitting Lasers with AlN/GaN Distributed Bragg Reflectors

Student: Shih-Wei Chen   Advisor: Dr. Hao-Chung Kuo
Dr. Tien-Chang Lu

Department of photonics & Institute of Electro-Optical Engineering
National Chiao-Tung University

Abstract

For several decades, GaN-based material has attracted much attention of academia and industry and widely used in several optoelectronic devices due to its wide direct bandgap and strong binding energy, such as light emitting diodes, laser diodes, and photon-detectors which can be applied in lighting, optical storage, display, and biotechnology. The thesis is focus on the design and fabrication of the electrically pumped GaN-based vertical cavity surface emitting lasers (VCSEL) with hybrid distributed Bragg reflectors and the optical pumped GaN-based photonic crystal surface emitting lasers (PCSEL) with AlN/GaN distributed Bragg reflectors.

First, we demonstrated an electrical pumped CW laser action on GaN-based VCSEL at room temperature. The laser structure consists of a 10-pair Ta_2O_5/SiO_2 distributed Bragg reflector (DBR), a 7 lamda-thick optical cavity, and a 29-pairs AlN/GaN DBR. To enhance the carrier coupling efficiency, an AlGaN electron blocking layer was inserted above the multi-quantum wells region, and a thinner ITO layer (30 nm) was used in the 7 lamda cavity. The laser has a threshold current 9.7 mA corresponding to threshold current density of about 12.4 kA/cm^2. The lasing wavelength is located at 412nm with a linewidth of about 0.5 nm. The degree of polarization and the laser beam divergence angle are about 55 % and 8 degree, respectively. In the CCD image, the laser spot size is about 2 μm contributed by the InGaN inhomogeneous characteristics. Besides, the spontaneous emission coupling factor is about $5*10^{-3}$. The value is 100 times larger than

the commercial edge emission lasers which means the efficiency is substantially enhanced by the micro cavity structure.

Second, we successfully fabricated the optical pumped GaN-based photonic crystal surface emitting lasers (PCSEL) with single mode emission and small divergence angle. By designing different photonic crystal lattice constants from 190 nm to 300 nm, different PCSELs with lasing wavelength ranging from 395 nm to 425 nm were achieved. According to the plane-wave expansion method and satisfied Bragg theory, the different lasing wavelengths can be attributed to the different band-edge modes, such as Γ1, K2, and M3. This result can be further confirmed by the polarization directions of these three band edge modes (Γ1，K2，M3). Moreover, from the angular-resolved μ-PL measurements, we can obtain the lasing angles of these modes normally from the sample surface are 0˚, 29˚, and 59.5˚, and the laser beam divergence angles are 1.2˚, 2.5˚, and 2.2˚. Furthermore, the threshold pumping power of Γ1 mode is smaller than that of K2 and M3 modes. This result can be attributed to the largest coupling coefficient calculated by the 2-D couple wave theory.

Due to these optical and electrical advantages of GaN-based VCSEL and PCSEL, we believe these laser devices can be applied to visible light and UV light lasers in high output power and multiple purposes of optoelectronic devices.

誌謝

時間過的真的很快，一轉眼，四年就過去了，到了畢業這一天，回憶一幕幕的在眼前浮現，經歷了很多事情，而每一件事情都讓我成長，真的很謝謝其中經歷過與幫助過我的每一個人。首先，很感謝老師們在這四年間願意細心教導我不論是實驗上或生活上的大小事。尤其是盧老師對於學術嚴謹的態度真的讓我深深佩服，願意花時間教導我種種問題，讓我在處理事情上更加的細心與謹慎，雖然有時還是粗線條居多，但是真的很謝謝老師的包容。而郭老師常常在深夜中穿梭於實驗室與我們的觸膝長談，聊聊研究中的苦悶與生活中的大小事，這些都讓我的博士生涯輕鬆許多。我也忘不了王老師那爽朗的笑聲總是在實驗室中出現，特別是在東京參加研討會時，晚上尋找居酒屋品嘗日本佳餚美酒還有吃拉麵時的情景，感覺人生不過就是如此暢快而已。

謝謝實驗室帶領我還有幫助過我的學長姐，小強、小朱、泓文、逸駿、小賴、李博、金博、鴻儒以及亞儒學長。其中小強、小朱、李博以及泓文學長常常幫助我解決研究上的難題。其中不乏有趣的回憶，如與小朱及小強夜衝貓空泡茶及宜蘭太平山的充電之旅，真的很棒。也很謝謝我的同學，明華、清華、宗鼎、志蒼、振昌、碩均及俊榮的幫忙，讓我能開心順利的度過博士生涯，不管如何，未來在外面一起努力吧^^。尤其是清華、明華及宗鼎，因為你們的陪伴與幫助，讓我能開心並且順利的完成學業，謝謝你們。參加日本東京奈米展的感覺更是記憶猶新，三人擠一張床，哈哈。在這之中一起努力過的學弟妹，可愛的小馬總是帶給我們歡笑，阿綱、金門、子維、哭哭、阿祥、嗡嗡、板弟、振弦、昀霖及幼齒，從你們身上我也學習到很多的東西，謝謝你們。還有鏡學、幸助、閔安、柏孝、小恬恬、小柯、政暐、玟君、依嚀、治凱及 QQ，因為你們，讓我的生活變得更多采多姿。

很感謝台大黃建璋老師、成大張守進老師、彰師大郭艷光老師以及李柏璁老師在口試時對我的指導，真的很謝謝你們的幫忙；很感謝長庚郭守義老師及賴芳儀學姐去上海時開會對我的照顧。各位老師、學長姐、同學們及學弟妹對我的照顧都讓我銘記在心，謝謝你們。

最後，很感謝我的家人，父母、兩位妹妹，爺爺奶奶、還有我們這個大家庭及八隻小狗。在這段時間中經歷了許多事情讓你們擔心了。但是因為有你們的支持，讓我能全心全力的完成博士班的學業，真的很謝謝你們。另外，這本書也獻給關心我愛我的每一個人，沒有你們，我是無法獨自完成這本論文，衷心的謝謝你們。

士偉　　于 99 年 8 月 16 日

交通大學光電所

CONTENTS

Abstract (in Chinese) I
Abstract (in English) III
Acknowledge V
Contents VII
List of figures IX

Chapter 1 Introduction 1
1-1 Wide-bandgap III-V materials 1
1-2 Nitride-based semiconductor lasers 2
1-2.1 Edge emitting lasers 3
1-2.2 Surface emitting lasers 5
1-3 Objective of the thesis...11
References. 13
Chapter 2 Design and Fabrication of VCSELs..15
2-1 Operation principle of semiconductor lasers 15
2-2 Distributed Bragg reflectors...23
2-2.1 Penetration depth... 24
2-2.2 Reflectance simulation of Ta_2O_5/SiO_2 and nitride-based DBRs 26
2-3 Design of GaN-based VCSELs...29
2-4 Fabrication of GaN-based VCSELs...34
2-4.1 Growth of nitride-based reflectors and micro-cavity......................... 34
2-4.2 Deposition of dielectric mirrors 39
References. 46
Chapter 3 Characteristics of Electrically Pumped GaN-based VCSELs.......47
3-1 Optical properties of GaN-based VCSELs 47
3-2 Characteristics of electrically pumped GaN-based VCSELs......................52
References. 64
Chapter 4 Design and Fabrication of PCSELs 68
4-1 Bragg diffraction theory..68

4-2 Couple wave theory 76
4-3 Design of GaN-based 2-D PCSELs 92
4-4 Fabrication of GaN-based PCSELs 94
Reference. 99
Chapter 5 Characteristics of Optical Pumped GaN-based PCSELs 102
5-1 Band-edge modes in dispersion curves 102
5-2 Threshold power characteristics with different coupling coefficients 112
5-3 Polarization characteristics at different band edge modes 117
5-4 Angular-resolved optical characteristics at different band-edge modes ...120
References. 127
Chapter 6 Conclusion and Futhre Work 128
6.1 Conclusion...128
6.2 Future work 129
Publication lists. 132

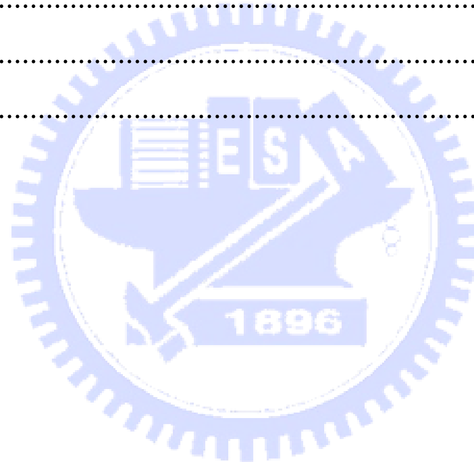

List of figures

Chapter 1

Figure 1. 1 The band-gap diagram of II-VI and III-V semiconductor materials. 2

Figure 1. 2 The schematic diagram of an edge emitting laser diode. 4

Figure 1. 3 The schematic diagram of a vertical-cavity surface emitting laser diode. 6

Figure 1. 4 Schematic diagrams of three nitride-based VCSEL structures. 9

Figure 1. 5 The band diagram of a 2-D triangular-lattice PhC structure. 10

Figure 1. 6 (a)The first InGaAsP photonic crystal defect laser structure and (b) The plane-view SEM image of single defect photonic crystal structure with hexagonal lattice...11

Chapter 2

Figure 2. 1 An illustration of output power vs. current for a diode laser......................... 18

Figure 2. 2 The internal photon number n_o versus the pump rate P as a function of the spontaneous emission coefficient β. 23

Figure 2. 3 A schematic diagram of DBRs 24

Figure 2. 4 Simulated reflectivity spectra of 5, 10, 15, and 25 pairs of AlN/GaN DBRs. 27

Figure 2. 5 Simulated reflectivity spectra of three different nitride-based DBRs with high reflectivity 28

Figure 2. 6 Simulated reflectivity spectra of 3, 5, and 8 pairs of Ta_2O_5/SiO_2 DBRs........ 29

Figure 2. 7 The simulation cavity structure 31

Figure 2. 8 The simulated reflectance spectra with different thickness of ITO................ 32

Figure 2. 9 the simulated cavity modes with different thickness of ITO.......................... 32

Figure 2. 10 The simulated quality factors with different thickness of ITO..................... 33

Figure 2. 11 Electric field intensity and refractive index as a function of the distance from top layer.. 34

Figure 2. 12 Cross-sectional TEM images of (a) the DBR sample and (b) one set of 5.5 pairs of GaN/AlN SL insertion layers.. 36

Figure 2. 13 AFM image of the DBR sample 37

Figure 2. 14 The reflectivity spectrum of the AlN/GaN DBR... 38

Figure 2. 15 (A) OM and (B) cross-sectional TEM images of the as-grown micro-cavity

sample. 39
Figure 2. 16 The reflectivity spectrum of the Ta_2O_5/SiO_2 DBR 40
Figure 2. 17 (A) Schematic diagram, (B) SEM image, and (C) OM images of the VCSEL structure. 41
Figure 2. 18 The process flowchart of nitride-based micro-cavity devices. 42
Figure 2. 19 The schematic diagram of the overall GaN-based VCSEL structure with hybrid mirrors. 42
Figure 2. 20 The absorption of the 30 nm-thick ITO layer 43
Figure 2. 21 I-V curve of the 30 nm ITO layer and the p-GaN layer 44
Figure 2. 22 OM images: (a) without current injection, (b) at 2 mA current injection, and (c) the array fabrication of the VCSEL devices. 45

Chapter 3

Figure 3. 1 The optical pumping setup 47
Figure 3. 2 PL emission spectra of as-grown sample and VCSEL structure, and the reflectivity spectrum of as-grown sample. 48
Figure 3. 3 The light emission intensity of the VCSEL as a function of the pumping energy density 50
Figure 3. 4 Emission spectrums under different pumping energy density 51
Figure 3. 5 The emission images under different pumping energy 51
Figure 3. 6 The coupling efficiency of spontaneous emission (β) 52
Figure 3. 7 The probe station measurement setup. 53
Figure 3. 8 The images of low temperature EL measurement system 54
Figure 3. 9 The lasing intensity as a function of injection current under different measurement temperature from 200 K (solid line), 240 K (dash line), 270 K (dot line), and 300 K (dot dash line). 55
Figure 3. 10 The voltage is a function of injection current at 200 K, 240 K, 270 K, and 300 K. 56
Figure 3. 11 The lasing intensity and the voltage as a function of injection current at 300 K. The threshold current and turn-on voltage are about 9.7 mA and 4.3 V. 57
Figure 3. 12 The emission spectra were recorded at injection current of 0.6 I_{th}, 1 I_{th}, and

1.2 I_{th}. 57
Figure 3. 13 The image shows the lasing spot with the diameter of about 2 μm below and above threshold current. 58
Figure 3. 14 Semi natural-logarithm plot of the dependence of the threshold pumping energy ($ln(I_{th})$) on the operation temperature. 59
Figure 3. 15 The lasing wavelength of GaN-based VCSEL as a function of temperature at 9 mA and 15 mA. 60
Figure 3. 16 The laser emission intensity versed injection current in logarithmic scale. The solid curve is the fitting curve. The β value is about 5×10^{-3}. 61
Figure 3. 17 The degree of polarization of VCSEL device is about 55 %. The solid line is the fitting curve. 62
Figure 3. 18 The laser divergence angle of about 8 degree was measured by the angular-resolved measurement system. 63

Chapter 4

Figure 4. 1 (a) The band diagram of photonic crystal with triangular lattice; (b) The schematic diagram of photonic crystal with triangular lattice in reciprocal space... 69
Figure 4. 2 Wave vector diagram at points (A), (B), (C) in Figure 4. 1(a); k_i and k_d indicate the incident and diffracted light wave. 70
Figure 4. 3 The wave vector diagram at point (A) in vertical direction. 71
Figure 4. 4 Wave vector diagram of (a) in-plane and (b) vertical direction at point (D); (c) wave vector diagram showing diffraction to an oblique direction at point (D)........ 72
Figure 4. 5 Wave vector diagram of (a) in-plane and (b) vertical direction at point (E) (or K2 mode); k_i and k_d indicate incident and diffracted light wave. 73
Figure 4. 6 Wave vector diagram of (a) in-plane and (b) vertical direction at point (F) (or M3 mode); k_i and k_d indicate incident and diffracted light wave............................ 74
Figure 4. 7 (a)Normalized far-field PL spectrum of the PhC-assisted QD structure; (b) Reciprocal lattice associated with the 2-D PhC and origin of extracted guided modes. The blue and gray circles indicate the light cone and the trace of points with identical $k_{//}$, respectively. The gray hexagon is the first Brillouin zone boundary.... 75
Figure 4. 8 2-D band structure of a PhC in the Γ-M direction; (b) Corresponding band

structure in a multimode waveguide: mode *m* gives rise to two PhC bands, Am and Bm. 76
Figure 4. 9 General multi-dielectric layers show the perturbation of refractive index and amplitude gain. $Z_1(x)$ and $Z_2(x)$ are two corrugated functions. 77
Figure 4. 10 A simple model used to explain Bragg conditions in a periodic waveguide. 78
Figure 4. 11 Schematic diagram of eight propagation waves in square lattice PC structure. 82
Figure 4. 12 Dispersion relationship for TE like modes, calculated using the 2-D PWEM 85
Figure 4. 13 Schematic diagram of six propagation waves in triangular lattice for Γ1 point. 86
Figure 4. 14 Schematic diagram of three propagation waves in triangular lattice for K2 point 88
Figure 4. 15 Schematic diagram of four propagation waves in triangular lattice for M3 point 90
Figure 4. 16 The lowest guided mode optical field distribution, where the confinement factor Γ_g=0.73 and n_{eff}=2.44. 93
Figure 4. 17 The band diagram of the 2-D triangular-lattice PhC structure on our sample structure. The value of *r*/*a* here is 0.28. 94
Figure 4. 18 The typical schematic diagram of EBL system. 95
Figure 4. 19 PCSEL fabrication flowcharts: (a) as-grown sample structure, (b) deposit SiNx film by PECVD, (c) spin on PMMA, (d)E-beam lithography, (e) PC patter transfer to SiN_x layer, (f) remove PMMA by Acetone, and (g) PC patterns transfer to GaN layer. 96
Figure 4. 20 The GaN-based PCSEL devices with AlN/GaN DBRs 97
Figure 4. 21 SEM images of PCSELs: (a) plane view. (b) cross-section view. 98

Chapter 5

Figure 5. 1 The angular-resolved μ-PL (AR μ-PL) system 103
Figure 5. 2 Reflectivity spectrum of the half structure with 35 pairs of GaN/AlN DBRs measured by N&K ultraviolet-visible spectrometer with normal incident at room

temperature. 104
Figure 5. 3 The u-PL spectrum of as-grown sample 104
Figure 5. 4 Laser intensity as a function of pumping energy density 105
Figure 5. 5 The lasing spectrums under different pumping energy densities 106
Figure 5. 6 (a) Normalized frequency as a function of the lattice constant. The solid circle points are the lasing wavelengths from the different PhC structures. (b) Calculated band diagram of the 2-D hexagonal-lattice structure. The dotted lines are guides for band edges. 108
Figure 5. 7 The lasing CCD image is at 1.3 E_{th} and the dash circle is the PhC nanostructure region of about 50μm 108
Figure 5. 8 The spontaneous emission coupling factor of GaN-based 2-D PCSEL 109
Figure 5. 9 The calculation schematic diagram and the plane-view SEM image 110
Figure 5. 10 Temperature dependence of the lasing threshold pumping energy (E_{th}). 111
Figure 5. 11 The far field pattern with different distance from the sample surface collected by objective lens 112
Figure 5. 12 The divergence angle between the two axes. 112
Figure 5. 13 Dispersion curve for TE like mode for Γ1 case...113
Figure 5. 14 Dispersion curve for TE like mode for K2 case 114
Figure 5. 15 Dispersion curve for TE like mode for M3 case 115
Figure 5. 16 The threshold power versus normalized frequency for Γ1 K2 M3 groups .116
Figure 5. 17 Normalized frequency verses *r*/*a* ratios. The solid, dot, and dash lines represent the simulation results of Γ, K, and M lasing groups by PWEM. The square points, inserted in the diagram, present the experiment results mapped and compared with the simulation results. 117
Figure 5. 18 (a) The measured polarization curves for different band edge lasers grouped into Γ(circle points and solid line), K(triangle points and dot line), and M(square points and dash line) boundaries calculated by the plane-wave expansion method. (b) The main polarization directions obtained in (a) and their corresponding diffracted laser beams, which are normal to the polarization directions in a K-space map corresponding to our hexagonal PhC lattice. 119
Figure 5. 19 The measured AR-PL diagram near the Γ1 mode ((a) pumped by YVO_4

pulse laser; (b) pumped by He-Cd laser), the dash lines represent the calculated photonic band dispersion curves. 122

Figure 5. 20(a) The enlarged dispersion curves near the Γ1 band edge. Labels (I) to (IV) correspond to four different Γ1 band edge modes. (b) (I)-(IV) are the magnetic field distributions in one unit cell for the band edge modes labeled in (a). Blue and green areas represent positive and negative magnetic fields perpendicular to the plane. dash circles indicate the PhC air holes.. 123

Figure 5. 21 The measured AR-PL diagram near the K2 mode ((a) pumped by YVO_4 pulse laser; (b) pumped by He-Cd laser). The dash lines represent the calculated photonic band dispersion curves. 124

Figure 5. 22 The measured AR-PL diagram near the M3 mode ((a) pumped by YVO_4 pulse laser; (b) pumped by He-Cd laser). The dash lines represent the calculated photonic band dispersion curves. 125

Figure 5. 23 The emission angles and divergence angles of Γ1, K2, and M3 band-edge modes on the normal plane from the sample surface.. 126

Chapter 6

Figure 6. 1 Electrical pumped of GaN-based VCSEL with optical and current confined layer 130

Figure 6. 2 (a) The image for EL GaN-based VCSELs with double dielectric mirrors; (b) the schematic diagram of EL GaN-based VCSELs with double dielectric mirrors.130

Figure 6. 3 (a) GaN-based photonic crystal defect laser; (b) electrically pumped GaN-based photonic crystal band-edge laser.. 131

Figure 6. 4 The schematic diagram of thin-GaN PCSEL devices 131

Chapter 1
Introduction

1-1 Wide-bandgap III-V materials

Over past decade, wide bandgap nitride materials have attracted great attention due to their promising potential for the applications of optoelectronic devices such as flat panel display, competing storage technologies, automobiles, general lighting, and biotechnology, and so on [1-5]. The III-N materials are synthesized mainly using the four kinds of atoms, gallium (Ga), nitride (N), aluminum (Al), and indium (In), to form the binary and ternary compounds such as GaN, InN, AlN, $In_xGa_{1-x}N$, and $Al_xGa_{1-x}N$ etc. The bandgap of these materials cover a very wide range from 0.9eV to 6.1eV (Figure 1. 1), which implies the large band off-set in hetero-structure could be achieved in this material system. The large band off-set is very useful to confine carrier for the high-speed and high power electronic devices and light emitting devices [6]. Their wide-range bandgap also provide possibility of full-color emission because they cover red, green, and blue emission regions. This property further makes nitride materials important and important for the applications of full-color display or solid-state lighting. Furthermore, nitride materials still have lots of advantages such as high bond energy (~2.3eV), high saturation velocity (~2.7×10^4 cm/s), high breakdown field (~2×10^6 V/cm), and strong excitonic energy (>50meV)[7,8]. Although wurtzite nitride compounds have some unique properties such as piezoelectric field and spontaneous polarization which is harmful to the efficiency of light emitting devices, the material system is a very strong candidate for the future optoelectronic applications due to their superior material properties.

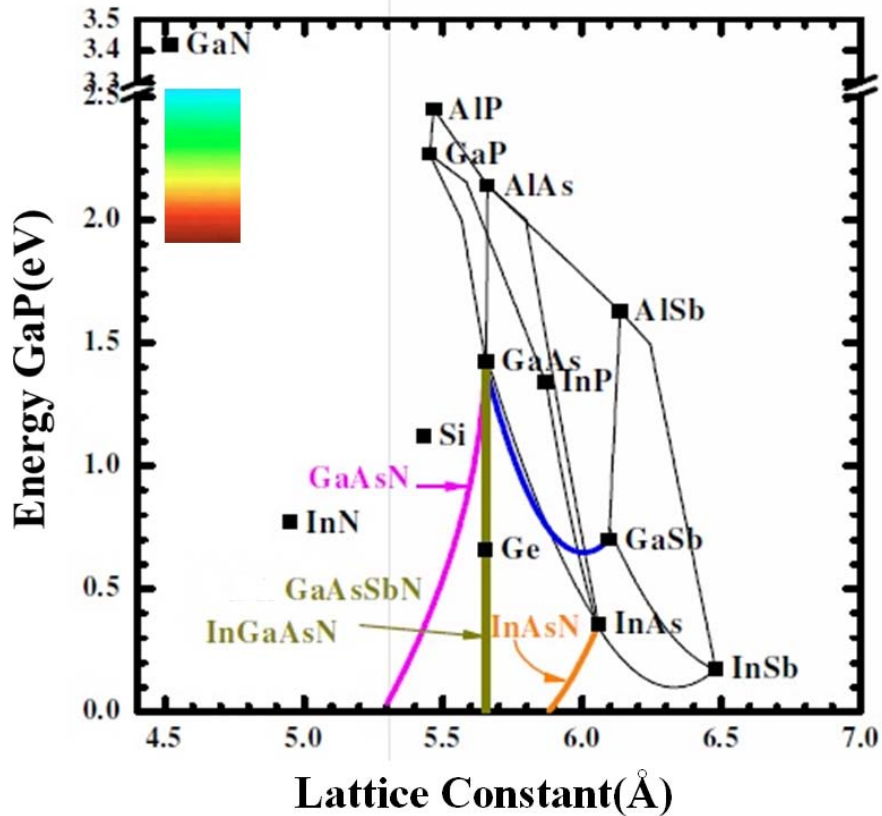

Figure 1. 1 The band-gap diagram of II-VI and III-V semiconductor materials.

1-2 Nitride-based semiconductor lasers

The research of blue light emitting devices began from the development of gallium nitride light emitting diodes in the early 1970s [9-11]. Two decades later, with several efforts devoted to the growth of nitride materials, doping concentration, efficiency of quantum wells, and so on, Nakamura *et al.* [2] developed the first prototype high-brightness (>100 times greater than previous alternatives, about 1 candela) GaN blue light emitting diodes in 1993. Then, in 1995, they also developed the first successful GaN electron-injection laser [1]. This makes nitride laser diodes begin to step on the road toward the commercial applications of high-information-density storage, laser printer, compact projector, and etc. In these years, the performance of nitride laser diodes has been improved to emit power as high as 100mW at room temperature with a low threshold only 3 kA/cm^2 [12], and the devices have been already successfully

commercialized to be applied to digital versatile disc (DVD). This next-generation DVD would enlarge the storage capacity from 4.7 giga-bytes which current DVD owns to 27 giga-bytes.

1-2.1 Edge emitting lasers

The major type of commercial nitride-based laser diodes now is edge emitting laser. This kind of structure is currently the most mature and producible one among all nitride laser devices. It is featured by a stripe-type long cavity and a pair of cleaved facet as the mirrors as shown in Figure 1. 2. Typically, the cavity length of the structure is about several hundred micro-meters. The light in the cavity is resonant in the horizontal direction and emits from the cleaved mirrors. The standard epi-layer structure of EELs usually is grown on sapphire and composes of p-n junction, multiple quantum wells (active region), and some cladding layer for photons and electrons. Over this decade, several improvements and researches on the growth and optimization of its structure were reported [13-16]. One is to improve the great amounts of defects and threading dislocations existing in the grown nitride materials on sapphire substrate due to the large lattice-mismatch between the nitride material and sapphire. The epitaxial lateral overgrowth (ELOG) is a very efficient method to reduce threading dislocation and defect density [13,14]. It is a method using the patterned SiO_x to make GaN laterally coalesce and bend threading dislocations to reduce the dislocation density. Generally, ELOG could decrease dislocation density down to the order of 10^8 cm^{-2}. Other one is to raise the low confinement factor of the optical field in the structure. Because the index difference between $Al_xGa_{1-x}N$ and GaN is small, the guiding of optical field in active region is usually weak. Nakamura *et al*. provided a solution that using modulation doped strain superlattice layer to improve the optical confinement [12, 13]. The other is to reduce spontaneous polarization and piezoelectric field in multiple quantum wells. Recently, M. Schmidt *et al*. [15] and D. Feezell [16] *et.al*. demonstrated nonpolar laser diode on m-plane GaN substrate. The laser diode emits violet light ~410nm and has the threshold current density of 3.7-8.2 KA/cm^2. The spontaneous and piezoelectric polarization effect was eliminated and the performance of laser diode could be further improved using this lattice matched substrate. The fabrication of flat and high-reflectivity mirrors is also a key point

for achieving an excellent lasing performance. In order to obtain a flat facet, the etching and cutting techniques were rapidly developed.

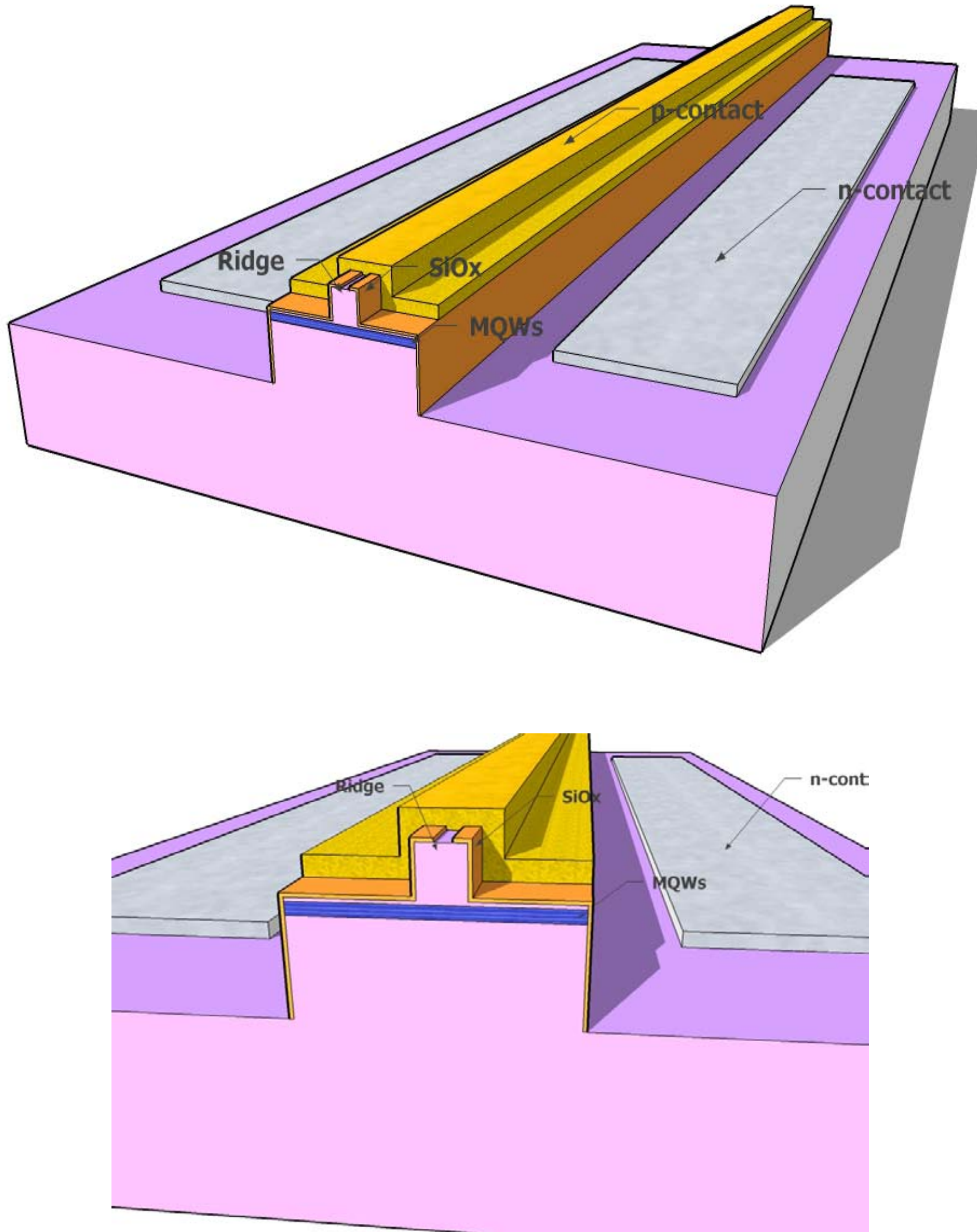

Figure 1. 2 The schematic diagram of an edge emitting laser diode.

1-2.2 Surface emitting lasers

1-2.2.1 Vertical cavity surface emitting lasers

Although the optimization of the edge emitting laser keeps going, some properties of this kind of laser are unfavorable. One of those properties is its elliptic beam shape. On one hand, the coupling efficiency would be low as the elliptic beam is coupled into optical fiber (typically in the form of circular core). On the other hand, for the application of storage, the elliptic beam not only makes each writing pixel larger but also raises expenses for correcting light shape. Usually, this kind of laser shows slightly large divergence angle to be over ten degree. This also is disadvantageous to the projection. Furthermore, the side emitting laser devices also makes the testing of devices a tough task. The wafer should be cut into several stripes (several laser devices on one strip) before the testing. For a commercial product, the complicated testing would result in a poor producing efficiency and be disadvantageous. Therefore, in order to have a superior laser device, K. Iga [17] demonstrated a new kind of laser diodes, vertical cavity surface emitting laser, in 1977. Vertical cavity surface emitting laser (VCSEL) is a vertical-emitting-type laser. It is formed by sandwiching a few-lambda cavity in a pair of reflectors, usually in the form of distributed Bragg reflector (DBR), with a very high reflectivity (>99.9%) as shown in Figure 1. 3. In contrast to EELs, photons in the cavity of VCSEL are vertically in resonance and emit outside perpendicularly to the surface of the structure. This laser diode can have many advantageous properties than conventional edge emitting laser, such as circular beam shape, lower divergence angle, two-dimensional laser array possible, efficient testing, low threshold, and so on. Owing to these superior performances, VCSELs had become very attractive and started to be applied to the commercial products at long wavelength range. In fact, short-wavelength VCSELs are also very promising for the applications of storage, display, and projection. In particular, the use of two-dimensional arrays of blue VCSELs could further reduce the read-out time in high density optical storage and increase the scan speed in high-resolution laser printing technology [18]. In recent years, several efforts have been devoted to the realization of nitride-based VCSELs [19-28]. Currently, three kinds of structures were reported:

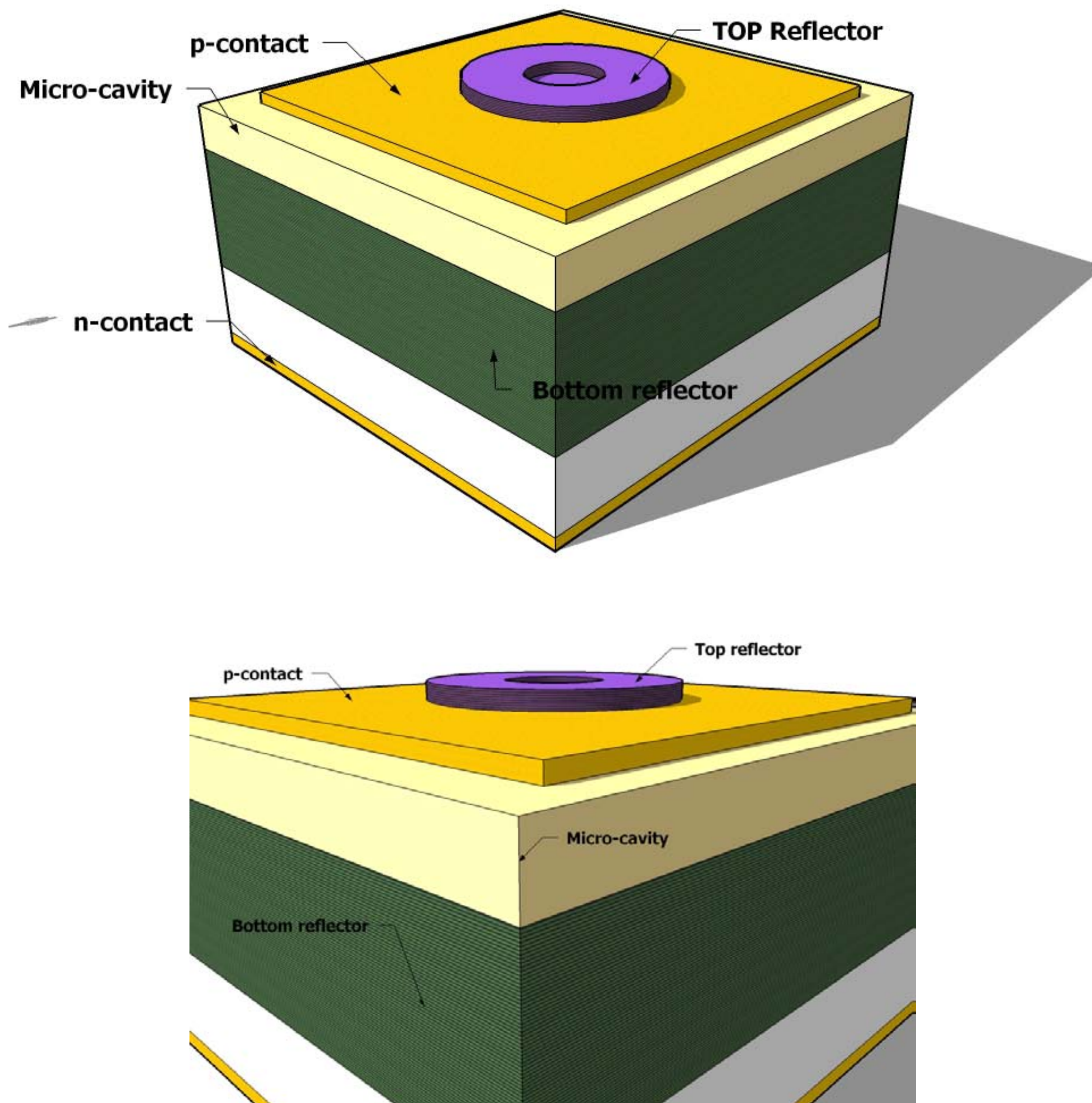

Figure 1. 3 The schematic diagram of a vertical-cavity surface emitting laser diode.

I. Fully epitaxial grown VCSEL structure

In 2005, J. F. Carlin [27] and E. Feltin [28] demonstrated the wholly epitaxial and high quality nitride-based micro-cavity (as shown in Figure 1. 4(a)) using metalorganic vapor phase epitaxy (MOVPE or MOCVD). They used the lattice-matched AlInN/GaN as the bottom and top reflectors to avoid cracks happened due to the accumulation of the strain

after stacking large pairs of layers. The reflectivity of AlInN/GaN could be achieved as high as 99.4%. They showed the 3/2-lambda cavity emitted a very narrow emission with a linewidth of 0.52 nm, corresponding to a quality factor of ~800.

II. VCSEL structure with two dielectric mirrors

Compared to epitaxial grown reflectors, the fabrication of dielectric mirrors is relatively simple. Furthermore, the large index difference of dielectric mirrors makes them could easily have wide stop band (>50nm) and high reflectivity (>99%) by coating just few stacks of 1/4-lambda-thick layers. Therefore, using dielectric mirrors to accomplish nitride-based VCSELs had begun attractive. Song *et al.* [19], Tawara *et al.* [20] and J. T. Chu *et al.* [22] successively reported the structure (as shown in Figure 1. 4(b)) after 2000. They employed some process techniques such as wafer bonding and laser lift-off to make dielectric mirrors be coated onto both sides of nitride-based cavity. They showed a micro-cavity could have a very high quality factor to be greater than 400 and achieve lasing action using optical pumping.

III. VCSEL structure with hybrid mirrors

The so-called hybrid mirrors are a combination of two different kinds of reflectors, for example, a dielectric mirror and an epitaxial reflector. Typically, the fabrication of this structure is to grow bottom reflector and cavity using MOCVD and then coat dielectric mirror to complete VCSEL structure (as shown in Figure 1. 4(c)). The hybrid-cavity nitride-based VCSEL\formed by the dielectric mirror and the epitaxial grown high-reflectivity GaN/$Al_xGa_{1-x}N$ DBR was reported earlier. In 1999, Someya *et al.* [18] used 43 pairs of $Al_{0.34}Ga_{0.66}N$/GaN as the bottom DBR and reported the lasing action at ~400nm. Then, Zhou et al [21] also employed a bottom DBR of 60 pairs $Al_{0.25}Ga_{0.75}N$/GaN and observed the lasing action at 383.2nm. Both these AlGaN/GaN DBR structures required large numbers of pairs due to the relatively low refractive index contrast between $Al_xGa_{1-x}N$ and GaN. Therefore, recently some groups began to study the AlN/GaN for application in nitride VCSEL. The DBR structure using AlN/GaN has higher refractive index contrast ($\Delta n/n=0.16$)[28] that can achieve high reflectivity with relatively less numbers of pairs. It has wide stop band that can easily align with the active layer emission peak to achieve lasing action. However, the AlN/GaN combination also

has relatively large lattice mismatch (~2.4%) and the difference in thermal expansion coefficients between GaN ($5.59x10^{-6}$/K) and AlN ($4.2x10^{-6}$/K) that tends to cause cracks in the epitaxial film during the growth of the AlN/GaN DBR structure and could result in the reduction of reflectivity and increase in scattering loss. With the mature of epitaxy techniques, the high-reflectivity AlN/GaN DBR structure with relatively smooth surface morphology has become possible with just twenty or thirty pairs [29].

In comparison of these three VCSELs, it doesn't require complicated process such as laser lift-off technique to complete a hybrid VCSEL device. This means the fabrication of such structure is stable and reliable comparing to other structures. Thus, the hybrid structure is more advantageous in the aspects of fabrication and commercialization

In fact, the investigation of the characteristics of the GaN-based VCSELs has gradually attracted more attentions. Kako *et al.* [30] investigated the coupling efficiency of spontaneous emission (β) and the polarization property of the nitride VCSEL and obtained a high β value of 1.6×10^{-2} and a strong linear polarization of 98%. Tawara *et al*. [20] also found a high β value of 10^{-2} in the nitride VCSEL with two dielectric mirrors. Honda *et al.* reported the estimation of high characteristics temperature of GaN-based VCSEL[31]. These all mean the development of nitride-based VCSEL and the understanding of the laser performance has become more and more important. Especially, the current-injected nitride-based VCSEL still can't be realized, therefore, more efforts on it are necessary and crucial for high performance future application.

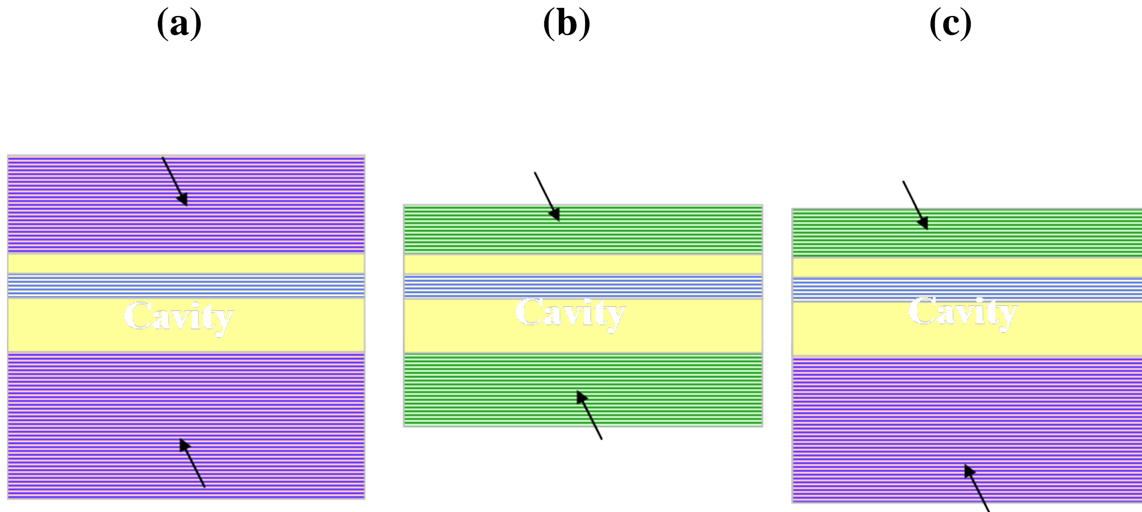

Figure 1. 4 Schematic diagrams of three nitride-based VCSEL structures.

1-2.2.2 Two-dimensional photonic crystal lasers

Besides VCSEL, a novel structure, photonic crystal (PhC) laser, was demonstrated to be a new type of the vertical emitting laser after 1990s. It is featured by a periodic structure called photonic crystal. According to the theory, the light in the photonic crystal structure would be forbidden or only allowed in specific modes, and those modes could be plotted as a photonic band diagram as shown in Figure 1. 5. Consequently, such structures can act not only as a passive waveguide or resonator to direct the wave propagation but also as an active medium to control light emission [32]. For fabricating laser devices, there are two kinds of 2-D PhC lasers to be reported in these few years. One is 2-D PhC nano-cavity laser, and another is 2-D PhC band-edge laser.

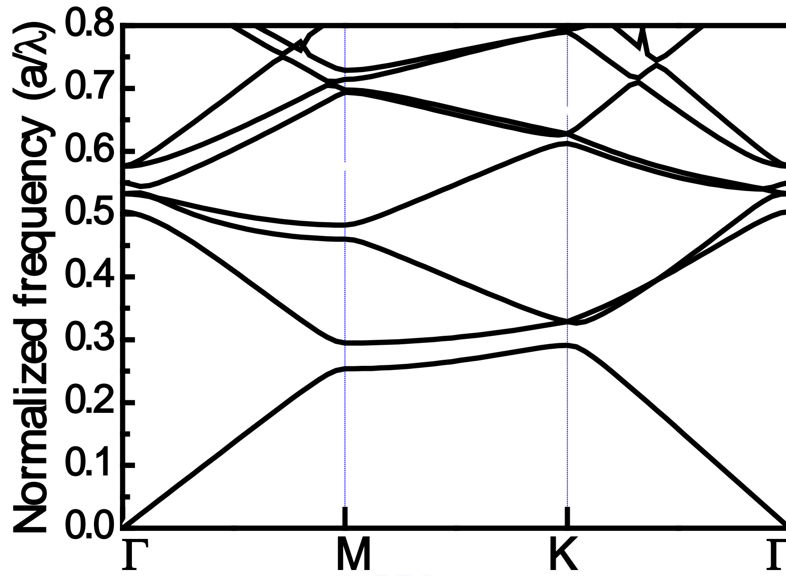

Figure 1. 5 The band diagram of a 2-D triangular-lattice PhC structure.

I. <u>2-D PC Nano-Cavity Lasers</u>

In 1994, P. R. Berman *et al.* first presented that photonic crystal could be a reflective mirror around the cavity of a laser [33]. Then, in 1999 O. Painter practically demonstrated an optically pumped InGaAs-based 2-D PhC nano-cavity laser emitting 1.55 micrometers (as shown in Figure 1. 6) [34]. The optical cavity he demonstrated consisted of a half-wavelength-thick waveguide for vertical confinement and a 2-D PhC mirror for lateral localization. A defect was introduced as a nano-cavity (a volume of 2.5 cubic half-wavelength, approximately 0.03 cubic micrometers) in the 2-D PhC to trap photons inside. In 2004, Hong-Gyu Park *et al.* realized the electrically driven single-cell 2D-PhC laser (λ=1519.7 nm) [35]. They used a sub-micrometer-sized semiconductor post placed below the center of the single-cell photonic crystal resonator to connect bottom electrode and achieved lasing action via current injection.

In 2005, nitride-based blue (about 488nm) photonic crystal membrane nano-cavity with Q factor about 800 was also reported by Y. S. Choi *et al.* [36]. They used photo-enhanced chemical etching to form a GaN membrane with a total thickness of 140 nm and patterned a photonic crystal cavity on it. Some resonance modes from the nano-cavities with lattice constant 180 nm could be observed in the photoluminescence

(PL) emission.

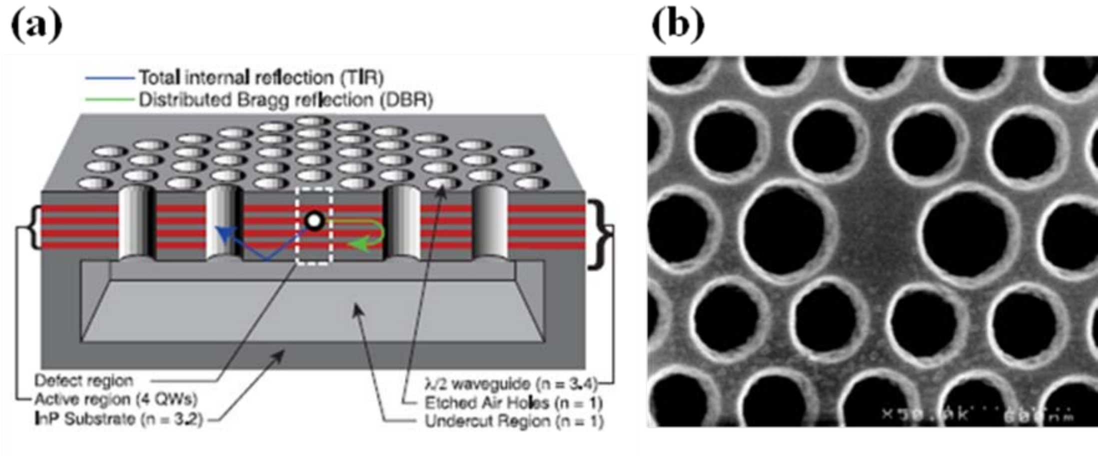

Figure 1. 6 (a)The first InGaAsP photonic crystal defect laser structure and (b) The plane-view SEM image of single defect photonic crystal structure with hexagonal lattice.

II. <u>2-D PC Band-edge lasers</u>

Compared to 2-D PhC nano-cavity lasers, it is not necessary to create a defect in the 2-D photonic crystal to be a nano-cavity for a 2-D PhC band-edge laser. That is, the 2-D photonic band-edge laser is composed of a perfect photonic crystal structure. Then, by satisfying Bragg condition, the laser action would happen in those band edge points in the photonic band diagram. In 1999, Noda *et al.* reported the electrically driven 2-D PhC band-edge laser under pulsed operation [37]. The PhC was a triangular-lattice structure composed of InP and air holes, which is integrated with an InGaAsP/InP multiple-quantum-well active layer by a wafer fusion technique. They demonstrated the single-mode, large-area and surface-emitting lasing action, and analyzed the lasing mechanism based on the satisfying of Bragg condition. Then, they further reported the room-temperature (RT) 2-D PhC band-edge laser under continuous wave (CW) operation in 2004 [38]. This opens a new road toward the large-area single-mode surface emitting laser.

1-3 Objective of the thesis

From the view of superior laser devices, the single mode, large area, high

output-power, and surface emitting have become basic requirements for the future laser device. In this thesis, we mainly focus on the study of nitride-based surface emitting lasers including the vertical-cavity surface emitting lasers (VCSEL) and 2-D photonic crystal surface emitting lasers (PCSEL). About VCSEL, the study consists of the design, fabrication, and characteristics of the laser. We discuss and analyze the performance of GaN-based VCSEL such as threshold characteristics, laser spectrum, polarization, divergence angle, characteristic temperature, and coupling efficiency of spontaneous emission. Furthermore, unique lasing phenomenon, such as specific mode behavior and quality factor in the structure, are also investigated. We also establish the fabrication processes 2-D PCSEL, using the epitaxial part of our nitride-based VCSEL, i.e. the structure with a GaN cavity and an AlN/GaN bottom reflector. The fabrication and characteristics of the GaN-based 2-D PCSEL are also demonstrated. The detail calculation, simulation, and experiment such as threshold characteristics, laser spectrum, polarization, divergence angle, characteristic temperature, and coupling efficiency of spontaneous emission are also investigated

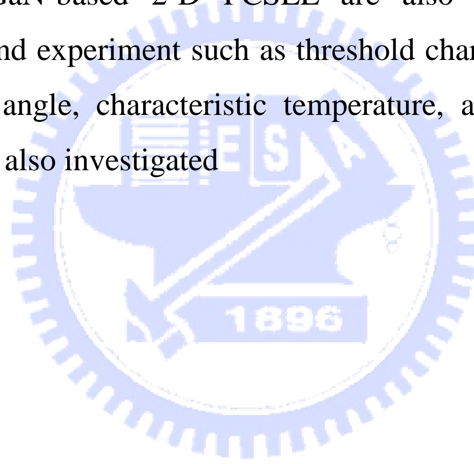

References.

[1] S. Nakamura, T. Mukai, and M. Senoh, *Appl. Phys. Lett.*, **64**, 1687 (1994)

[2] S. Nakamura, M. Senoh, S. Nagahama, N.Iwasa, T. Yamada, T. Matsushita, Y. Sugimoto, and H. Kiyoku, *Appl. Phys. Lett.*, **70**, 868 (1997)

[3] S. Nakamura, *Science*, **281**, 956 (1998)

[4] Y. Arakawa, *IEEE J. Select. Topics Quantum Electron.*, **8**, 823 (2002)

[5] S. Nakamura, M. Senoh, N. Iwasa, and S. Nagahama, *Jpn. J. Appl.Phys.*, **34**, L797 (1995)

[6] H. Morkoc, *Nitride Semiconductors and Devices (Spring Verlag, Heidelberg)* (1999)

[7] S. N. Mohammad, and H. Morkoc, *Progress in Quantum Electron.*, **20**, 361 (1996)

[8] J. I. Pankove, E. A. Miller, J. E. Berkeyheier, *J. Luminescence*, **5**, 84 (1972)

[9] H. P. Maraska, D. A. Stevenson, J. I. Pankove, *Appl. Phys. Lett.*, **22**, 303 (1973)

[10] J. I. Pankove, *Phys. Rev. Lett.*, **34**, 809 (1975)

[11] M. Takeya, T. Tojyo, T. Asano, S. Ikeda, T. Mizuno, O. Matsumoto, S. Goto, Y. Yabuki, S. Uchida, and M. Ikeda, *phys. stat. sol. (a)*, **192**, 269 (2002)

[12] S. Nakamura, M. Senoh, S. Nagahama, N. Iwasa, T. Yamada, T. Matsushita, H. Kiyoku, Y. Sugimoto, T. Kozaki, H. Umemoto, M. Sano, and K. Chocho, *Appl. Phys. Lett.*, **72,** 211 (1998)

[13] S. Nakamura, *IEEE J. Select. Topics Quantum Electron.*, **4**, 483 (1998)

[14] M. C. Schmidt, K. C. Kim, R, M. Farrell, D. F. Feezell, D. A. Cohen, M. Saito, K. Fujito, J. S. Speck, S. P. Denbaars, and S. Nakamura, *Jpn. J. Appl. Phys*, **46**, L190 (2007)

[15] D. F. Feezell, M. C. Schmidt, Robert M. Farrell, K. C. Kim, M. Saito, K. Fujito, D. A. Cohen, J. S. Speck, S. P. Denbaars, and S. Nakamura, *Jpn. J. Appl. Phys*, **46**, L284 (2007)

[16] K. Iga, *IEEE J. Quantum Electron.*, **24**, 1845 (1988)

[17] K. Iga, *Proceedings of the First International Symposium on blue lasers and light emitting diodes*, Th-11 (1996)

[18] T. Someya, R. Werner, A. Forchel, M. Catalano, R. Cingolani, Y. Arakawa, Science, **285**, 1905 (1999)

[19] Y. K. Song, H. Zhou, M. Diagne, A. V. Nurmikko, R. P. Schneider, Jr., C. P. Kuo, M. R. Krames, R. S. Kern, C. C. Coman, and F. A. Kish, *Appl. Phys. Lett.*, **76**, 1662 (2000)

[20] T. Tawara, H. Gotoh, T. Akasaka, N. Kobayashi, and T. Saitoh, *Appl. Phys. Lett*., **83**, 830 (2003)

[21] H. Zhou, M. Diagne, E. Makarona, A. V. Nurmikko, J. Han, K. E. Waldrip and J. J. Figiel, *Electron. Lett.*, **36**,1777 (2000)

[22] J. T. Chu, T. C. Lu, H. H. Yao, C. C. Kao, W. D. Liang, J. Y. Tsai, H. C. Kuo, S. C. Wang, *Jpn. J. Appl. Phys*, **45**, 2556 (2006).

[23] J. T. Chu, T. C. Lu, M. You, B. J. Su, C. C. Kao, H. C. Kuo, S. C. Wang, *Appl. Phys. Lett.*, **89**, 121112 (2006)

[24] C. C. Kao,Y. C. Peng, H. H. Yao, J. Y. Tsai, Y. H. Chang, J. T. Chu, H. W. Huang, T. T. Kao, T. C. Lu, H. C. Kuo,S. C. Wang, C. F. Lin., *Appl. Phys. Lett.*, **87**, 081105-1 (2005).

[25] C. C. Kao, T. C. Lu, H. W. Huang, J. T. Chu, Y. C. Peng, H. H. Yao, J. Y. Tsai, T. T. Kao, H. C. Kuo, S. C. Wang, C. F. Lin., *IEEE Photon. Technol. lett*., **18**, 877 (2006).

[26] J. F. Carlin, J. Dorsaz, E. Feltin, R. Butté, N. Grandjean, M. Ilegems, and M. Laügt, *Appl. Phys. Lett.*, **86**, 031107 (2005)

[27] E. Feltin, R. Butté, J. F. Carlin, J. Dorsaz, N. Grandjean, and M. Ilegems, *Electron. Lett.*, **41**, 94 (2005)

[28] T. Ive, O. Brandt, H. Kostial, T. Hesjedal, M. Ramsteiner, and K. H. Ploog, *Appl. Phys. Lett*., **85**, 1970 (2004)

[29] H. H. Yao, C. F. Lin, H. C. Kuo, S. C. Wang, *J. Crystal Growth,* **262***,* 151 (2004)

[30] S. Kako, T. Someya, and Y. Arakawa, *Appl. Phys. Lett.*, **80**, 722 (2002)

[31] T. Honda, H. Kawanishi, T. Sakaguchi, F. Koyama and K. Iga, *MRS Internet J. Nitride Semicond.,* **4S1**, G6.2-1 (1999).

[32] C. M. Lai, H. M. Wu, P. C. Huang, S. L. Peng, *Appl. Phys. Lett.*, **90**, 141106, (2007)

[33] P. R. Berman, New York:Academic, (1994)

[34] O. Painter, R. K. Lee, A. Scherer, A. Yariv, J. D. O`Brien, P. D. Dapkus, I. Kim, *Science*, **284**, 1819, (1999)

[35] H. G. Park, S. H. Kim, S. H. Kwon, Y. G. Ju, J. K. Yang, J. H. Baek, S. B. Kim, Y. H. Lee, *Science*, **305**, 1444, (2005)

[36] Y. S. Choi, K. Hennessy, R. Sharma, E. Haberer, Y. Gao, S. P. DenBaars, C. Meier, *Appl. Phys. Lett.*, **87**, 243101, (2005)

[37] M. Imada, S. Node, A. Chutinan. and T. Tokuda, *Appl. Phys. Lett.*, **75**, 316, (1999)

[38] D. Ohnishi, T. Okano, M. Imada, and S. Node, *Opt. Exp.,* **12**, 1562, (2004)

Chapter 2
Design and Fabrication of Vertical-Cavity Surface Emitting Lasers

2-1 Operation principle of semiconductor lasers

Carrier density rate equation

For the DH active region, the injected current provides a generation term, and various radiative and nonradiative recombination process as well as carrier leakage provide recombination terms. Thus, we can write the carrier density rate equation,

$$\frac{dN}{dt} = G_{gen} - R_{rec} \qquad (2.\ 1)$$

where N is the carrier density (electron density), G_{gen} is the rate of injected electrons and R_{rec} is the ratio of recombining electrons per unit volume in the active region. Since $\frac{\eta_i I}{q}$ are electrons per second being injected into the active region, $G_{gen} = \frac{\eta_i I}{qV}$, where V is the volume of the active region. The recombination process is complicated and several mechanisms must be considered. Such as, spontaneous recombination rate, $R_{sp} \sim BN^2$, nonradiative recombination rate, R_{nr}, carrier leakage rate, R_l, ($R_{nr} + R_l = AN + CN^3$), and stimulated recombination rate, R_{st}. Thus we can write $R_{rec} = R_{sp} + R_{nr} + R_l + R_{st}$. Besides, $N/\tau \equiv R_{sp} + R_{nr} + R_l$, where τ is the carrier lifetime. Therefore, the carrier density rate equation could be expressed as

$$\frac{dN}{dt} = \frac{\eta_i I}{qV} - \frac{N}{\tau} - R_{st} \qquad (2.\ 2)$$

Photon density rate equation

Now, we describe a rate equation for the photon density (N_p), which includes the photon generation and loss terms. The photon generation process includes spontaneous recombination (R_{sp}) and stimulated recombination (R_{st}), and the main photon generation term of laser above threshold is R_{st}. Every time an electron-hole pair is stimulated to

recombine, another photon is generated. Since, the cavity volume occupied by photons, V_p, is usually larger than the active region volume occupied by electrons, V, the photon density generation rate will be $[V/V_p]R_{st}$ not just R_{st}. This electron-photon overlap factor, V/V_p, is generally referred to as the confinement factor (Γ). Sometimes it is convenient to introduce an effective thickness (d_{eff}), width (w_{eff}), and length (L_{eff}) that contains the photons. That is, $V_p=d_{eff}w_{eff}L_{eff}$. Then, if the active region has dimensions, d, w, and L_a, the confinement factor can be expressed as, $\Gamma=\Gamma_x\Gamma_y\Gamma_z$, where $\Gamma_x = d/d_{eff}$, $\Gamma_y = w/w_{eff}$, $\Gamma_z = L_a/L_{eff}$. Photon loss occurs within the cavity due to optical absorption and scatting out of the mode, and it also occurs at the output coupling mirror where a portion of the resonant mode is usually couple to some output medium. These net losses can be characterized by a photon (or cavity) lifetime (τ_p). Hence, the photon density rate equation takes the form

$$\frac{dN_p}{dt} = \Gamma R_{st} + \Gamma \beta_{sp} R_{sp} - \frac{N_p}{\tau_p} \tag{2. 3}$$

where β_{sp} is the *spontaneous emission factor*. As to R_{st}, it represents the photon-stimulated net electron-hole recombination which generates more photons. This is a gain process for photons. It is given by

$$\left(\frac{dN_p}{dt}\right)_{gen} = R_{st} = \frac{\Delta N_p}{\Delta t} = v_g \mathrm{g} N_p \tag{2. 4}$$

where v_g is the group velocity and g is the gain per unit length.
Now, we rewrite the carrier and photon density rate equations

$$\frac{dN}{dt} = \frac{\eta_i I}{qV} - \frac{N}{\tau} - v_g \mathrm{g} N_p \tag{2. 5}$$

$$\frac{dN_p}{dt} = \Gamma v_g \mathrm{g} N_p + \Gamma \beta_{sp} R_{sp} - \frac{N_p}{\tau_p} \tag{2. 6}$$

Threshold gain

In order for a mode of the laser to reach threshold, the gain in the active section must be increased to the point when all the propagation and mirror losses are compensated. Most laser cavities can be divided into two general sections: an active section of length L_a and a passive section of length L_p. For a laser, at the threshold, the gain is equal whole loss in the cavity, which includes cavity absorption and mirror loss. For convenience the

mirror loss term is sometimes abbreviated as, $\alpha_m \equiv (1/2L)\ ln(1/R_1R_2)$. Noting that the cavity life time (photon decay rate) is given by the optical loss in the cavity, $1/\tau_p = 1/\tau_i + 1/\tau_m = v_g(\alpha_i + \alpha_m)$. Thus, the threshold gain in the steady state can be expressed with following equation

$$\Gamma g_{th} = \alpha_i + \alpha_m = \frac{1}{v_g \tau_p} = \alpha_i + \frac{1}{2L} \ln\left(\frac{1}{R_1 R_2}\right) \qquad (2.\ 7)$$

where α_i is the average internal loss which is defined by $(\alpha_{ia}L_a + \alpha_{ip}L_p)/L$ (i.e.,$\alpha_{ia}L_a$ and $\alpha_{ip}L_p$ are loss of active region and passive section, respectively), and R_1 and R_2 is the reflectivity of top and bottom mirror of the laser cavity, respectively.

Output power versus driving current

The characteristic of output power versus driving current (L-I characteristic) in a laser diode can be realized by using the rate equation Eq. (2. 5) and Eq. (2. 6). Consider the below threshold (almost threshold) steady-state ($dN/dt = 0$) carrier rate equation, the Eq. (2. 5) is given by $\frac{\eta_i I_{th}}{qV} = \frac{N_{th}}{\tau}$. While the driving current is above the threshold, the carrier rate equation will be

$$\frac{dN}{dt} = \eta_i \frac{(I - I_{th})}{qV} - v_g g N_p \qquad (2.\ 8)$$

From Eq. (2. 8), the steady-state photon density above threshold where $g = g_{th}$ can be calculated as

$$N_p = \frac{\eta_i (I - I_{th})}{q v_g g_{th} V} \qquad (2.\ 9)$$

The optical energy stored in the cavity, E_{os}, is constructed by multiplying the photon density, N_p, by the energy per photon, $h\nu$, and the cavity volume, V_p. That is $E_{os} = N_p h\nu V_p$. Then, we multiple this by the energy loss rate through the mirrors, $v_g\alpha_m = 1/\tau_m$, to get the optical power output from the mirrors, $P_0 = v_g \alpha_m N_p h\nu V_p$. By using Eq. (2. 7) and Eq. (2. 9), and $\Gamma = V/V_p$, we can write the output power as the following equation

$$P_O = \eta_i \left(\frac{\alpha_m}{\alpha_i + \alpha_m}\right) \frac{h\nu}{q} (I - I_{th}) \qquad (2.\ 10)$$

Now, by defining $\eta_d = \frac{\eta_i \alpha_m}{\alpha_i \alpha_m}$, Eq.(2. 1 0) can be simplified as

$$P_O = \eta_d \frac{h\nu}{q}(I - I_{th}) \qquad (I>I_{th}) \qquad (2.1\ 1)$$

Thus, the η_d can be expressed as

$$\eta_d = \left[\frac{q}{h\nu}\right]\frac{dP_O}{dI} \qquad (I>I_{th}) \qquad (2.1\ 2)$$

In fact, η_d is the differential quantum efficiency, defined as number of photons out per electron. Besides, dP_o/dI is defined as the slope efficiency, S_d, equal to the ratio of output power and injection current. Figure 2. 1 shows the illustration of output power vs. current for a diode laser. Below threshold, only spontaneous emission is important; above threshold, the stimulated emission power increases linearly with the injection current while the spontaneous emission is clamped at its threshold value.

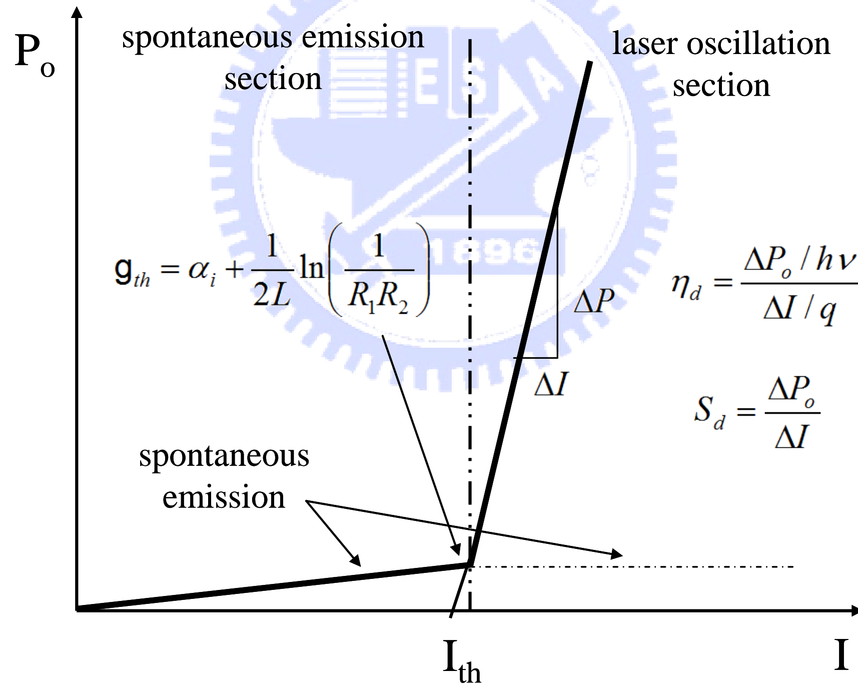

Figure 2. 1 An illustration of output power vs. current for a diode laser.

<u>**Coupling Efficiency of Spontaneous Emission into a Lasing Mode [1]**</u>

In a conventional semiconductor laser, only a very small part of the spontaneous emission is coupled into a single-lasing mode. That is because the radiation pattern of spontaneous emission is isotropic, a substantial part of the spontaneous emission is not

coupled to the guided modes in an active waveguide with a small acceptance angle. Furthermore, the spontaneous emission spectral linewidth is broader than the linewidth of the longitudinal mode; therefore, a substantial part of the spontaneous emission is not coupled to a lasing mode. That is, the coupling efficiency of spontaneous emission (β) usually is considerably small for typical laser diodes.

Suppose an active volume V of semiconductor laser, which is much larger than the cubic of optical length, is enclosed by "perfect reflector". The number of modes per unit frequency interval is given by $8\pi v^2 V \varepsilon^{3/2} / c^3$. If we assume the active dipoles are distributed uniformly in the volume V and are randomly oriented, the coupling efficiency of spontaneous emission into each mode is identical. The total spontaneous emission rate is given by

$$R_{sp} \equiv N_c \gamma = \int \frac{8\pi v^2 V \varepsilon^{3/2}}{c^3} |g|^2 \frac{2\Gamma N_c}{4\pi^2 (v - v_0)^2 + \Gamma^2} dv = \frac{8\pi v^2 V \varepsilon^{3/2} |g|^2 N_c}{c^3} \qquad (2.1\ 3)$$

Here $|g|^2$ is the electric dipole coupling constant and a Lorentzian line shape is assumed, 2Γ is the spontaneous emission linewidth in rad/s (FWHM), γ is the spontaneous decay rate, and N_c is total minority-carrier number. If the lasing frequency is coincident with gain center $v = v_0$, the spontaneous emission rate E_{cv} into one lasing mode is

$$E_{cv} = \frac{2|g|^2 N_c}{\Gamma} \qquad (2.1\ 4)$$

From Eq. (2. 1 3) and Eq. (2. 1 4), the coupling efficiency β of spontaneous emission into the lasing mode (spontaneous emission coefficient) is calculated as [2]

$$\beta \equiv \frac{E_{cv}}{R_{sp}} = \frac{c^3}{4\pi v^2 \varepsilon^{3/2} V \Gamma} = \frac{\lambda^4}{4\pi^2 V \Delta\lambda \varepsilon^{3/2}} \approx 0.025 \frac{\lambda^4}{\varepsilon^{3/2} \Delta\lambda V} \qquad (2.1\ 5)$$

Here $\Delta\lambda = \lambda^2 \Gamma / c\pi$ is the spontaneous emission linewidth in meters (FWHM). If we use the numerical parameters of a typical GaN semiconductor laser, assuming $\lambda = 4 \times 10^{-7} m$, $\varepsilon^{1/2} = 2.5$, $\Delta\lambda = 2 \times 10^{-8} m$, and $V = 10^{-15} m^3$, the spontaneous emission coefficient β is on the order of 10^{-5}. This means that only one photon of 10^5 spontaneously emitted photons could couple into a lasing mode.

Besides equation Eq. (2. 1 5), β also could be written as [3]:

$$\beta = F_p / (1 + F_p)$$
$$F_p = \frac{3}{4\pi^2} \frac{Q}{V_c / (\lambda / \bar{n})^3} \quad (2.1\ 6)$$

where F_p is the Purcell factor, Q is the cavity quality factor, λ is the wavelength of laser mode, V_c is the effective optical volume of the laser mode, and $\bar{n}$ is the refractive index.

<u>The calculation of the spontaneous emission coupling efficiency[1]</u>

As discussed already, the coupling efficiency of spontaneous emission into a lasing mode can be increased to a value close to 1 for a microcavity semiconductor laser from 10^{-5} for a conventional semiconductor laser. The characteristics of such a microcavity semiconductor laser would be very different from a conventional semiconductor laser.

The quantum Langevin equation for the (total) electron number operator $\hat{N}_c$ is written as [4]

$$\frac{d}{dt}\hat{N}_c = P - \left[\frac{1-\beta}{\tau_{sp}} + \frac{\beta}{\tau_{sp}}\right]\hat{N}c - (\hat{E}_{cv} - \hat{E}_{vc})\hat{n} + \hat{\Gamma}_p + \hat{\Gamma}_{sp} + \hat{\Gamma}, \quad (2.1\ 7)$$

where P is the pump rate, $\beta < \hat{N}_c > /\tau_{sp}$ is the spontaneous emission rate into a lasing mode, $(1-\beta) < \hat{N}_c > /\tau_{sp}$ is the spontaneous emission rate into all other modes except the lasing mode, $< \hat{E}_{cv} >$ and $< \hat{E}_{vc} >$ are the stimulated emission and absorption rates per photon, $(< \hat{E}_{cv} > - < \hat{E}_{vc} >)$ is a population inversion parameter, $\hat{n}$ is the (total) photon number operator, $\hat{\Gamma}_p$, $\hat{\Gamma}_{sp}$, and $\hat{\Gamma}$ are the noise operators associated with the pump process, the spontaneous emission process and stimulated emission or absorption process.

The spontaneous emission rate into the lasing mode and the stimulated emission rate per photon should be equal by the Einstein's relation, so that we have

$$\frac{\beta}{\tau_{sp}} < \hat{N}_c > = < \hat{E}_{cv} > \quad (2.1\ 8)$$

The quantum Langevin equations for (total) photon number operator $\hat{n}$ is written as

$$\frac{d}{dt}\hat{n} = -\left[\frac{\omega}{Q} - (\hat{E}_{cv} - \hat{E}_{vc})\right]\hat{n} + \frac{\beta}{\tau_{sp}}\hat{N}_c + \hat{F} + \hat{F}_e \tag{2.1 9}$$

where ω/Q is the photon decay rate, $\hat{F}$, and $\hat{F}_e$ are the noise operators associated with the stimulated emission processes, and the photon decay process.

Let us consider the steady-state (average) solutions of Eq. (2. 1 7) and Eq. (2. 1 9). Using the linear solutions, $\hat{N}_c = N_{c0} + \Delta\hat{N}_c$ and $\hat{n} = n_0 + \Delta\hat{n}$, in Eq. (2. 1 7) and (2. 1 9), we obtain

$$P - \frac{N_{c0}}{\tau_{sp}} - \frac{\beta}{\tau_{sp} n_{sp}} n_0 = 0 \tag{2.2 0}$$

$$-\left[\frac{\omega}{Q} - \frac{\beta N_{c0}}{\tau_{sp} n_{sp}}\right] n_0 + \frac{\beta N_{c0}}{\tau_{sp}} = 0 \tag{2.2 1}$$

At pump rates above the threshold, the photon decay rate ω / Q is equal to the net gain $\hat{E}_{cv} - \hat{E}_{vc}$ (i.e., the stimulated emission gain-stimulated absorption loss). Thus,

$$\frac{\omega}{Q} = \frac{\beta N_{c0,th}}{\tau_{sp} n_{sp}} \tag{2.2 2}$$

where $N_{c0,th}$ is the threshold (total) electron number, which is approached by real electron number N_{c0} only when the pump rate is well above the threshold.

At the threshold pump rate, all the pump electrons recombine via spontaneous emission $(P_{th} = N_{c0,th} / \tau_{sp})$. The stimulated emission rate E_{cv} by one photon is equal to the spontaneous emission so that

$$E_{cv} = \beta P_{th} \tag{2.2 3}$$

From Eq. (2. 2 2), the threshold pump rate can be calculated as

$$P_{th} = \frac{N_{c0,th}}{\tau_{sp}} = \frac{(\omega / Q) n_{sp}}{\beta} \tag{2.2 4}$$

This is an important result suggests that the threshold pump rate can be decreased by

increasing β.

From Eq. (2. 2 1), the average photon number n_0 is

$$n_0 = \frac{\beta N_{c0} / \tau_{sp}}{\omega / Q - \beta N_{c0} / \tau_{sp} n_{sp}} \tag{2.2 5}$$

It is obvious from this equation that the real electron number N_{c0} never reaches the threshold value $N_{c0,th}$ as long as the spontaneous emission coefficient β is nonzero. From Eq. (2. 2 1), the average electron number N_{c0} is given by

$$N_{c0} = \begin{cases} N_{c0,th} \dfrac{(r+1) - [(r+1)^2 - 4(1-\beta)r]^{1/2}}{2(1-\beta)} \quad , \quad \beta \neq 1 \\ N_{c0,th} \dfrac{r}{1+r} \quad , \quad \beta = 1 \end{cases} \tag{2.2 6}$$

where $r = P / P_{th}$ is the normalized pump rate and $N_{c0,th} = \omega \tau_{sp} n_{sp} / Q\beta$. Using Eq. (2. 2 5) in Eq. (2. 2 6), the average photon number n_0 is

$$n_0 = \begin{cases} n_{sp} \dfrac{(r+1) - [(r+1)^2 - 4(1-\beta)r]^{1/2}}{2(1-\beta)} \Big/ \left[1 - \dfrac{(r+1) - [(r+1)^2 - 4(1-\beta)r]^{1/2}}{2(1-\beta)} \right] \quad , \quad \beta \neq 1 \\ n_{sp} r \quad , \quad \beta = 1 \end{cases} \tag{2.2 7}$$

If the photon number n_0 is larger than one before the carrier density exceeds a transparency point, the stimulated emission rate into the lasing mode, even though the net gain is still negative. The threshold condition Eq. (2. 2 4) holds when the photon number n_0 is much smaller than one at the transparency point. Figure 2. 2 shows the internal photon number n_0 versus the pump rate P as a function of the spontaneous emission coefficient β, assuming that $n_{sp} = 1$ and βP_{th} is the same for each curve with different β value. It is clear the jump of photon nember at near threshold is smaller and smaller as the value of β is larger. As the $\beta = 1$, the increase of photon number with the increasing of pump rate becomes a linear increasing.

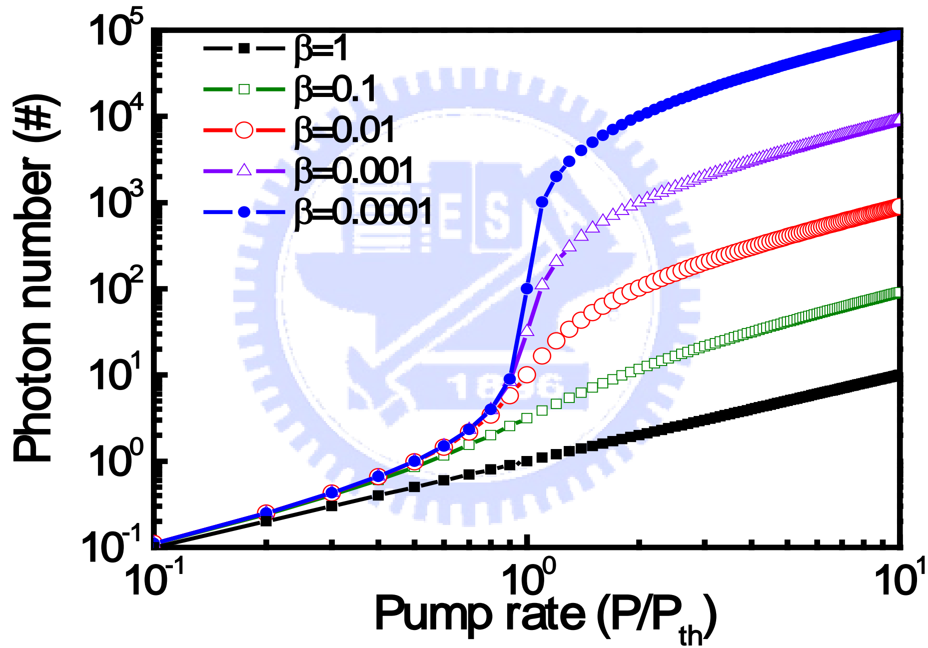

Figure 2. 2 The internal photon number n_o versus the pump rate P as a function of the spontaneous emission coefficient β.

2-2 Distributed Bragg reflectors

The research of blue light emitting devices began from the development of gallium nitride light emitting diodes in the early 1970s [5-7]. Two decades later, with several efforts devoted to the growth of nitride materials, doping concentration, efficiency of quantum wells, and so on, Nakamura *et al*. developed the first prototype high-brightness (>100 times greater than previous alternatives, about 1 candela) GaN blue light emitting diodes

in 1993. Then, in 1995, they also developed the first successful GaN electron-injection laser. This makes nitride laser diodes begin to step on the road toward the commercial applications of high-information-density storage, laser printer, compact projector, and etc. In these years, the performance of nitride laser diodes has been improved to emit power as high as 100mW at room temperature with a low threshold only 3 kA/cm^2, and the devices have been already successfully commercialized to be applied to digital versatile disc (DVD). This next-generation DVD would enlarge the storage capacity from 4.7 giga-bytes which current DVD owns to 27 giga-bytes.

2-2.1 Penetration depth

Distributed Bragg reflectors (DBRs) served as high reflecting mirror in numerous optoelectronic and photonic devices such as VCSEL. It is a periodic structure formed by stacking several pairs of two 1/4-lamda-thick layers with different refractive index. Consider a distributed Bragg reflector consisting of m pairs of two dielectric, lossless materials with high- and low- refractive index n_H and n_L, as shown in Figure 2. 3. The thickness of the two layers is assumed to be a quarter wave, that is, $L_1 = \lambda_B/4n_H$ and $L_2 = \lambda_B/4n_L$, where the λ_B is the Bragg wavelength.

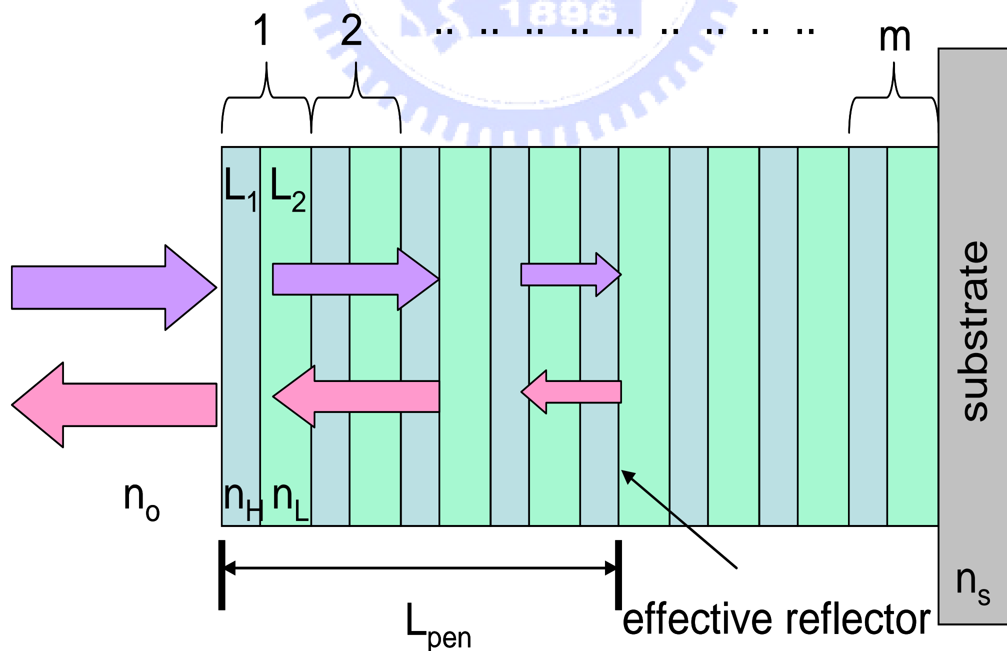

Figure 2. 3 A schematic diagram of DBRs

Multiple reflections at the interface of the DBR and constructive interference of the multiple reflected waves increase the reflectivity with increasing number of pairs. The reflectivity has a maximum at the Bragg wavelength λ_B. The reflectivity of a DBR with m quarter wave pairs at the Bragg wavelength is given by

$$R = \left(\frac{1 - \frac{n_s}{n_o} (\frac{n_L}{n_H})^{2p}}{1 + \frac{n_s}{n_o} (\frac{n_L}{n_H})^{2p}} \right) \tag{2.28}$$

where the n_o and n_s are the refractive index of incident medium and substrate.

The high-reflectivity or stop band of a DBR depends on the difference in refractive index of the two constituent materials, Δn (n_H - n_L). The spectral width of the stop band is given by

$$\Delta\lambda_{stopband} = \frac{2\lambda_B \Delta n}{\pi n_{eff}} \tag{2.29}$$

where n_{eff} is the effective refractive index of the mirror. It can be calculated by requiring the same optical path length normal to the layers for the DBR and the effective medium. The effective refractive index is then given by

$$n_{eff} = 2(\frac{1}{n_H} + \frac{1}{n_L})^{-1} \tag{2.30}$$

The length of a cavity consisting of two metal mirrors is the physical distance between the two mirrors. For DBRs, the optical wave penetrates into the reflector by one or several quarter-wave pairs. Only a finite number out of the total number of quarter-wave pairs are effective in reflecting the optical wave. The effective number of pairs seen by the wave electric field is given by

$$m_{eff} \approx \frac{1}{2} \frac{n_H + n_L}{n_H - n_L} \tanh(2m \frac{n_H - n_L}{n_H + n_L}) \tag{2.31}$$

For very thick DBRs ($m \to \infty$) the tanh function approaches unity and one obtains

$$m_{eff} \approx \frac{1}{2} \frac{n_H + n_L}{n_H - n_L} \tag{2.32}$$

Also, the penetration depth is given by

$$L_{pen} = \frac{L_1 + L_2}{4r} \tanh(2mr) \tag{2.33}$$

where $r = (n_1-n_2)/ (n_1+n_2)$ is the amplitude reflection coefficient.

For a large number of pairs ($m\rightarrow\infty$), the penetration depth is given by

$$L_{pen} \approx \frac{L_1 + L_2}{4r} = \frac{L_1 + L_2}{4}\frac{n_H + n_L}{n_H - n_L} \quad (2.3\ 4)$$

Comparison of Eq. (2. 3 2) and Eq. (2. 3 4) yields that

$$L_{pen} = \frac{1}{2} m_{eff} (L_1 + L_2) \quad (2.3\ 5)$$

The factor of (1/2) in Eq. (2. 3 5) is due to the fact that m_{eff} applies to effective number of periods seen by the electric field whereas L_{pen} applies to the optical power. The optical power is equal to the square of the electric field. The effective length of a cavity consisting of two DBRs is thus given by the sum of the thickness of the center region plus the two penetration depths into the DBRs.

2-2.2 Reflectance simulation of Ta_2O_5/SiO_2 and nitride-based DBRs

The simulation of nitride-based DBRs [8]

To determine how many pairs DBRs are required for a VCSEL, the realization of reflectivity spectra of DBR is inevitable and necessary. In the following, we simulate and discuss the reflectance of bottom and top reflectors we used, AlN/GaN and Ta_2O_5/SiO_2 DBRs, to understand the DBR pairs we required at least to deposit for a VCSEL. Reflectivity spectra of DBR structures here were simulated using the transfer matrix method. The incident angle of illumination and wavelength of the reference light were set to be 0° (the direction normal to the sample surface) and 410nm, respectively.

AlN/GaN DBRs

The refractive index of GaN and AlN at wavelength of 410 nm, used as the parameters in the simulation, were n_{GaN} = 2.45 and n_{AlN} = 2.05. Figure 2. 4 shows the reflectance spectrum of 5, 10, 15, and 25 pairs of AlN/GaN DBR. The reflectivity value at center wavelength rapidly rises with the increasing of used pairs. As the pairs of DBR were 25 pairs, AlN/GaN DBR could theoretically achieve a high reflectivity of 99% at 450 nm and a wide stop-band about 46nm. The superiority of the AlN/GaN DBR also

could be further confirmed using the simulation. Figure 2. 5 shows the reflectivity spectra of three different nitride-based DBRs, AlN/GaN DBR, $Al_{0.25}Ga_{0.75}N$/GaN DBR, and $Al_{0.35}Ga_{0.65}N$/GaN DBR, with high reflectivity larger than 99% at 450 nm. Other two DBRs with low aluminum contents both show large required pairs (>50 pairs) and small stop-band (<20 nm). Compared to those nitride reflectors, the AlN/GaN DBR obviously reveals relatively wide stop-band and high reflectivity with relatively few pairs.

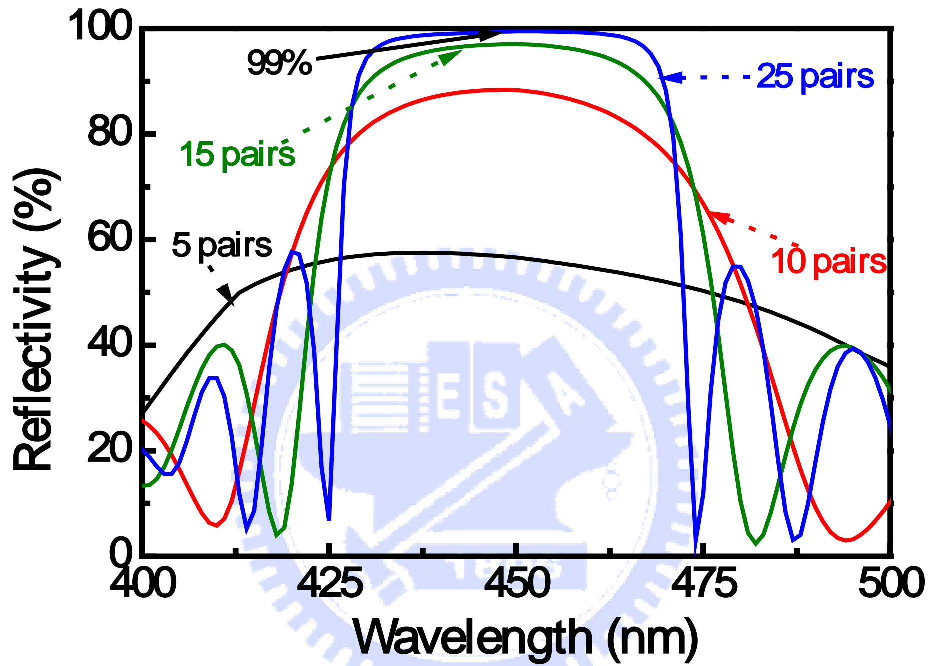

Figure 2. 4 Simulated reflectivity spectra of 5, 10, 15, and 25 pairs of AlN/GaN DBRs

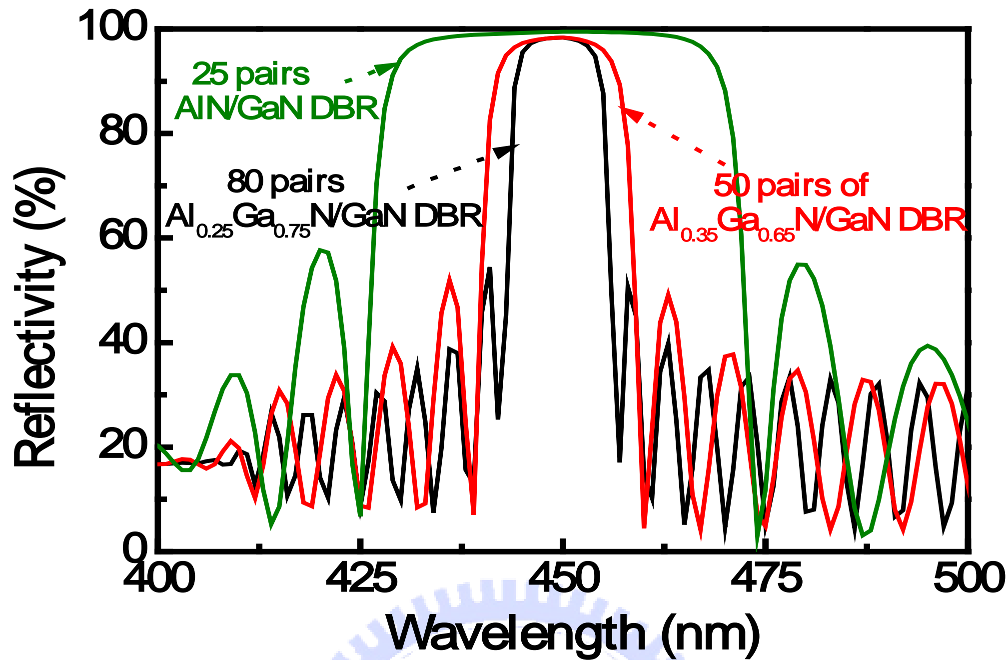

Figure 2. 5 Simulated reflectivity spectra of three different nitride-based DBRs with high reflectivity

Ta_2O_5/SiO_2 DBRs [9,10]

Dielectric mirror has the advantage of the large refractive index contrast between two different dielectric materials so it only needs a few pairs of DBR to form high reflectivity mirror. In most dielectric DBRs, SiO_2 is usually used as the low refractive index material due to its some advantaged characteristics such as relative low refractive index than many other dielectric materials. It is easy and cheap to get, hard to decompose, and high transparent window from the wavelength of 180 nm to 8 μm. As to the high refractive index material, Ta_2O_5 is a proper selection owing to benefits of low absorption and high transparency in visible to IR ray. The refractive index of SiO_2 and Ta_2O_5 at wavelength of 450 nm, used as the parameters in the simulation, are n_{SiO2} = 1.463 and n_{Ta2O5} = 2.15. Figure 2. 6 shows the reflectance spectrum of 3, 5, and 8 pairs of Ta_2O_5/SiO_2 DBR. The 8 pairs of Ta_2O_5/SiO_2 mirror can have a high reflectivity of 99% and the wide stop band about 128 nm. Therefore, we use at least 8 pairs of Ta_2O_5/SiO_2 DBR as the top mirror in the following experiments.

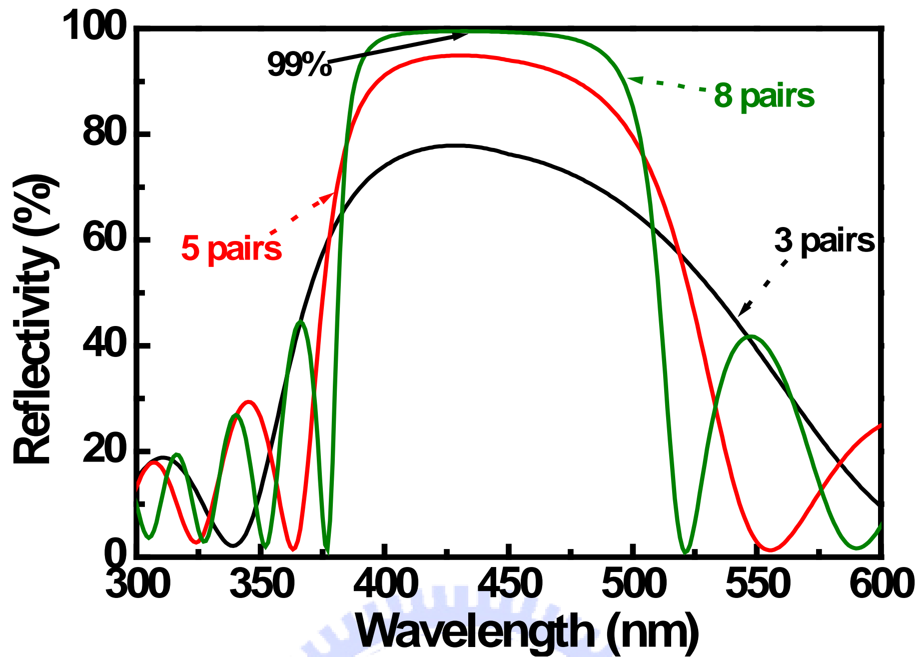

Figure 2. 6 Simulated reflectivity spectra of 3, 5, and 8 pairs of Ta_2O_5/SiO_2 DBRs.

2-3 Design of GaN-based VCSELs [11-13]

The design of a typical VCSEL structure should consider three dominant components: the micro-cavity length, the location of active region, and how many pairs of DBR layers we should coated. To achieve lasing action of VCSEL, a careful evaluation and design for the active region and the DBRs are quite important. In this section, we discuss the design of nitride-based VCSEL with hybrid cavity. The hybrid cavity is a cavity sandwiched by an epitaxial grown AlN/GaN DBR and a Ta_2O_5/SiO_2 dielectric DBR. The design for each component in our VCSEL structure is determined by considering the analysis of the reflectance of DBRs and the electric field distribution inside our structure. The cavity length was designed to be seven-lambda in optical length (λ~410 nm). In addition to the consideration of high-reflectivity mirror, the location of active region, usually in the form of MQWs, is also an important issue to the fabrication of GaN-based VCSEL. The active region plays a role of the gain medium. How to effectively make photons to oscillate with active medium is an important consideration. If we put the gain medium at the node of optical field, the interaction between light and

electrons would be very weak, therefore, the gain medium couldn't efficiently provide gain for lasing action. On the contrary, the lasing threshold would be significantly lowered if the active region was put at anti-node of optical field. The same mechanism can be applied in other component of the cavity.

For the electrical pumped VCSEL structure, the ITO layer as a current spreading layer should be considered as one important part of the whole cavity because it would increase the absorption when light resonates in the cavity region. In order to reduce the absorption of the ITO layer, there are two methods can achieve the effect. The first one is using the thinner ITO layer to reduce the absorption in the whole cavity. The second one is designed at the node of optical field, shows opposite views of the MQWs. Then we would introduce the simulation results of these two methods to achieve the better design in our VCSEL structure.

<u>The reflectance and quality factor simulation with different ITO thickness</u>

Before proceeding with the experiment, we first simulate the reflectance spectra with different thickness of ITO layer. Figure 2. 7 shows the simulation cavity structure with different ITO layer thickness from 0 nm, 30 nm, 120 nm, 210 nm, and 225 nm. Here, the 225nm-thick ITO layer stands for one optical wavelength thickness at 440nm. Owing to DBR reflectivity symmetry, then we chosen 18-pair AlN/GaN DBR. Figure 2. 8 is the simulated reflectance spectra under different ITO thickness. The dip positions in the reflectance spectra represent the cavity modes with different ITO thickness and the quality factor can be estimated from the linewidth of the dip. In Figure 2. 9, the cavity mode wavelength is the function of different ITO thickness. The cavity mode wavelength shifts to longer wavelength because of the longer cavity length, but the cavity mode wavelength would turn back to shorter wavelength when ITO thickness is thicker than 120nm due to the exceeding of the stop band region of the lower DBR. In this case, the cavity mode would jump to the $(m+1)_{th}$ mode from the m_{th} mode. Furthermore, the cavity mode also changes to multimode owing to longer cavity length and smaller mode spacing when ITO thickness is larger than 30nm. In Figure 2. 10, the quality factor is about 700 using the cavity with a 225nm-thick ITO layer, but this value is much lower than that without ITO layer of about 3300. If we consider the qualify factor of the cavity with a

30nm-thick ITO layer, the value of about 3100 is a little smaller than that with a 0nm-thick ITO layer but the structure with a ITO layer can be efficiently injected current in our electrical pumped VCSEL devices. Based on the simulation results and reality device requests, we can expect the 30nm ITO layer can efficiently reduce the loss and threshold current density of our VCSEL devices.

Figure 2. 7 The simulation cavity structure

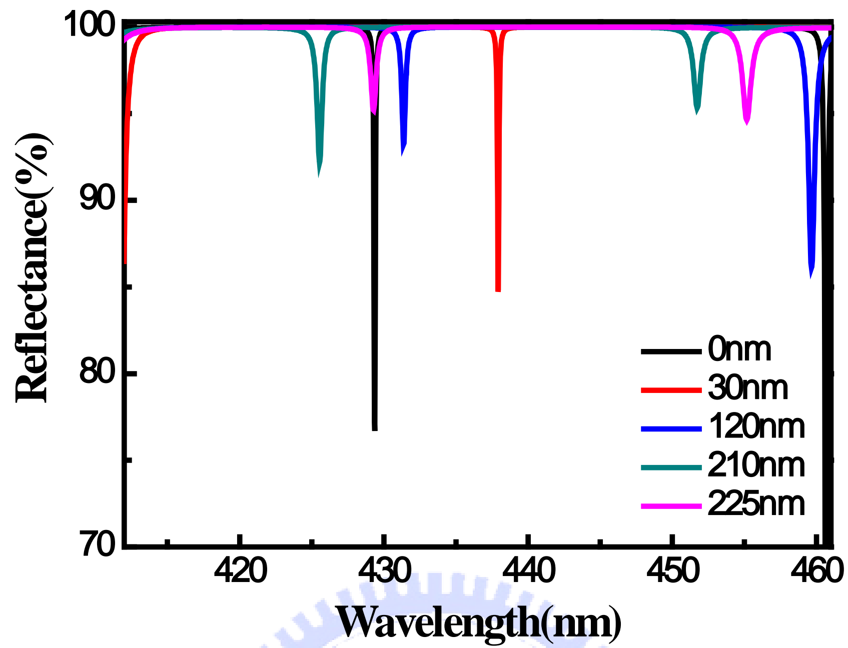

Figure 2. 8 The simulated reflectance spectra with different thickness of ITO

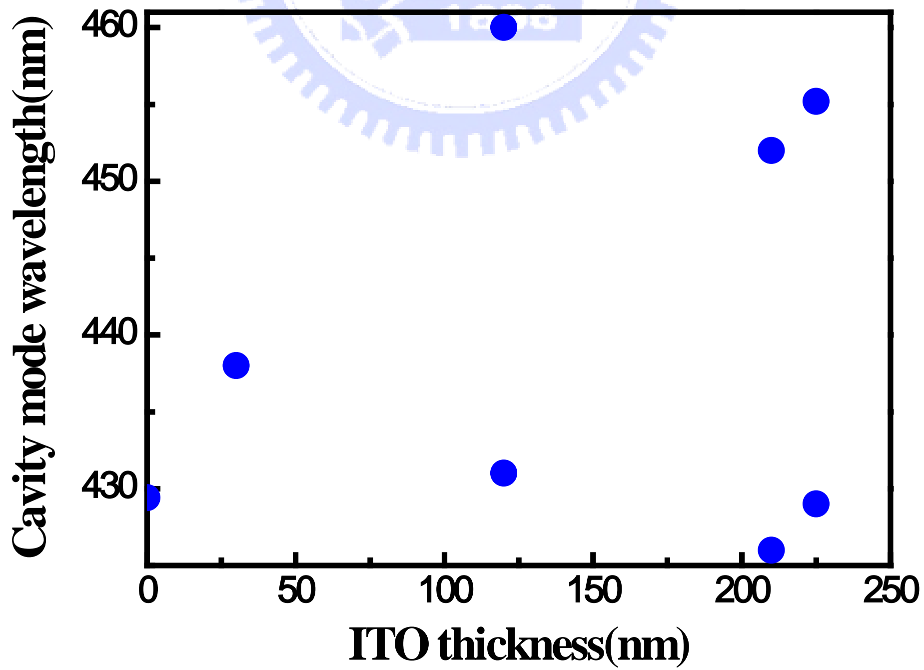

Figure 2. 9 the simulated cavity modes with different thickness of ITO

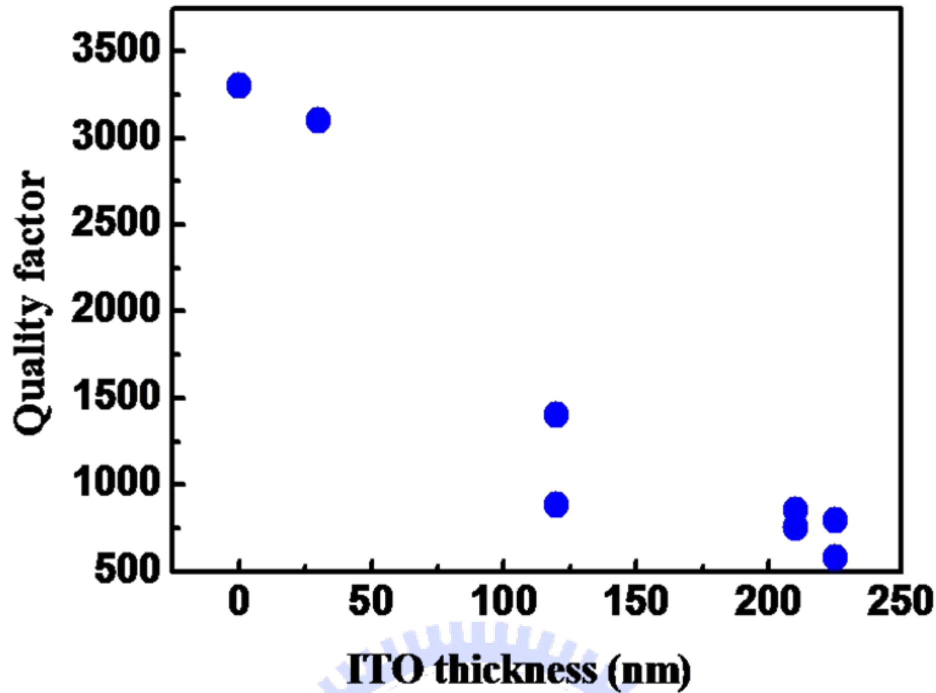

Figure 2. 10 The simulated quality factors with different thickness of ITO

1896

The design of electrical pumped VCSELs

For a typical VCSEL, the cavity length is designed to be 1 λ or 3/2 λ, so the antinode of optical field and active region could be easily designed to match each other. However, in our design, the cavity length has been determined to be seven-λ (optical length), which correspond to a geometric thickness of about 1.1 μm, due to the consideration of device fabrication. The structure should compose of a top dielectric reflector, an ITO layer, a p-type GaN, MQWs, an n-type GaN, and a bottom nitride-based reflector. The optimal thickness of the ITO layer to be about 30 nm, the p-type InGaN to be about 2 nm, the p-type GaN to be about 110 nm, of the p-type AlGaN as a electron blocking layer to be about 24 nm, of 10-pair $In_{0.2}Ga_{0.8}N$(2.5 nm)/GaN(12.5nm) multi-quantum wells (MQWs) to be about 150 nm, and of the n-type GaN to be about 860 nm, and slightly modified these thicknesses to make the center of MQWs and the ITO layer at the anti-node and node of optical field, respectively. Figure 2. 11 shows the electric field intensity (EFI) and the refractive index as the functions of the distance from top layer. From the figure, it can be observed that a pronounced resonant enhancement of

the electric field was built up in the active region. It suggests that the light could be amplified inside the resonant cavity and the more opportunity could be obtained to achieve laser operation.

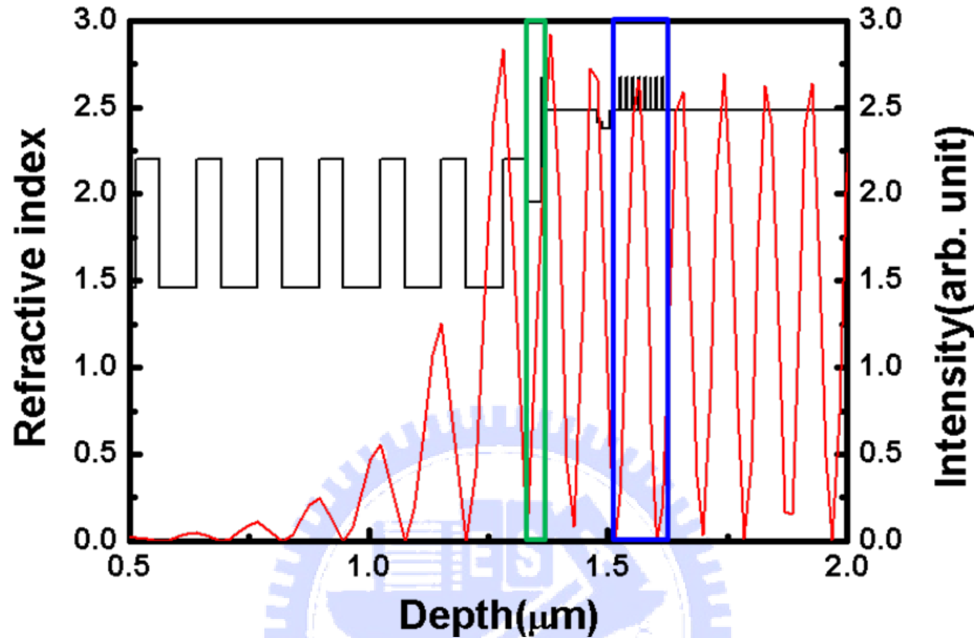

Figure 2. 11 Electric field intensity and refractive index as a function of the distance from top layer.

2-4 Fabrication of GaN-based VCSELs

The nitride-based structures including micro-cavity and bottom reflector in the experiments were grown in a vertical-type metal-organic chemical vapor deposition (MOCVD) system (EMCORE D-75) with a fast rotating disk, which can hold one 2-inch wafer. The polished optical-grade C-face (0001) 2-inch-diameter sapphire was used as substrate. Trimethylindium (TMIn), Trimethylgallium (TMGa), Trimethylaluminum (TMAl), and ammonia (NH_3) were used as the In, Ga, Al, and N sources, respectively. In this section, the fabrication of the nitride-based VCSEL is divided into two parts: (1) Growth of nitride-based reflectors and micro-cavity. (2) Deposition of dielectric mirror.

2-4.1 Growth of nitride-based reflectors and micro-cavity

The nitride-based DBR used in the experiment is the stacks of 29-pair AlN/GaN

layers with insertion of the AlN/GaN super-lattice (SL). The super-lattice in structure is inserted for releasing strain during the growth of AlN/GaN DBR to further improve interface and raise reflectivity of the DBR. The growths and characteristics of the DBR and micro-cavity are described as following:

First, the substrate was thermally cleaned in the hydrogen ambient for 5 min at 1100 °C, and then a 30 nm-thick GaN nucleation layer was grown at 500°C. The growth temperature was raised up to 1100 °C for the growth of a 2 μm-thick GaN buffer layer. The subsequent epitaxial structure consisted of a 29-pair of quarter-wave AlN/GaN DBR grown at 1100 °C, a 7-lamda cavity (λ = 410 nm) including a 860 nm-thick Si-doped n-GaN layer, 10 pairs $In_{0.2}Ga_{0.8}N$/GaN (2.5 nm/12.5 nm) MQWs, a 24 nm-thick AlGaN layer as the electron blocking layer, a 110 nm-thick Mg-doped p-GaN layer, and a 2 nm-thick p^+ InGaN layer as the contact layer. The AlGaN electron blocking layer was served to reduce the electron overflow to the p-GaN layer.

For the DBR structure, in order to reduce the crack problems encountered in the AlN/GaN DBRs, we inserted one AlN/GaN superlattice into each five DBR periods at first twenty pairs of DBR. Then the superlattice was inserted into each three DBR periods for the remaining nine pairs of DBR to reduce the tensile strain. The thicknesses of AlN and GaN layers are ~3–5 nm in SL. The ambient gas was changed from hydrogen into nitrogen before the DBR layers were grown. The center wavelength of these DBRs was designed to be around 410 nm. The detail of the growth was reported elsewhere [14].

Figure 2. 12(a) shows cross-sectional transmission electron microscopy (TEM) images of the SL sample. The lighter layers represent AlN layers while the darker layers represent GaN layers. In Figure 2. 12 (a), no cracks can be observed in the TEM image. However, some V-shaped defects dark spots were still observed on the interfaces of GaN or AlN layers in Figure 2. 12 (a). These V-shaped defects have been reported earlier to be due to various origins such as stacking mismatch boundaries and surface undulation [23]. Figure 2. 12 (b) shows the cross section of one set of 5.5 pairs of GaN/AlN SL insertion layers. The interface between GaN and AlN is sharp and abrupt. Figure 2. 13 shows the AFM image of the DBR. The surface is lumpy, and the drop in height is within the range of 10-30 nm. The reflectivity spectrum of the AlN/GaN DBR is shown in Figure 2. 14. It shows the highest reflectivity of the DBR is about 99% at 416 nm. The stop-band of the

DBR is as wide as about 25 nm. Figure 2. 15 is (a) the OM and (b) cross-sectional TEM images of the as-grown micro-cavity sample.

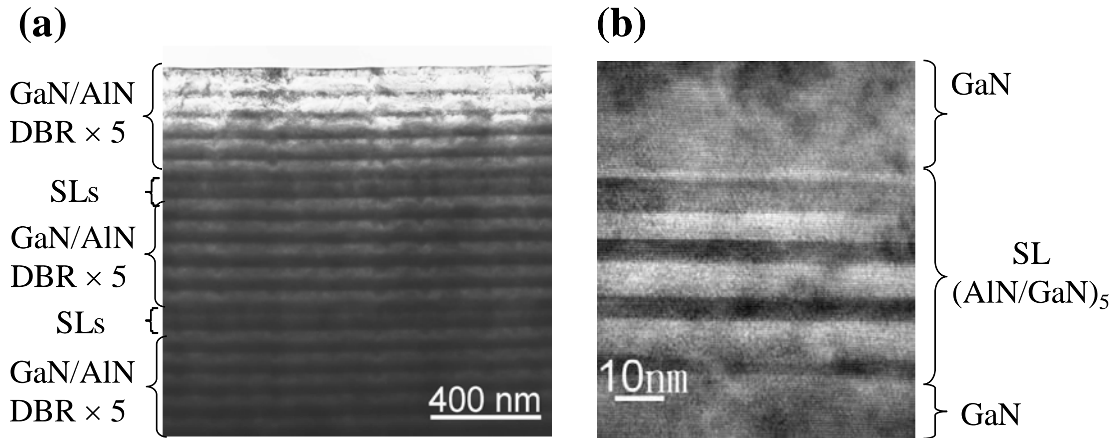

Figure 2. 12 Cross-sectional TEM images of (a) the DBR sample and (b) one set of 5.5 pairs of GaN/AlN SL insertion layers.

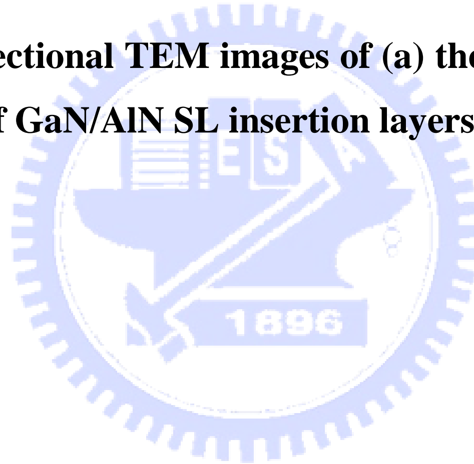

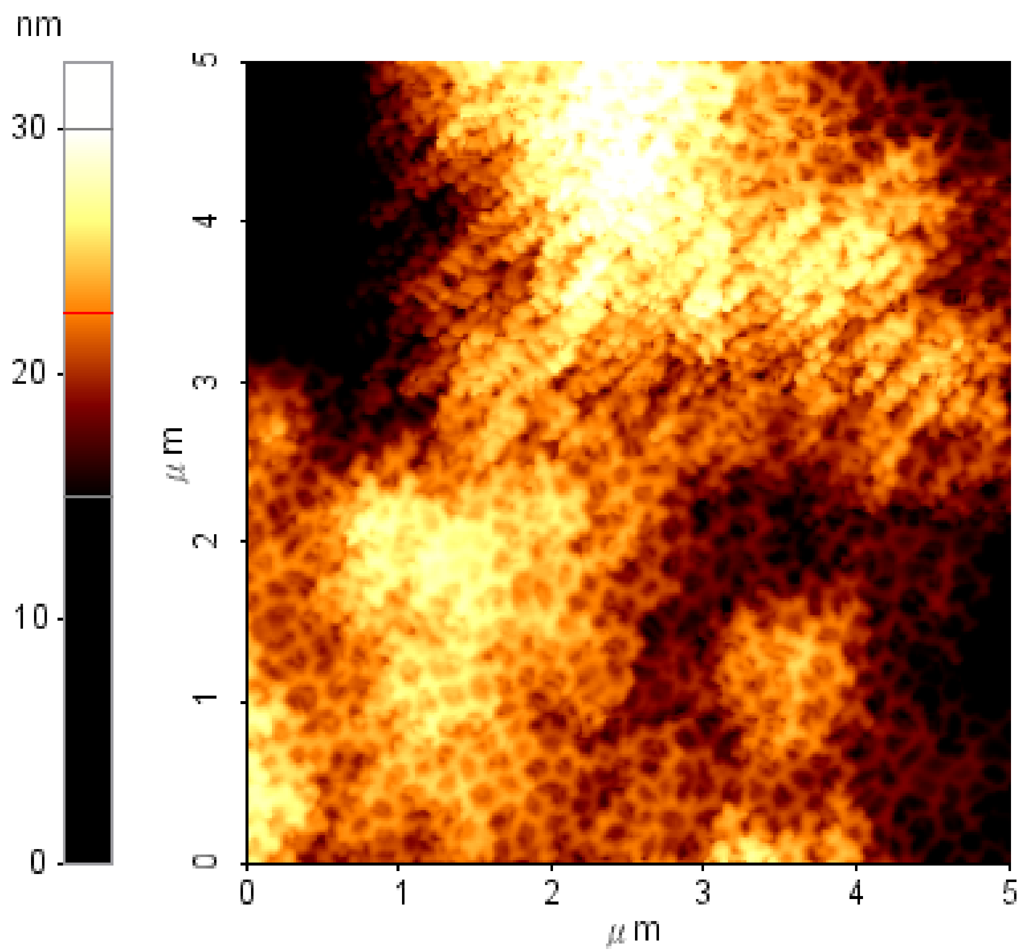

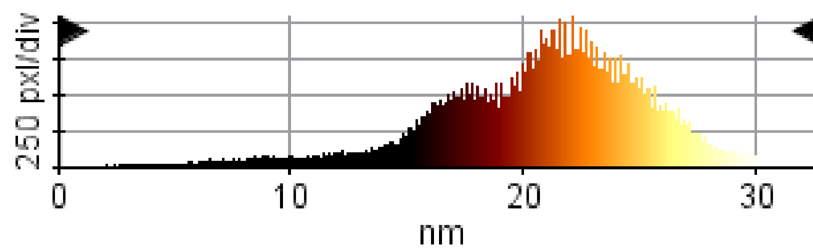

Figure 2. 13 AFM image of the DBR sample

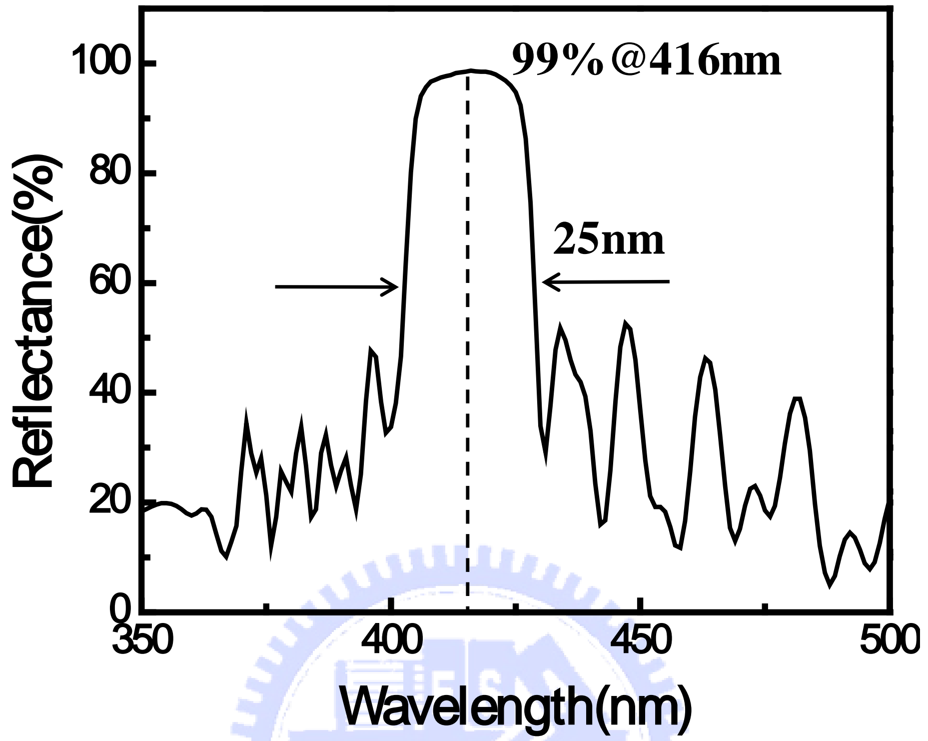

Figure 2. 14 The reflectivity spectrum of the AlN/GaN DBR

1896

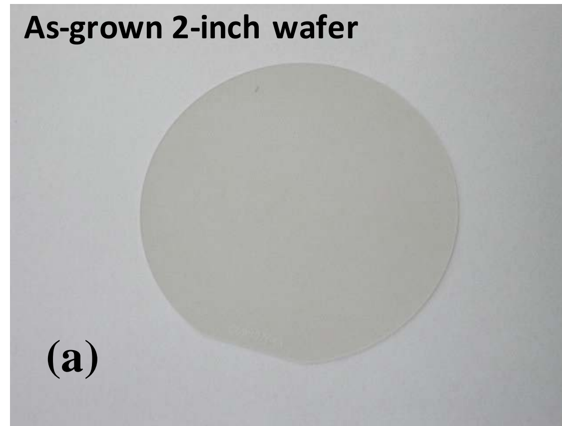

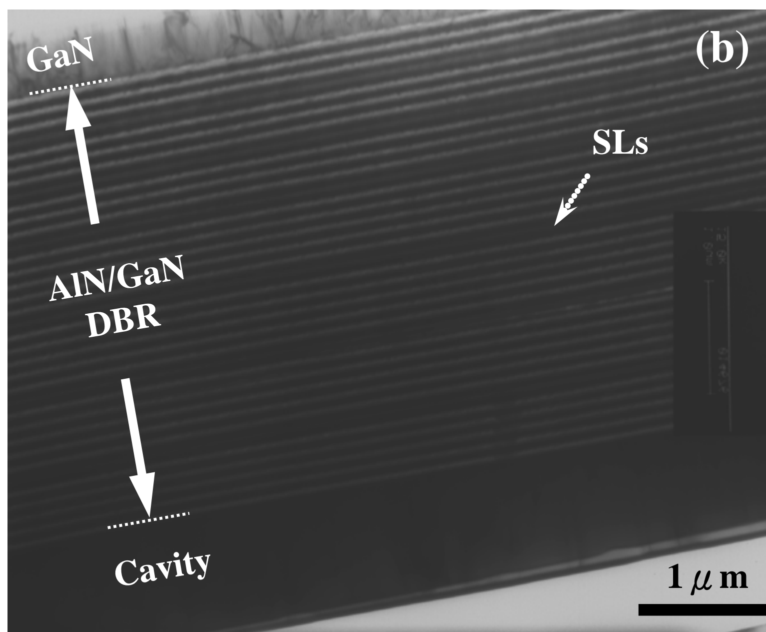

Figure 2. 15 (A) OM and (B) cross-sectional TEM images of the as-grown micro-cavity sample.

2-4.2 Deposition ofdielectric mirrors

The final process to complete an optical pumped VCSEL is the deposition of a dielectric mirror. The dielectric mirror in the experiment, an eight pairs Ta_2O_5/SiO_2 DBR, was deposited using the electron beam evaporation. The dielectric mirror was coated onto as-grown sample surface in an O_2 ambient at the controlled temperature below 170°C. The reflectivity spectrum of the dielectric mirror was measured as shown in Figure 2. 16.

The Ta_2O_5/SiO_2 DBR shows a very high reflectivity as high as 99% centered at 451 nm with a wide stop-band of about 130 nm. The schematic diagram of the overall VCSEL structure is shown in Figure 2. 17(a). The scanning electron microscopy (SEM) and OM images of the overall VCSEL structure are also shown in the Figure 2. 17(b) and (c), respectively.

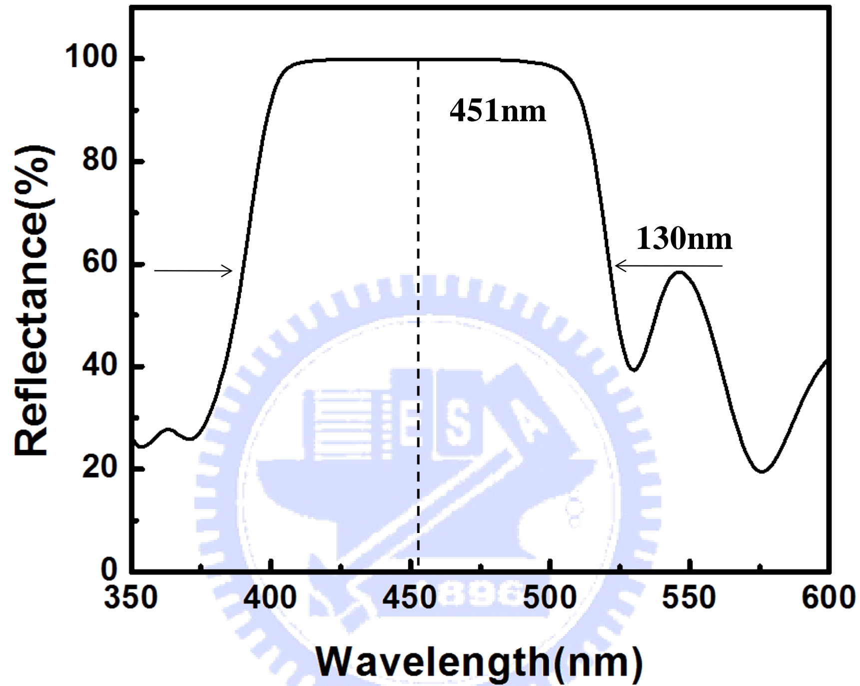

Figure 2. 16 The reflectivity spectrum of the Ta_2O_5/SiO_2 DBR

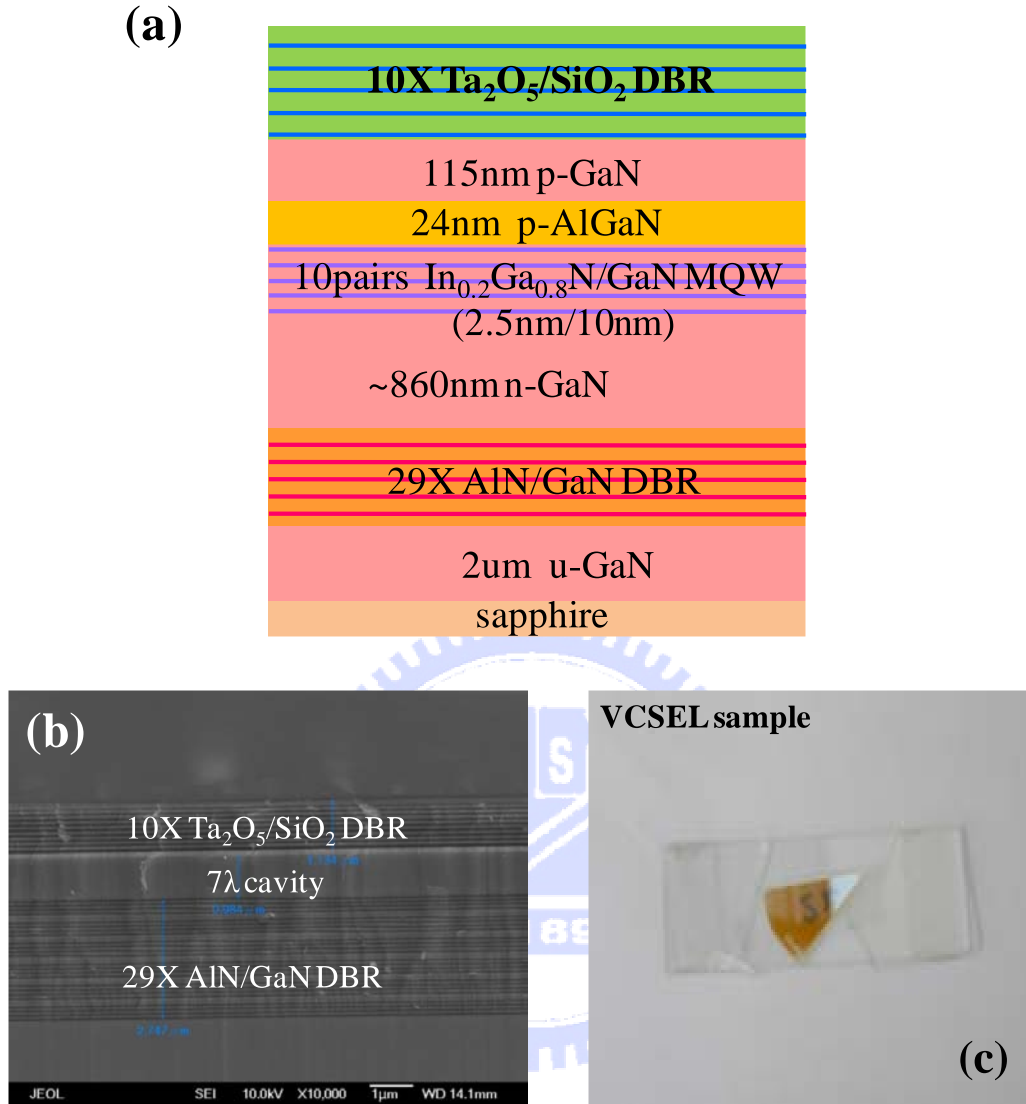

Figure 2. 17 (A) Schematic diagram, (B) SEM image, and (C) OM images of the VCSEL structure.

2-4.3 Fabrication processes for GaN-based VCSELs

Figure 2. 18 shows a process flowchart for a nitride-based VCSEL. The processes for a GaN-based hybrid-cavity VCSEL include steps: (1) definition of mesa area, (2) definition of current aperture, (3) coating of transparent contact, (4) deposition of p, n contact, and (4) deposition of top DBR. Figure 2. 19(a) shows the schematic diagram of the whole GaN-based VCSEL structure. In the structure, the positions of the ITO layer and MQWs region are located at the node and anti-node positions of the electric field

respectively to reduce the absorption from the ITO layer and to further increase the coupling between the electric field and MQWs region.

(1) As-grown sample

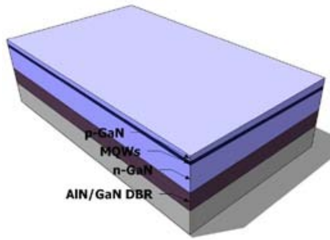

(2) Mesa etching

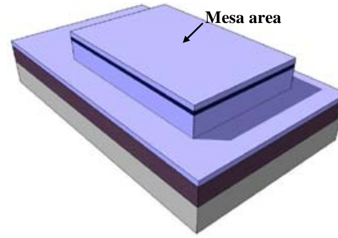

(3) pasivation

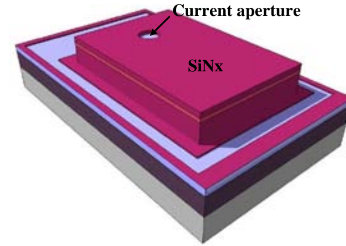

(4) ITO

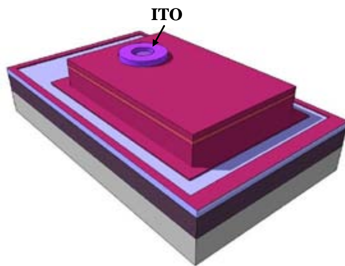

(5) p, n metal

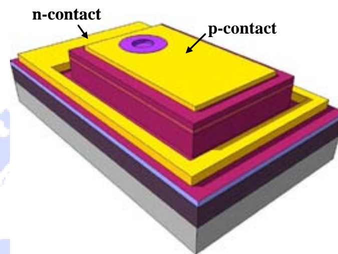

(6) Dielectric mirror

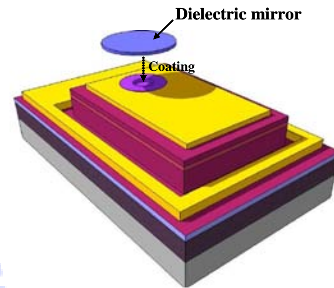

Figure 2. 18 The process flowchart of nitride-based micro-cavity devices.

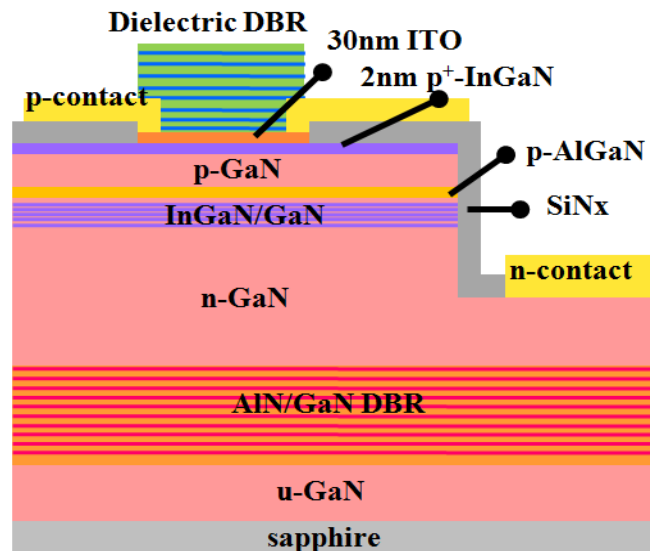

Figure 2. 19 The schematic diagram of the overall GaN-based VCSEL structure with hybrid mirrors.

The process of VCSEL devices began with the deposition of a 0.3 μm-thick SiN_x etching mask by plasma enhanced chemical vapor deposition (PECVD) and the definition of mesa region by photo-lithography. The mesa etching was then performed with Cl_2/Ar as the etching gas in an inductively coupled plasma reactive ion etching (ICP-RIE) system with the ICP power and bias power operated at 13.56 MHz. After removing the etching mask, we re-deposited and patterned a 0.2 μm-thick SiN_x layer to define a current aperture from 5 μm to 30 μm. Then, a 30 nm-thick ITO layer was deposited as the current spreading layer by an e-gun due to the poor conductivity of the p-GaN layer and annealed at 600 ^{o}C for 10 min by rapid thermal annealing. Here, the ITO layer consisted of a 10 nm amorphous ITO layer and a 20 nm crystalline RT ITO layer was employed an ohmic contact. Only 2 % of absorption was obtained at 420 nm after annealing as shown in Figure 2. 20. The contact between ITO and p-GaN was nearly ohmic, and the contact resistance was about $9.4*10^{-4}$ ohm-cm as shown in Figure 2. 21.

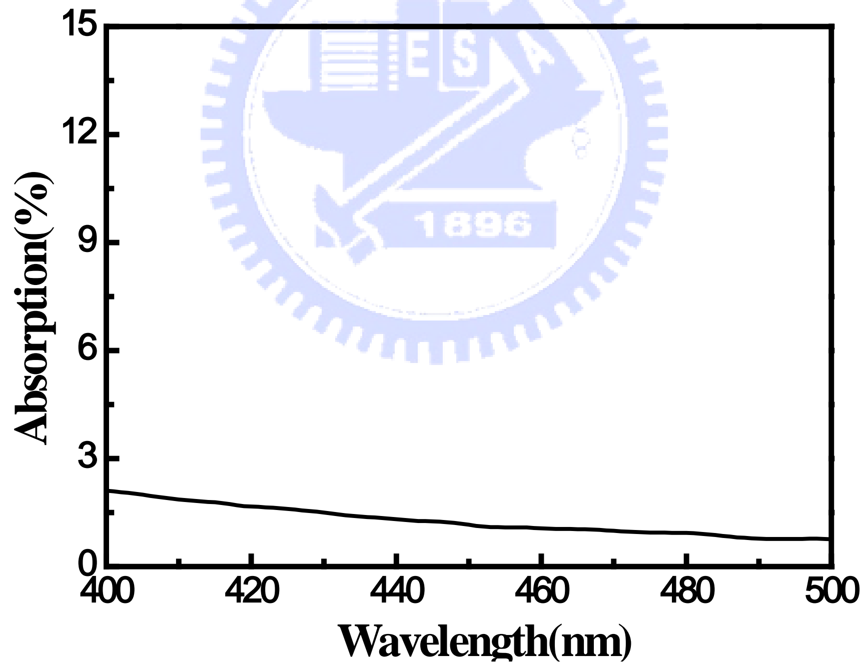

Figure 2. 20 The absorption of the 30nm-thick ITO layer

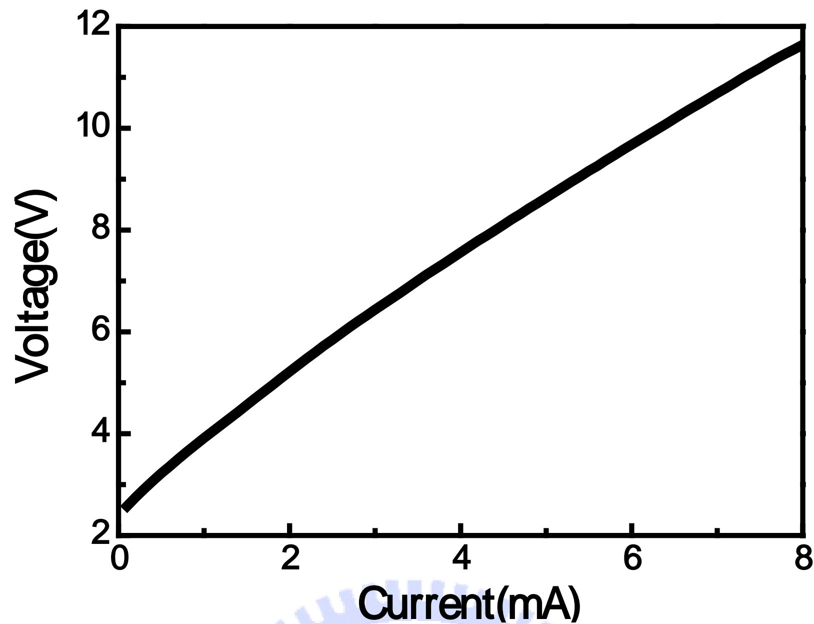

Figure 2. 21 I-V curve of the 30nm ITO layer and the p-GaN layer

The 2 nm-thick p^+ InGaN layer on the p-GaN surface can further reduce the series resistance between the thin ITO layer and the p-GaN layer with a slight increase of absorption. Then, the p-contact and n-contact were patterned by a lift-off procedure and deposited with Ni/Au of about 20 nm/150 nm and Ti/Al/Ni/Au of about 20 nm/150 nm/20 nm/150 nm by the e-gun system, respectively. Finally, 10 pairs Ta_2O_5/SiO_2 of the top dielectric DBR were deposited by the ion-assisted e-gun system to complete the whole GaN-based VCSEL devices. The OM images of the fabricated devices without and with 2 mA current injection are shown in Figure 2. 22(a) and (b), respectively. Figure 2. 22 (c) show the array fabrication of the VCSEL devices.

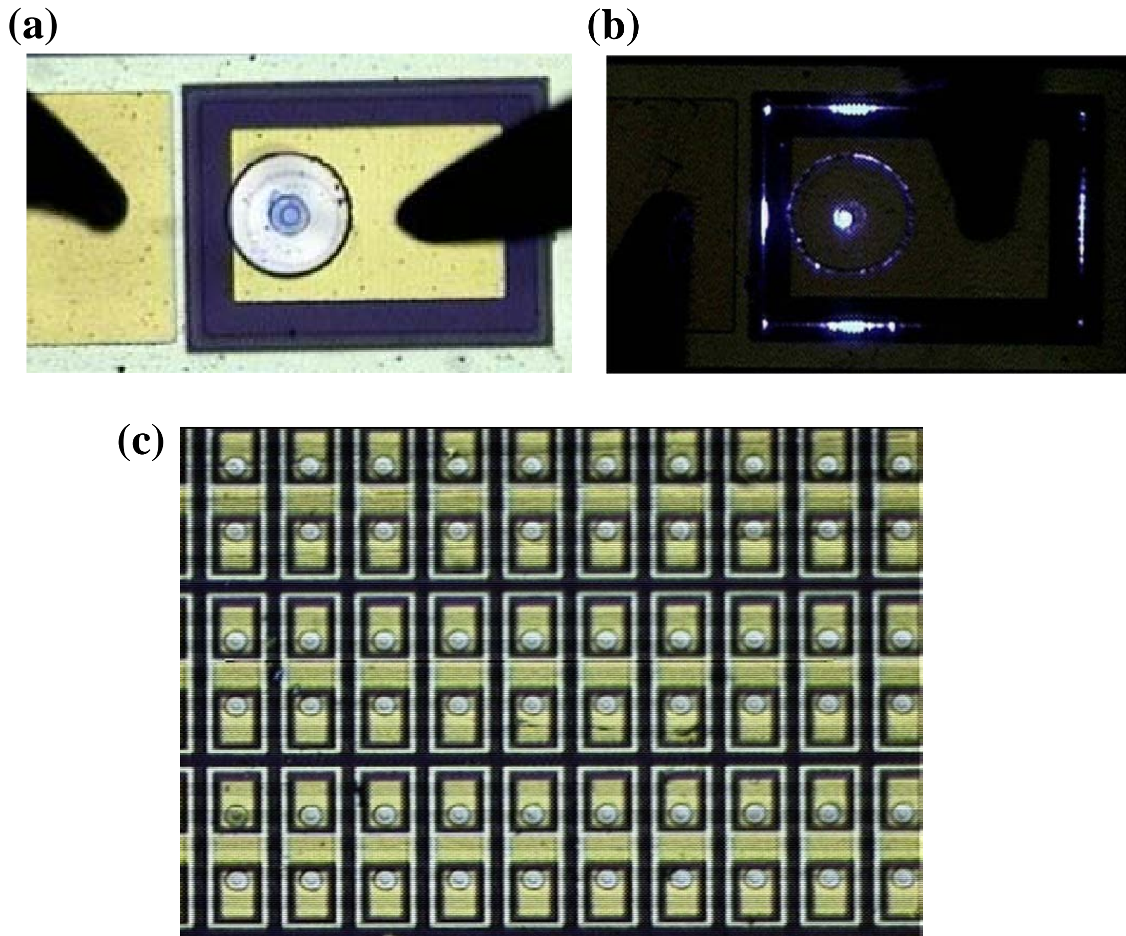

Figure 2. 22 OM images: (a) without current injection, (b) at 2 mA current injection, and (c) the array fabrication of the VCSEL devices.

References.

[1] Y. Yamamoto, S. Machida, and G. Björk, *Phys. Rev. A*, **44**, 657 (1991)

[2] Y. Suematsu and K. Furuya, *Trans Inst. Electron. Commun. Eng. Jpn.*, **E-60**, 467 (1969)

[3] S. Kako, T. Someya, and Y. Arakawa, *Appl. Phys. Lett.*, **80**, 722 (2002)

[4] H. Haug, *Phys. Rev.*, **184**, 338 (1969)

[5] H. E. Li and K. Iga, Vertical-Cavity Surface –Emitting Laser Devices, *Springer-Verlag, Berlin* (2003)

[6] C. W. Wilmsen, H. Temkin, L. A. Coldren, Vertical-Cavity Surface-Emitting Lasers, *Cambridge University Press* (1999)

[7] D. I. Babic and S. W. Corzine, *IEEE J. Quantum Electron.*, **28**, 514 (1992)

[8] G. W. Wood, U. Ozgur, H. O. Everitt, F. Yun, and H. Morkoc, *phys. stat. sol. (a)*, **188**, 793 (2001)

[9] 李正中，薄膜光學與鍍膜技術 (1999)

[10] E. D. Palik, Handbook of Optical Constants of Solids, *Academic Press Inc* (1985)

[11] P. Mackowwiak and W. Nakwaski, *J. Physics D: Applied Physics* **33**, 642 (2000)

[12] P. Mackowwiak and W. Nakwaski, *J. Physics D: Applied Physics* **34**, 954 (2001)

[13] P. Mackowwiak, T. Czyszanowski, R. P. Sarzala, M. Wasiak, and W. Nakwaski, *Opto-Electron. Rev.,* **11**, 119 (2003)

[14] G. S. Huang, T. C. Lu, H. H. Yao, H. C. Kuo, S. C. Wang, C. W. Lin and L. Chang, *Appl. Phys. Lett.*, **88**, 061904 (2006)

Chapter 3

Characteristics of Electrical Pumped GaN-Based VCSELs

3-1 Optical properties of GaN-based VCSELs

Photoluminescence of the VCSEL structure

In Figure 3. 1, the photoluminescence (PL) emission was excited by a 325 nm He-Cd laser with a spot size of about 2-μm-diameter. By using the microscopy system (WITec, alpha snom), the emission was collected into a spectrometer/CCD (Jobin-Yvon Triax 320 Spectrometer) with a spectral resolution of ~0.15 nm for spectral output measurement. The as-grown sample is consisted of a 7-lamda optical cavity and bottom AlN/GaN DBR.

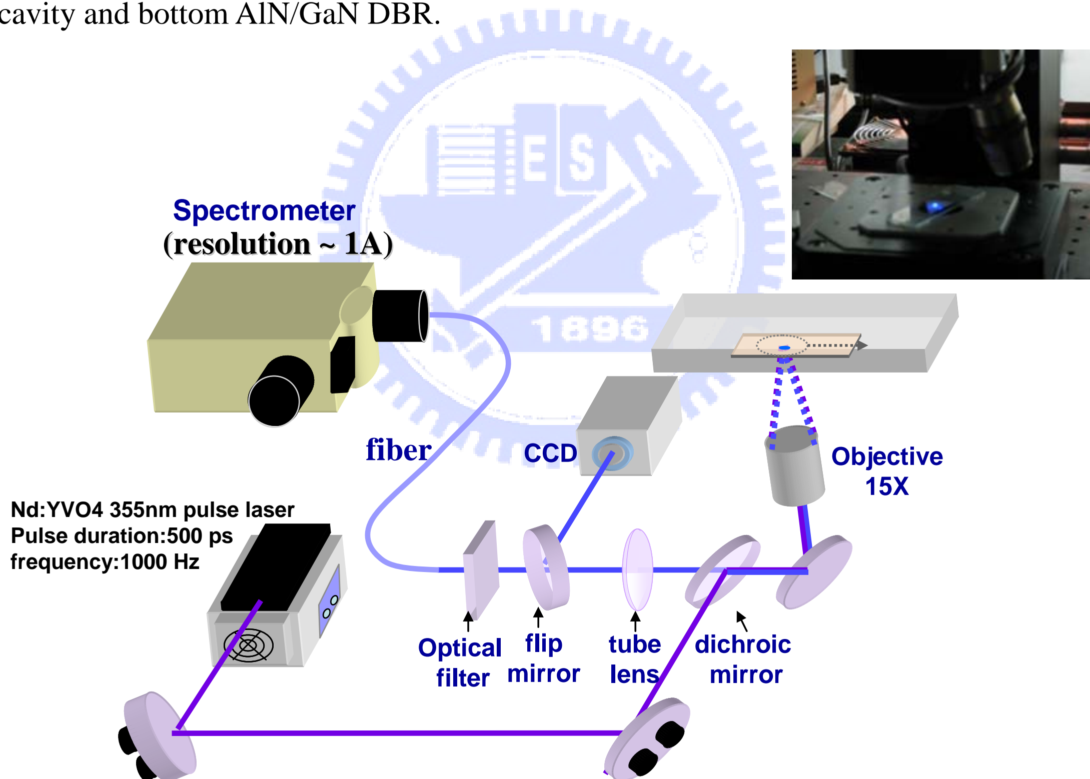

the PL emission and the FWHM of emission spectrum of overall VCSEL structure became 437.5 nm and 0.23 nm, respectively. It is obvious that the PL emission peak wavelength of overall VCSEL structure was modified by cavity mode, which could be seen from the reflectivity spectrum of as-grown sample (the dip in stop-band), and centered at 437 nm. The narrow FWHM of 0.23 nm is an evidence of the strong Febry-Perot cavity effect existing in our VCSEL sample. Besides, the cavity mode in our VCSEL structure would shift from 410 nm to 440 nm due to the non-uniform bottom DBR. In the following section, we will observe different laser devices with various lasing wavelength.

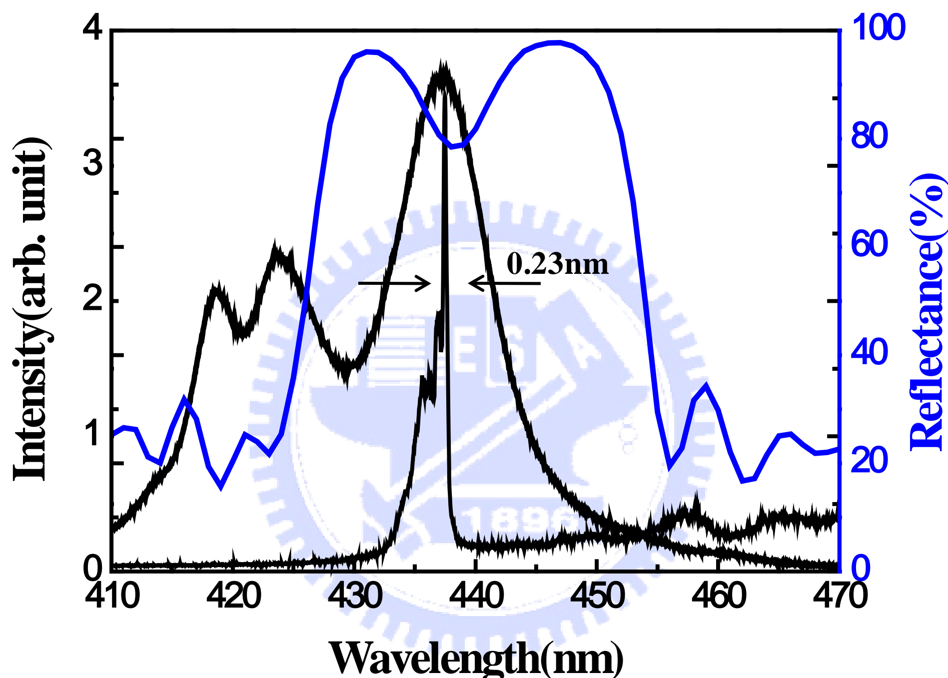

Figure 3. 2 PL emission spectra of as-grown sample and VCSEL structure, and the reflectivity spectrum of as-grown sample.

<u>**Quality factor of the VCSEL structure**</u>

A narrow PL emission with full width at half maximum of 0.23 nm corresponds to the cavity resonant mode at 437 nm was observed. It indicates the spontaneous emission generated from MQWs was well-aligned the narrow vertical-cavity mode resulting from the high reflectivity of AlN/GaN DBR and dielectric mirror. The cavity quality factor is a value usually used to evaluate how good a cavity is. Generally, the cavity quality factor is defined as $Q=\frac{\lambda}{\Delta\lambda}$, where λ is the wavelength emitted from cavity and $\Delta\lambda$ is the FWHM of the emission peak. Therefore, we could obtain the Q

value of our VCSEL structure to be about 1900. The value can be estimated by the following equation. However, this value has some inaccuracies because the theoretical estimation doesn't consider the ITO absorption in the whole cavity.

$$Q = \frac{2nL}{\lambda} \frac{\pi}{1 - \sqrt{R_1 R_2} e^{-\alpha L}} \qquad (3.\ 1)$$

where R_1, R_2 are the reflectivity of bottom and top reflectors, L is the cavity length, α is absorption coefficient of GaN, and n is refractive index of GaN. Here we consider the absorption loss in GaN at 440 nm is 1 - 200 cm^{-1} at 440 nm [1], and the high reflectivity of top and bottom reflectors are both 99% at 440 nm.

Optical pumping setup

The optical pumping of the sample was performed using a frequency-tripled Nd:YVO_4 355-nm pulsed laser with a pulse width of ~ 0.5 ns at a repetition rate of 1kHz. The pumping laser beam with a spot size of 60μm was incident normal to the VCSEL sample surface. The light emission from the VCSEL sample was collected using an imaging optic into a spectrometer/CCD (Jobin-Yvon Triax 320 Spectrometer) with a spectral resolution of ~0.15 nm for spectral output measurement. Figure 3. 1 shows the schematic diagram of the setup.

Threshold characteristics

The light emission intensity from the VCSEL as a function of the pumping energy is shown in Figure 3. 3 solid line. From the dash lines, a distinct threshold characteristic was observed at the threshold pumping energy (E_{th}) of about 500 nJ corresponding to an energy density of 2.9 mJ/cm^2 (threshold energy density is 1.2 mJ/cm^2 if considering some energy loss due to reflectivity of DBR). Then the laser output increased linearly with the pumping energy beyond the threshold. The carrier density at the threshold is estimated to be about 2×10^{19} cm^{-3}, assuming the reflectivity of the top mirror at pumping wavelength of 355 nm was 40 %, the absorption coefficient of the GaN was about 10^5 cm^{-1} at 355 nm [1] and the quantum efficiency was 10 % [2]. We estimated the threshold gain (g_{th}) of the VCSEL cavity using the equation:

$$g_{th} = (L_c / N_w L_w)\alpha_i + (1/2N_w L_w)\ln(1/R_1 R_2) \qquad (3.\ 2)$$

where L_c is effective cavity length (including penetration depth of DBR, which could be estimated using Eq. (2. 3 5), α_i is absorption coefficient of GaN at lasing

wavelength, N_w is the number of quantum wells, L_w is the width of each quantum well and R_1, R_2 are the reflectivity of the top and bottom mirrors, respectively. We obtained the required threshold gain is about 8.7×10^3 cm^{-1}. The parameters used in the estimations of carrier density at threshold and threshold gain are listed in the Table 3.1. The threshold gain value at the threshold carrier density is slightly lower than the gain value of Park's report [3].

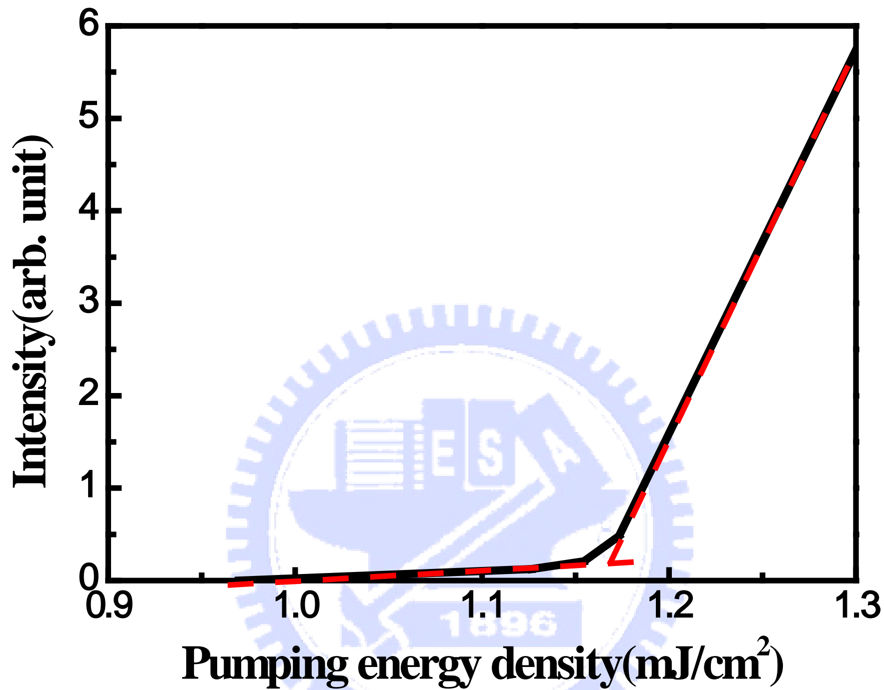

Figure 3. 3 The light emission intensity of the VCSEL as a function of the pumping energy density

Threshold energy density E_{th}	2.9 mJ/cm^2
The reflectivity of the top mirror at 355nm R_{355}	40%
The absorption (coefficient) of the p-GaN at 355 nm A_{355} (α_{GaN})	86.5% (10^5 cm^{-1})
The quantum efficiency η	10% [Science, **285**, 1905]
The effective cavity length L_c	1.6μm
The absorption coefficient of GaN at lasing wavelength α_i	100cm^{-1}
The number of quantum wells N_w	10
The width of each quantum well L_w	2.5nm
The reflectivity of the top mirrors R_1	99%
The reflectivity of the bottom mirrors R_2	99%

Table 3. 1 Parameters for the estimation of material gain.

Figure 3. 4 shows the variation of emission spectrum with the increasing pumping energy from 0.8 E_{th} to 1.1 E_{th}. A dominant laser emission line at 438.7 nm appears above the threshold pumping energy. The laser emission spectral linewidth reduces with the pumping energy above the threshold energy and approaches 0.35 nm above the pumping energy of 1.1 E_{th}.

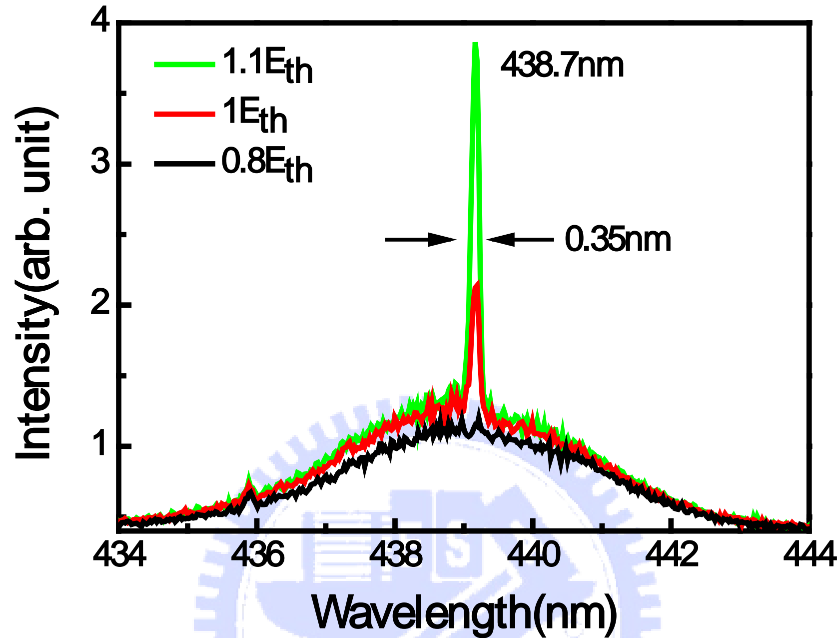

Figure 3. 4 Emission spectrums under different pumping energy density

The emission images under different pumping energy were shown in Figure 3. 5. The blue spontaneous emission could be seen as the pumping energy was below threshold. With the pumping energy increasing above threshold, a laser spot with relatively strong intensity appears, and the intensity of the spot rapidly increases. This result shows the nitride-based VCSEL is a spot-type laser.

Figure 3. 5 The emission images under different pumping energy

The coupling efficiency of spontaneous emission (*β*)

In order to understand the *β* of this cavity, we normalized the scales of Figure 3. 3 and re-plotted it in a logarithm scale as shown in Figure 3. 6. The spontaneous emission coupling efficiency *β* value is about $6*10^{-4}$.

This value of the VCSEL is one order of magnitude higher than that of the typical edge emitting semiconductor lasers (normally about 10^{-5}) [2, 4] indicating the enhancement of the spontaneous emission into a lasing mode by the high quality factor microcavity effect in the VCSEL structure.

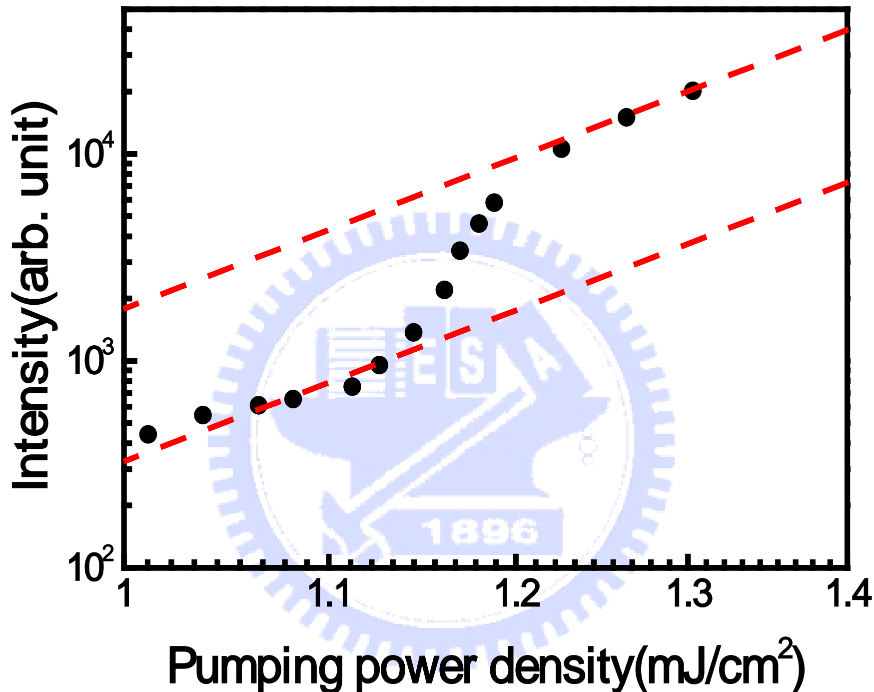

Figure 3. 6 The coupling efficiency of spontaneous emission (*β*)

3-2 Characteristics of electrically pumped GaN-based VCSELs

Electrical pumping setup

The electroluminescence (EL) characteristics of the fabricated VCSELs were measured by the probe station system and injected current by the Keithley 238 CW current source as shown in Figure 3. 7. Figure 3. 8 is the images of the low temperature EL measurement system. The light output power can be measured by Si-based optical power meter through an integrated sphere. The relative electrical characteristics, such as current-light output intensity(L-I) and current-voltage (I-V) properties, were performed by using the probe station, Keithley 238 CW Current Source, UV power detector, and Newport 1835-C optical power meter. The emission

light was then collected by a 25 μm-diameter multimode fiber using a microscope with a 40X objective and fed into the spectrometer/CCD (Jobin-Yvon Triax 320 Spectrometer) with a spectral resolution of ~0.15 nm for spectral output measurement. All the data could be directly feed backed to the computer from these facilities including the optical meter spectrometer and the Keithley 238 current source by the GPIB connector.

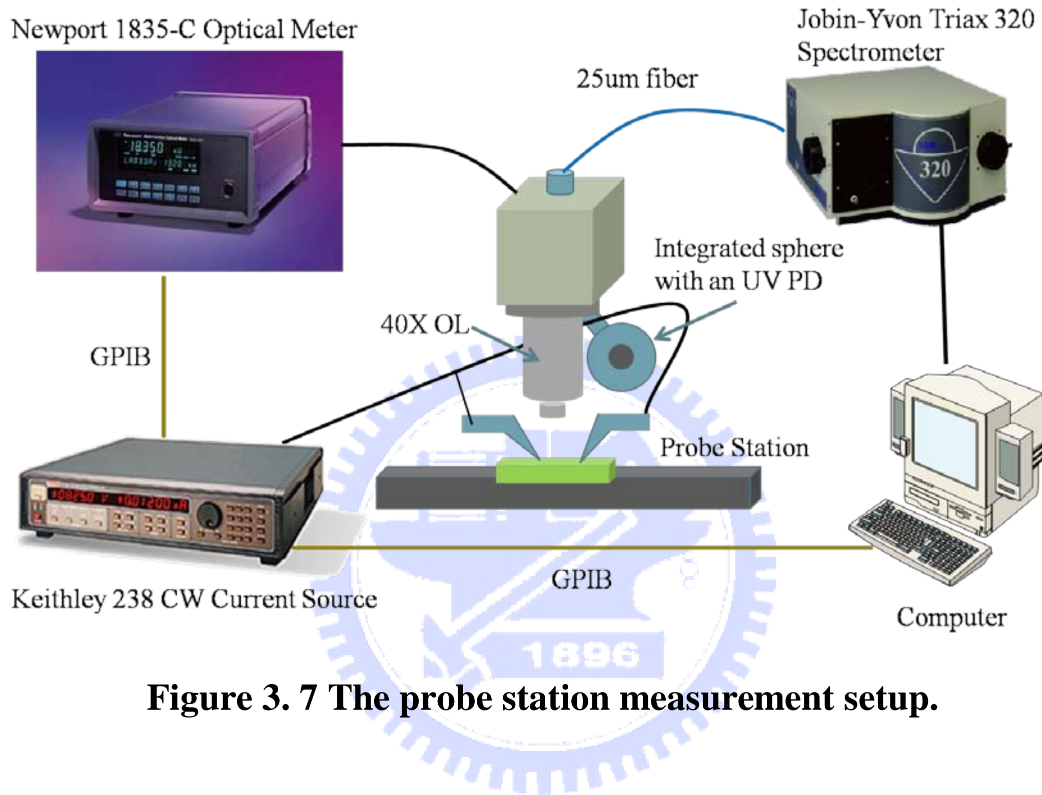

Figure 3. 7 The probe station measurement setup.

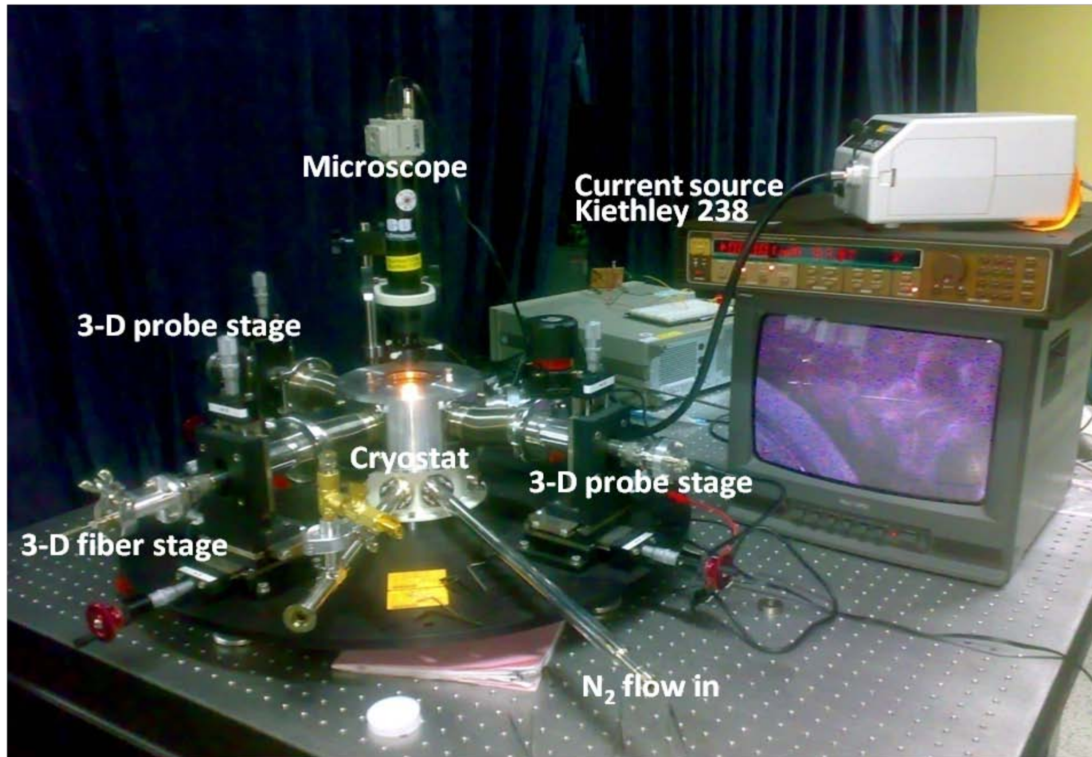

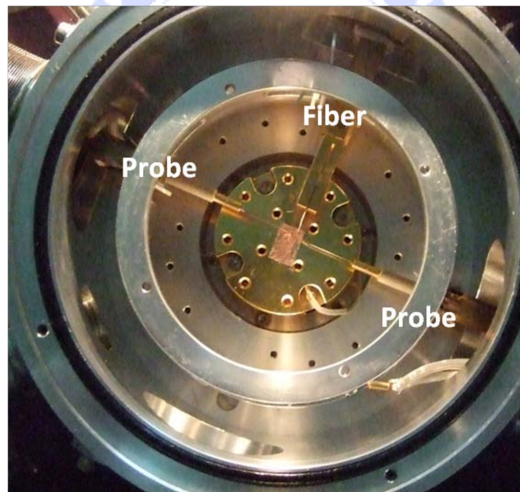

Figure 3. 8 The images of low temperature EL measurement system

<u>Threshold characteristics</u>

The light emission intensity from the VCSEL as a function of the injection current is shown in Figure 3. 9 at 200 K, 240 K, 270 K, and 300 K. All of them has a distinct threshold characteristic was observed at the threshold injection current (I_{th}) of about 7.5 mA (200 K), 8.2 mA (240 K), 9.2 mA (270 K), and 9.7 mA (300 K). At room temperature(300 K), the threshold current density is 11.4 kA/cm^2 similar to the result of the electrical pumped GaN VCSEL with double dielectric mirrors fabricated by Nichia company[5,6].

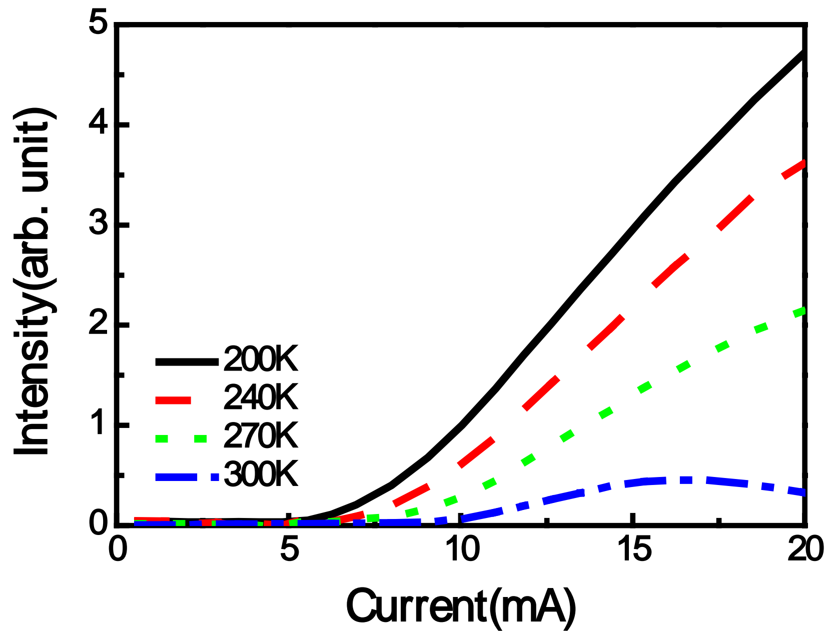

Figure 3. 9 The lasing intensity as a function of injection current under different measurement temperature from 200 K (solid line), 240 K (dash line), 270 K (dot line), and 300 K (dot dash line).

Figure 3. 10 shows the laser device voltage as a function of the injection current at 200 K, 240 K, 270 K, and 300 K. When we increased the measurement temperature from 200 K to 300 K, the series resistance and turn-on voltage of the laser device decreased from 220 Ω to 180 Ω and from 4.55 V to 4.3 V, respectively. In general, this might be caused by the worse hole mobility in p-GaN material in lower temperature (200 K) compared with the room temperature (300 K). In our experiment, the whole mobility in p-GaN material increased when the environment temperature rose to 300 K and further accelerated the recombination of the holes and the electrons. Therefore, the series decreases in higher measurement temperature.

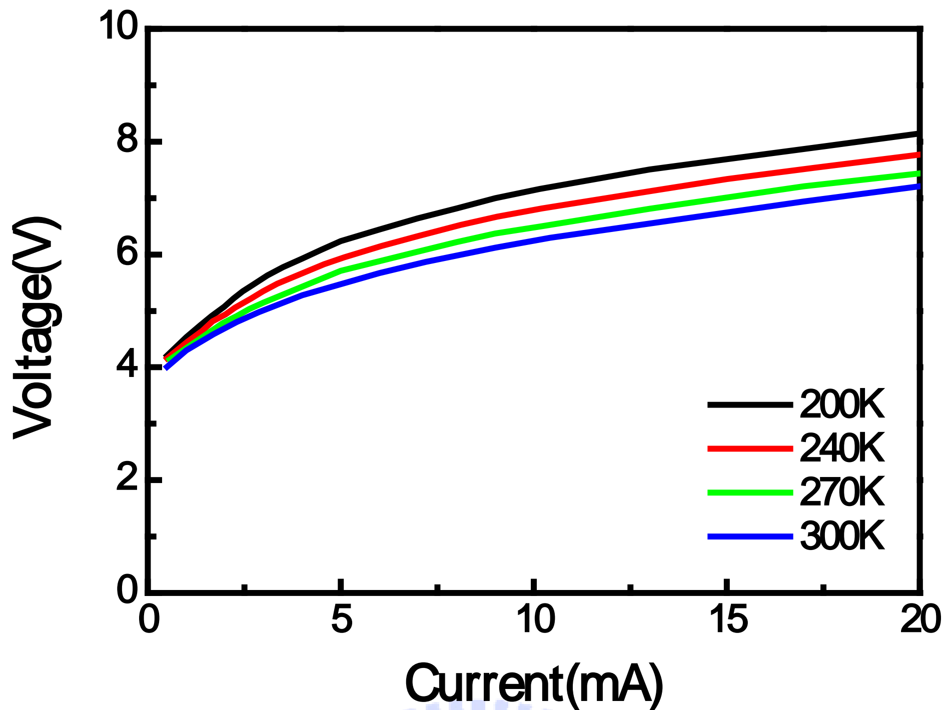

Figure 3. 10 The voltage is a function of injection current at 200 K, 240 K, 270 K, and 300 K.

Figure 3. 11 shows L-I-V curves at 300 K. The dash line is the linear fitting curve of the laser intensity versus injection current. A clear lasing transition from spontaneous emission to stimulated emission can be observed at room temperature. From the linear fitting curve, the laser threshold current is around 9.7 mA corresponding to the current density of about 12.4 kA/cm^2. The relative low threshold at room temperature operation could be due in part to the successful prevention of carrier overflow by using the electron blocking layer on top of the MQWs and the lower internal absorption loss of the thinner ITO layer. The turn-on voltage is about 4.3 V indicating the good electrical contact of the 30 nm ITO transparent layer and the 2 nm-thick InGaN layers. The output laser intensity from the sample increased linearly with current injection beyond the threshold current. However, the laser intensity started to roll over at higher injection current beyond 15 mA due to the thermal effect.

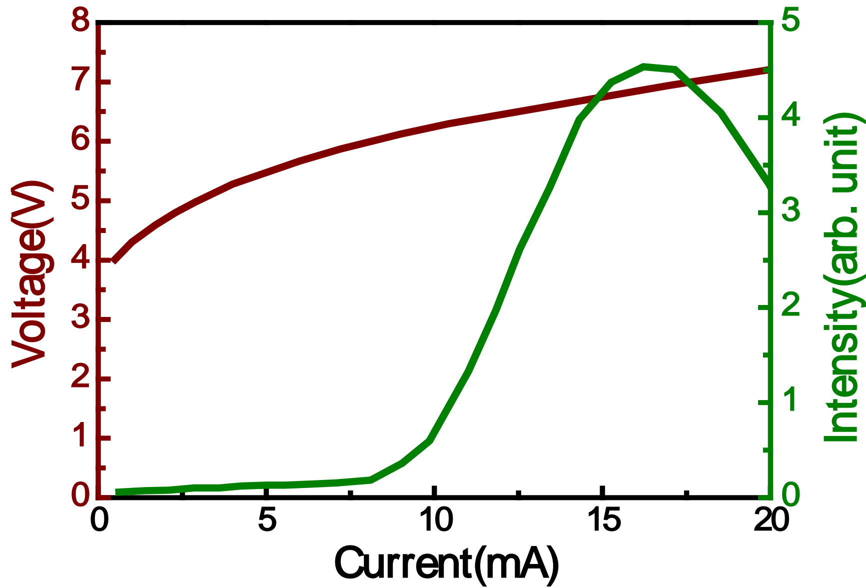

Figure 3. 11 The lasing intensity and the voltage as a function of injection current at 300 K. The threshold current and turn-on voltage are about 9.7 mA and 4.3 V.

Figure 3. 12 shows the variation of emission spectrum with the increasing pumping energy. From the figure, we can observe the transition behavior from spontaneous emission to stimulated emission. Above the threshold current, one dominant laser emission wavelength at 412 nm appears with a linewidth of about 0.5 nm.

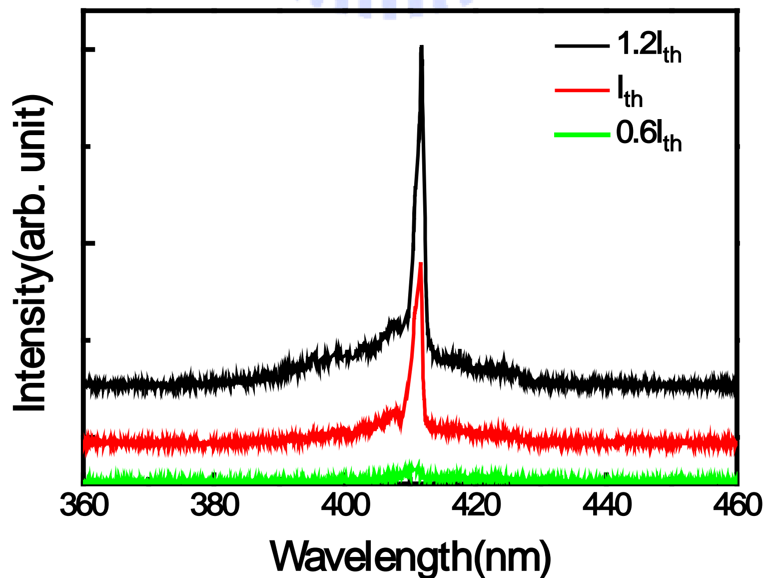

Figure 3. 12 The emission spectra were recorded at injection current of 0.6 I_{th}, 1 I_{th}, and 1.2 I_{th}.

There are two CCD images below and above threshold current as shown in Figure 3. 13, respectively. The blue spontaneous emission could be seen both in these two images. When we injected the current above the threshold current, a laser spot of about 2 μm in diameter with relatively strong intensity appears and shows the inhomogeneous phenomenon of InGaN material.

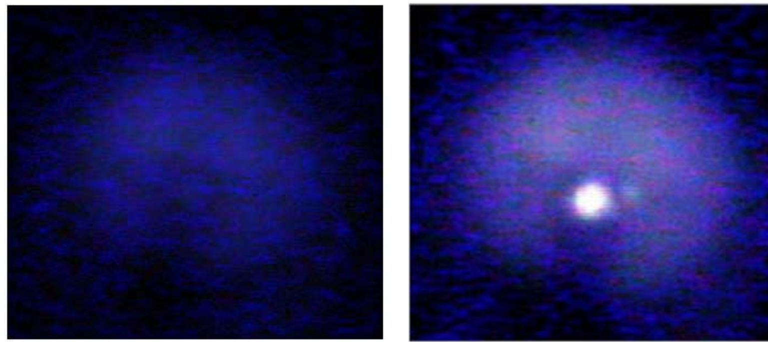

Figure 3. 13 The image shows the lasing spot with the diameter of about 2 μm below and above threshold current.

Characteristic Temperature

Figure 3. 14 shows the semi natural-logarithm plot of the dependence of the threshold pumping energy (lnE_{th}) on the operation temperature (T). The threshold current gradually increased as the operation temperature rose from 200 K to 300 K. In general, we will use the relation between the threshold current and the operation temperature could be characterized by the equation $E_{th}=E_0\times e^{T/T_0}$, where T_0 is the characteristic temperature and E_0 is a constant, showing the linear characteristic between measurement temperature and laser threshold power. However, the relationship between the threshold current and the operation temperature in VCSEL devices appear the U-shape property not linear relation. Therefore, we cannot estimate the characteristic temperature in the laser devices.

This high T_0 could be understood by some temperature-dependent properties of the components in the nitride structure, active region and DBR. The lasing wavelength shows a slight red shift about 1 nm as the temperature rose from 200 K to 300 K as shown in Figure 3. 15. This lasing wavelength shift per Kevin degree is so small of about 10^{-2} nm/K that the gain peak almost keeps aligning the cavity mode. In fact, the reflectivity of nitride-based DBR is also almost independent with the variation of temperature as shown in previous report. That is, the slightly shifted gain

peak actually could keep meeting the highest reflectivity although temperature was varied. Therefore, the superior high temperature performance of the GaN-based VCSEL structure could be attributed to the almost invariant reflectivity spectrum of AlN/GaN DBR, and less shift of the gain peak and cavity mode as the temperature rises, and the ten-pair $In_{0.2}Ga_{0.8}N$/GaN MQW structure which could suppress the carrier leakage from the MQW active layers to the cladding layers and the thick GaN cavity (1.1 μm in thickness) providing a good heat dissipation path during the high carrier injection and high temperature conditions [7].

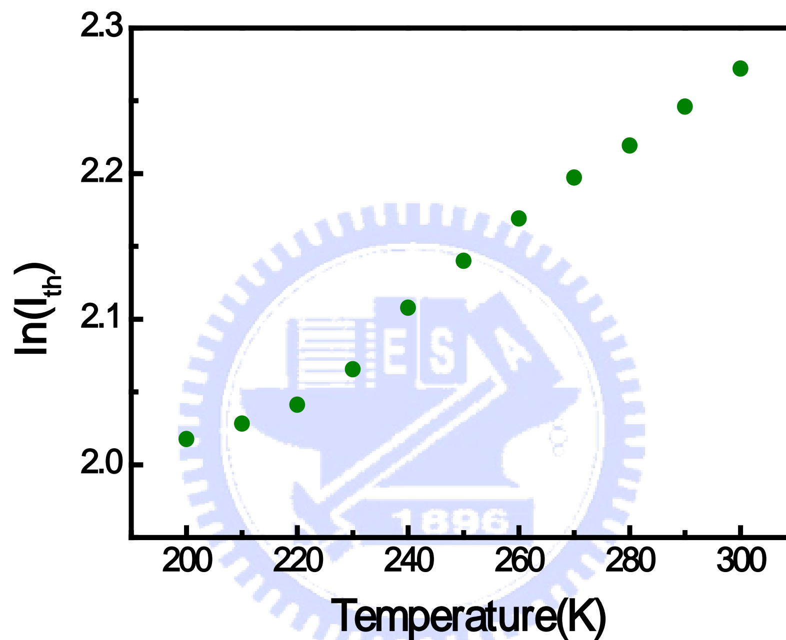

Figure 3. 14 Semi natural-logarithm plot of the dependence of the threshold pumping energy ($ln(I_{th})$) on the operation temperature.

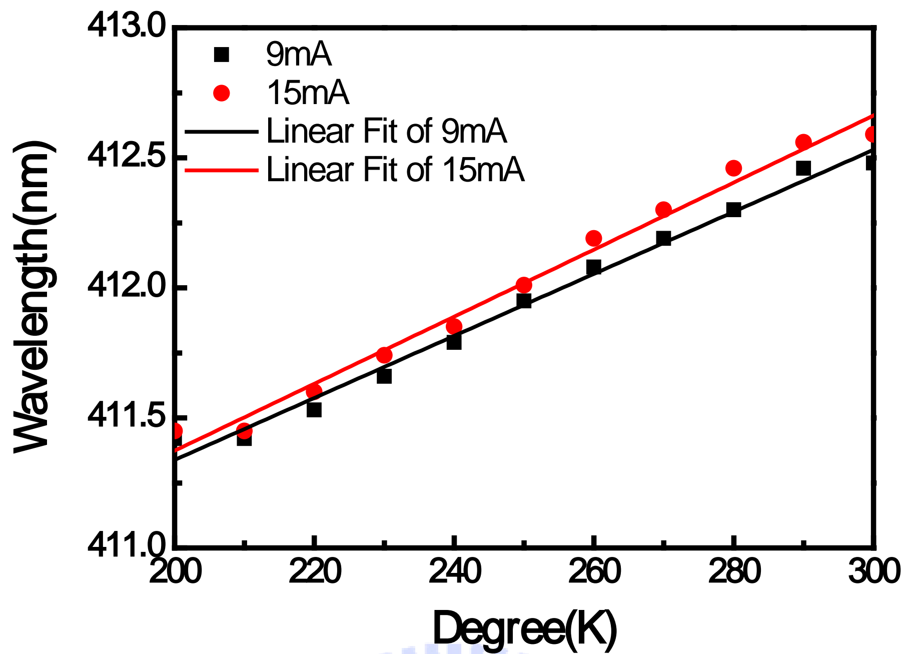

Figure 3. 15 The lasing wavelength of GaN-based VCSEL as a function of temperature at 9 mA and 15 mA.

The coupling efficiency of spontaneous emission (β)

In order to understand the β of this cavity, we normalized the scales of Figure 3. 11 and re-plotted it in a logarithm scale as shown in Figure 3. 16. Besides, we used the Eq. (2. 2 7) to fit our data as shown in chapter 2 and the fitting result shows the β value of the laser is about 5×10^{-3}.

As we mentioned before, this β value of the VCSEL is two order of magnitude higher than that of the typical edge emitting semiconductor lasers (normally about 10^{-5}) [2, 4] indicating the enhancement of the spontaneous emission into a lasing mode by the high quality factor microcavity effect in the VCSEL structure.

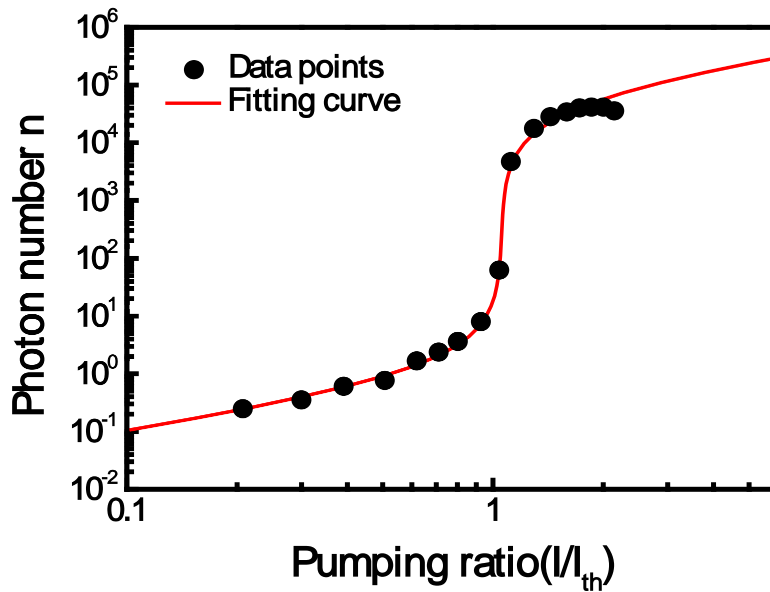

Figure 3. 16 The laser emission intensity versed injection current in logarithmic scale. The solid curve is the fitting curve. The β value is about 5×10^{-3}.

Polarization

The contrast of emission intensity was measured by rotating a polarizer in front of the optical fiber. Figure 3. 17 shows the laser emission intensity as a function of the angle of the polarizer at 0.6 I_{th}. The variation of intensity with the angle of the polarizer shows nearly a sine variation. The degree of polarization (*DOP*) is defined as $DOP = \frac{I_{\max} - I_{\min}}{I_{\max} + I_{\min}}$, where $I_{\max}$ and $I_{\min}$ are the maximum and minimum intensity of the nearly sine variation, respectively. The result showed the laser beam has a degree of polarization of about 54.6 %.

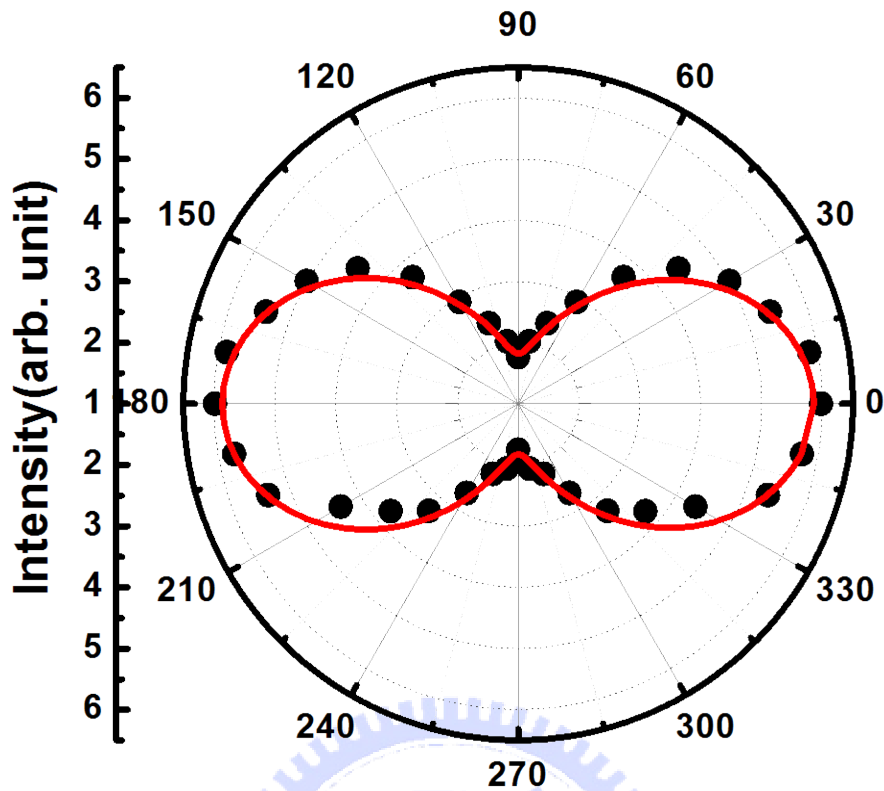

Figure 3. 17 The degree of polarization of VCSEL device is about 55 %. The solid line is the fitting curve.

Far field pattern (FFP)

The far-field patterns (FFP) of the laser were detected by an angular-resolved electrical pumped system and were plotted as shown in Figure 3. 18. It shows the far-field emission intensity as a function of the angle between the light direction and the axial perpendicular to the surface. The divergence angle determined by the FWHM could be estimated from the far-field profile to be as small as about 8 degree.

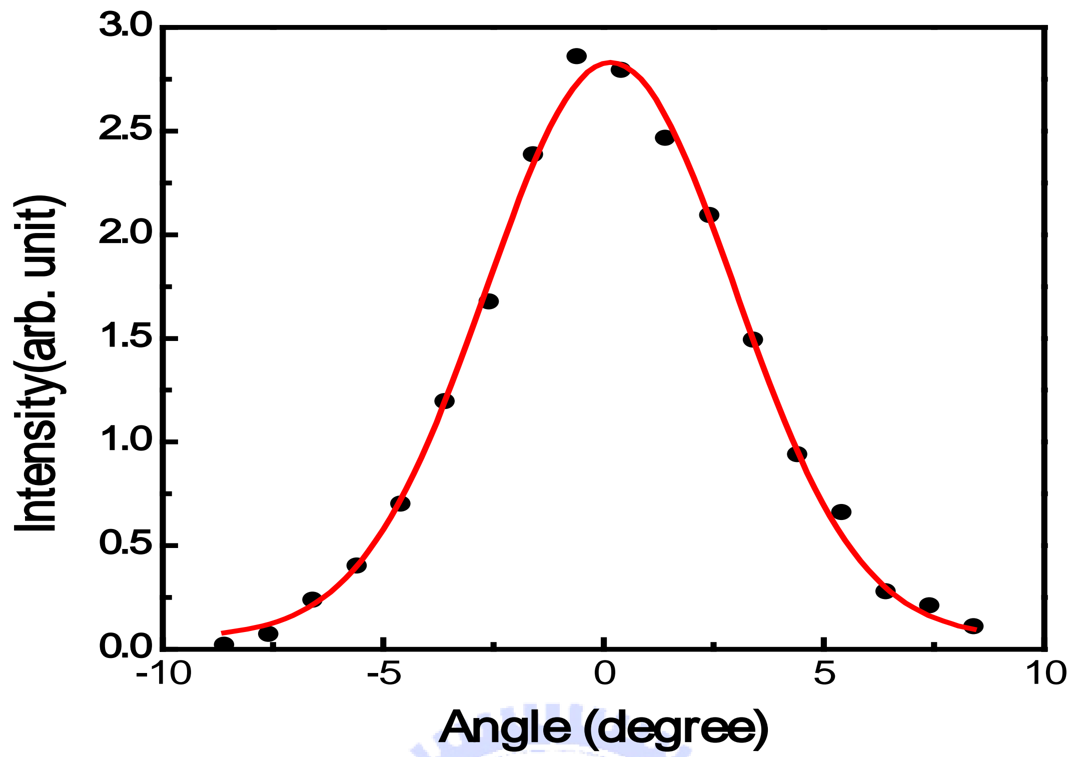

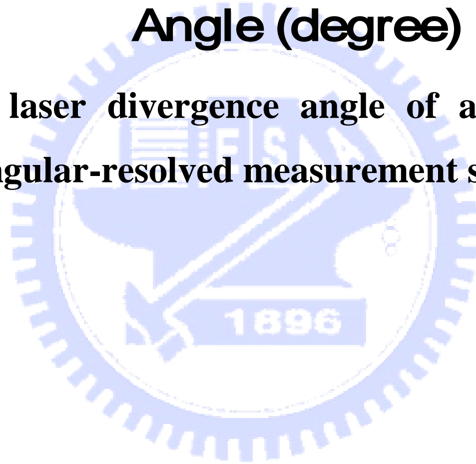

Figure 3. 18 The laser divergence angle of about 8 degree was measured by the angular-resolved measurement system.

References.

[1] G. Yu, G. Wang, H. Ishikawa, and M. Umeno, T. Soga, T. Egawa, J. Watanabe, and T. Jimbo, *Appl. Phys. Lett.*, **70,** 3209 (1997)

[2] T. Someya, R.Werner, A. Forchel, M. Catalano, R. Cingolani and Y.Arakawa, *Science*, **285**, 1905 (1999)

[3] S. H. PARK, *Jpn. J. Appl. Phys.*, **42**, L 170 (2003)

[4] T. Tawara, H. Gotoh, T. Akasaka, N. Kobayashi, and T. Saitoh, *Appl. Phys. Lett.*, **83**, 830 (2003)

[5] Y. Higuchi, K. Omae, H. Matsumura, and T. Mukai, *Appl. Phys. Exp.*, **1**, 121102(2008)

[6] K. Omae, Y. Higuchi, K. Nakagawa, H. Matsumura, and T. Mukai, *Appl. Phys. Exp.*, **2**, 052101 (2009)

[7] M. Ortsiefer, R. Shau, G. Bohm, F. Kohler, J. Rosskopf, and M. C. Amann, *Phys. Stat. Sol.* (a), **188**, 913 (2001)

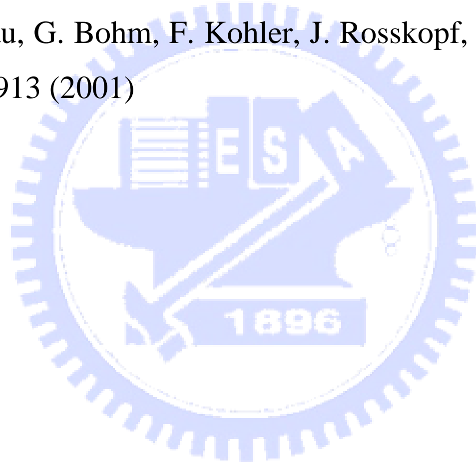

Chapter 4
Design and Fabrication of Photonic Crystal Surface Emitting Lasers

Photonic crystal (PhC) surface emitting lasers utilizing a 2-D distributed feedback (DFB) mechanism has a considerable amount of publication during the past few years [1-4]. The PhC lasers have such excellent advantages to attract the people's attention including controlling the specific lasing modes such as longitudinal and transverse modes, lasing over the large area, and narrow divergence beam. Besides, the calculation of the photonic band-gap and the distribution of electric or magnetic field became more and more important. In the past few years, there were many theoretical calculations and methods have been developed, such as 2-D plane wave expansion method (PWEM) [2, 5], finite difference time domain (FDTD) [6, 7], transfer matrix method, and multiple scattering method, etc. However, there is no any detail lasing characteristic of PhC band-edge modes including the diagram of angular-solved μ-PL system, and the feature of high order lasing modes. In the discussion, we focused on the lasing behavior of PhC band-edge modes lasers in GaN-based 2-D PCSELs with AlN/GaN distributed Bragg reflectors. Each of PhC band-edge modes exhibits a different type of wave coupling mechanism according to the Bragg diffraction mechanism. In this chapter, we introduced the fundamental and higher order Bragg diffraction in section 4.1. According to Bragg diffraction mechanism and coupling wave theory, we can expect the fundamental and high order PhC lasing modes have specific lasing emission characteristics.

4-1 Bragg diffraction theory

First order Bragg diffraction in 2-D triangular lattice PhC [8,9]

Figure 4. 1(a) shows a band diagram of PhC with triangular lattice. The points (A), (B), (C), (D), (E), and (F) present the different lasing modes including Γ1, K2, M1, Γ2, K2, and M2, respectively. Each of the different PhC band-edge lasing modes represents the PhC nanostructure can control the light propagated in different lasing wavelength and band-edge region. Figure 4. 1(b) shows a schematic diagram in a reciprocal space. The reciprocal space of the PhC nanostructure is a space transferred by hexagonal photonic crystal nanostructure in real space. The $K1$ and $K2$ are the Bragg vectors with the same magnitude, $|K|=2\pi/a$, where a is the lattice constant of the photonic crystal. Considered the TE modes in the 2-D photonic crystal nanostructure, the diffracted light

wave from the PhC structure must satisfy the Bragg's law and energy conservation:

$$k_d = k_i + q_1 K_1 + q_2 K_2, \qquad q_{1,2} = 0, \pm 1, \pm 2, \ldots \tag{4. 1}$$

$$\omega_d = \omega_i \tag{4. 2}$$

where k_d is a xy-plane wave vector of diffracted light wave; k_i is a xy-plane wave vector of incident light wave; $q_{1,2}$ is order of coupling; ω_d is the frequency of diffracted light wave, and ω_i is the frequency of incident light wave. Eq. (4. 1) represents the phase-matching condition (or momentum conservation), and Eq. (4. 2) represents the constant-frequency condition (or energy conservation). When both of equations are satisfied, the lasing behavior would be observed.

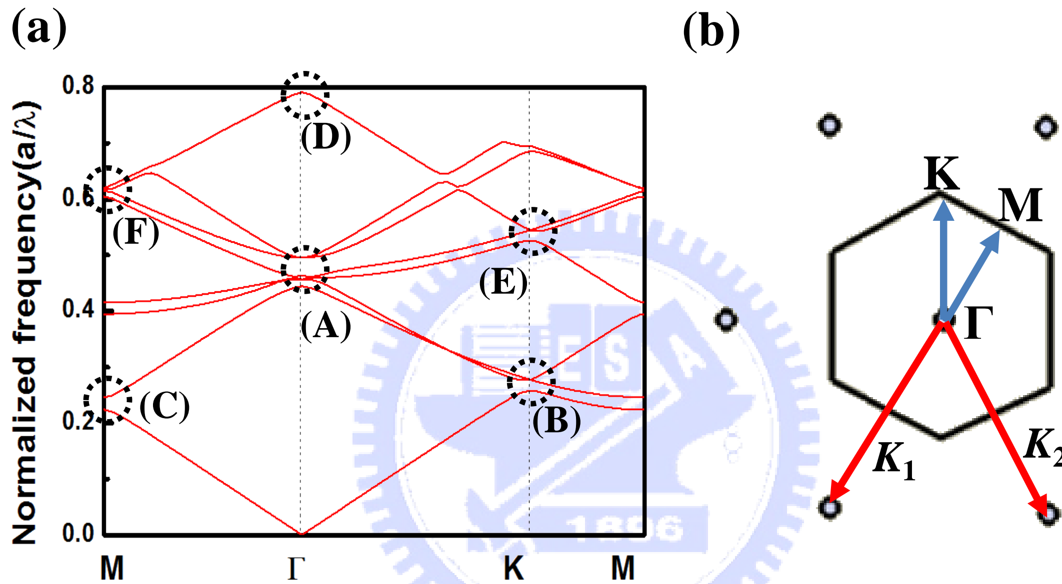

Figure 4. 1 (a) The band diagram of photonic crystal with triangular lattice; (b) The schematic diagram of photonic crystal with triangular lattice in reciprocal space.

Of course, it is expected the lasing behavior would occur at specific points on the Brillouin-zone boundary including Γ, M, and K and these PhC band-edge lasing modes would split and cross. At these PhC lasing band-edge modes, waves propagating in different directions would be coupled and increased the mode density (or density of state, DOS). It is particularly interesting that each of these band-edge modes exhibits a different type of wave coupling routes. For example, as shown in Figure 4. 1(c), the coupling at point (C) only involves two waves, propagating in the forward and backward directions. This coupling is similar to that of a conventional DFB laser. Both of them show the similar coupling mechanism but different lasing behavior according to the different structure. However, there can be six equivalent Γ-M directions in the structure; that is, the

cavity can exist independently in each of the three different directions to form three independent lasers. Point (B) has a unique coupling characteristic which is different resonance mechanism compared with the conventional DFB lasers. The coupling waves propagating in three different directions are shown in Figure 4. 2(b). This figure means that the cavity is a triangular shape. On the other hand, the point (B) can also be six Γ-K directions in the structure. Therefore, two different lasing cavities in different Γ-K directions coexist independently. At point (A) in Figure 4. 2(a), the coupling waves in in-plane are including six directions 0°, 60°, 120°, -60°, -120°, and 180. The coupled light can emit perpendicular from the sample surface according to satisfied first order Bragg diffraction, as shown in Figure 4. 3. Therefore, the PhC devices can function as a surface emitting lasers.

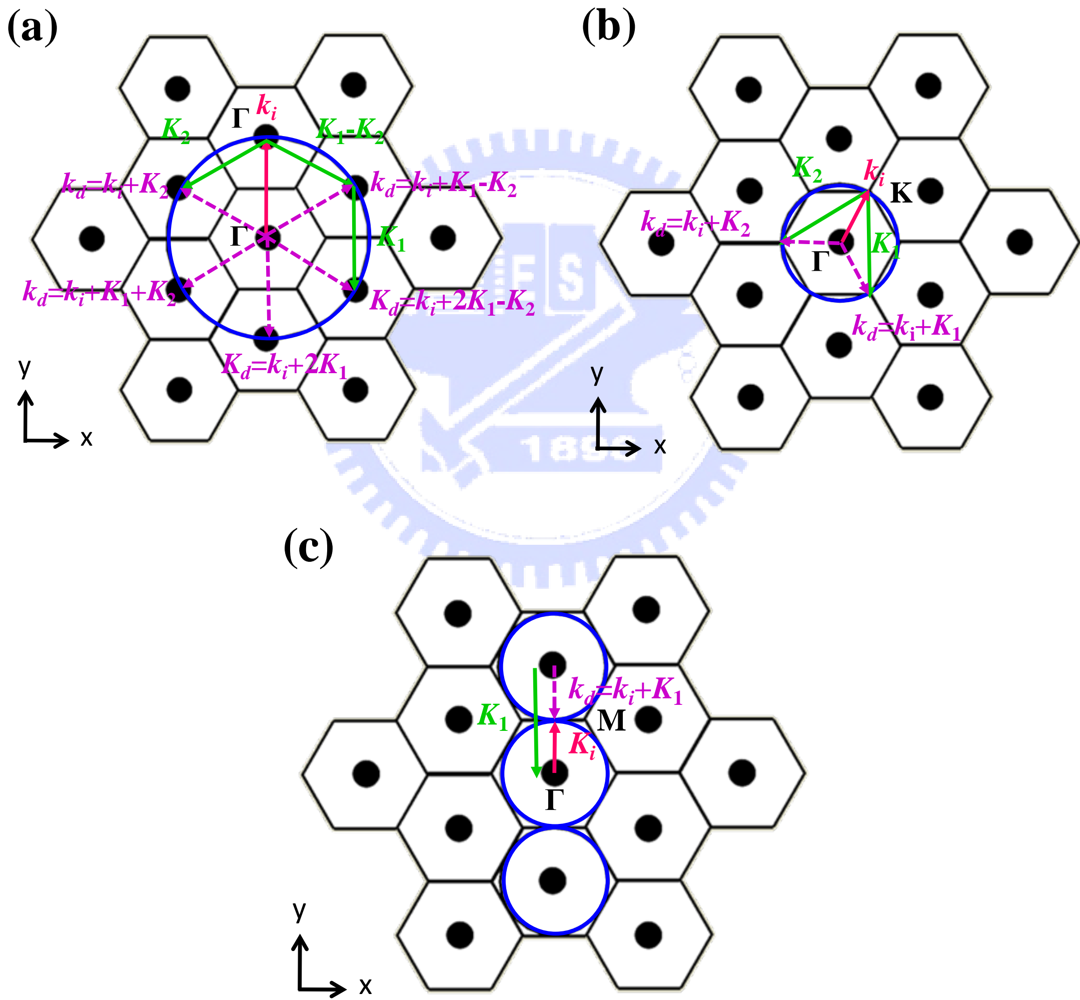

Figure 4. 2 Wave vector diagram at points (A), (B), (C) in Figure 4. 1(a); k_i and k_d indicate the incident and diffracted light wave.

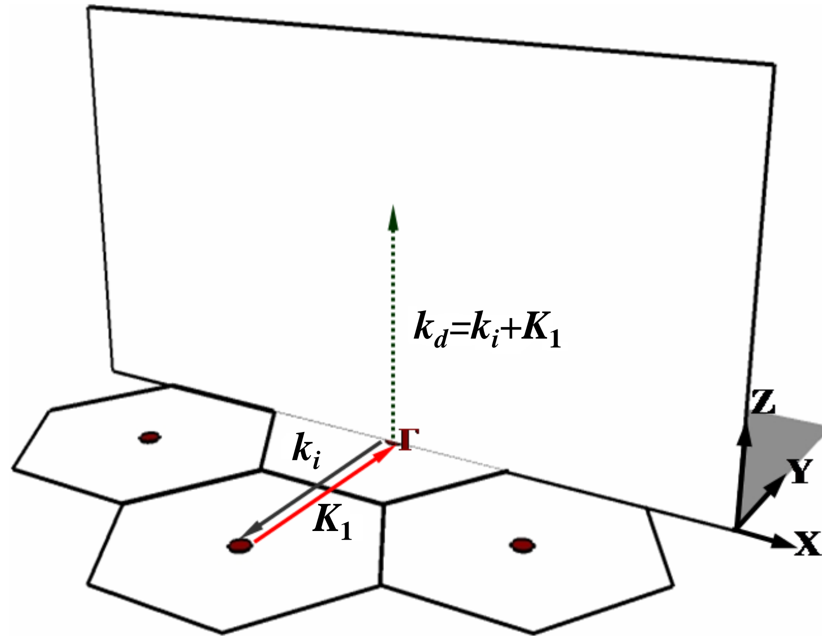

Figure 4. 3 The wave vector diagram at point (A) in vertical direction.

Higher order Bragg diffraction in 2-D PhC with triangular lattice

Figure 4. 4(a) and Figure 4. 4(b) show the in-plane and vertical diffraction at point (D). In this case, the light wave is diffracted in five Γ-K directions and in the vertical direction similar to point (A) and (k_i+q_1K_1+q_2K_2) which can reach to the six Γ' points. Figure 4. 4(c) shows the wave vector diagram of one Γ' point in K space where the light wave is diffracted to an oblique direction. The light wave would be also diffracted to a bottom oblique direction.

Figure 4. 5(a) and (b) show the in-plane and vertical diffraction at point (E). In this case, the light wave is diffracted in three Γ-K directions and (k_i+q_1K_1+q_2K_2) which can reach to the three K' points. Figure 4. 5(b) shows the wave-vector diagram of one K' point where the light wave is diffracted to an angle tilt 30̊ normally from the sample surface. Therefore, we expect the lasing behavior of K2 mode that would emit at this specific angle.

Figure 4. 6(a) and (b) show the in-plane and vertical diffraction at point (F). In this case, the light wave is diffracted in two different Γ-M directions and (k_i+q_1K_1+q_2K_2) which can reach to the three M' points. Figure 4. 6(b) shows the wave-vector diagram of one M' point where the light wave is diffracted into three independent angles tilted of about 19.47̊, 35.26˚, and 61.87˚ normally from the sample surface, respectively. Since we collected PL spectrum on one detected plane, these diffraction angles would be happened on different detected planes. In our experiment, we could only detect one diffraction angle at one time limited by the detector when the PhC effect is occurred.

Figure 4. 4 Wave vector diagram of (a) in-plane and (b) vertical direction at point (D); (c) wave vector diagram showing diffraction to an oblique direction at point (D).

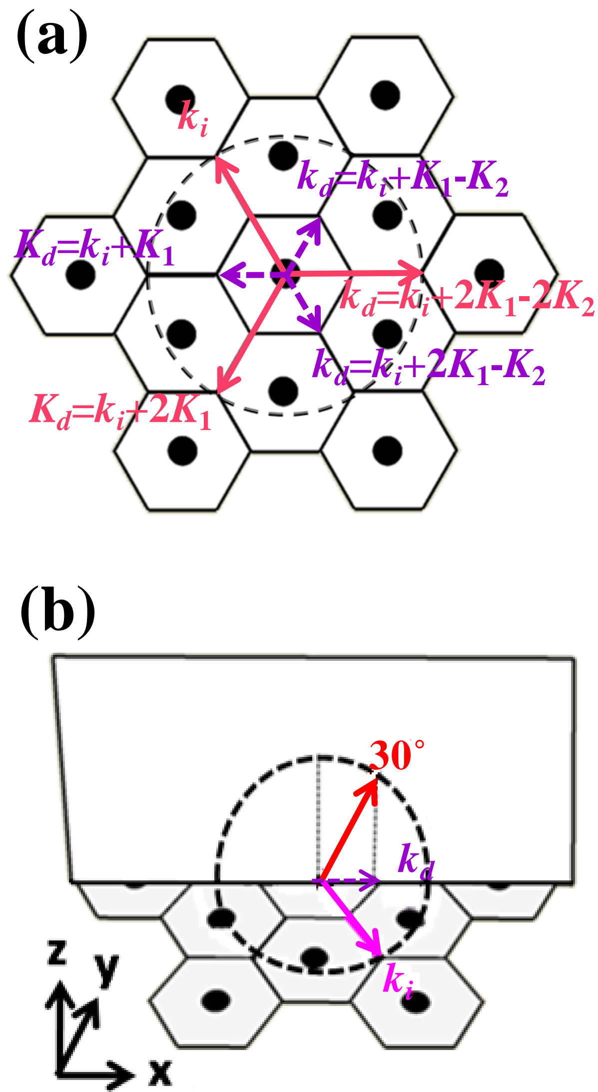

Figure 4. 5 Wave vector diagram of (a) in-plane and (b) vertical direction at point (E) (or K2 mode); k_i and k_d indicate incident and diffracted light wave.

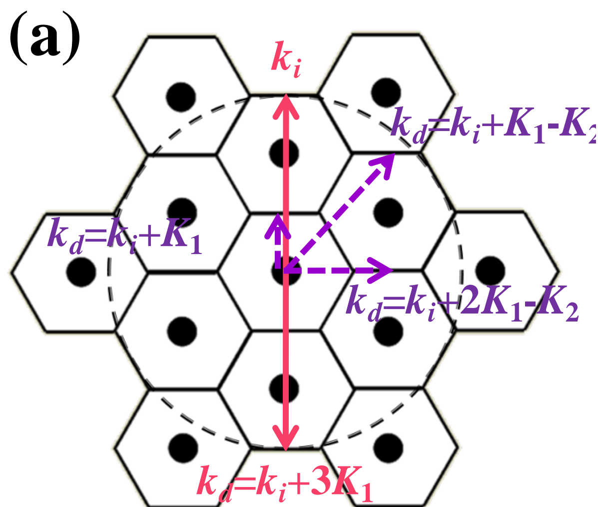

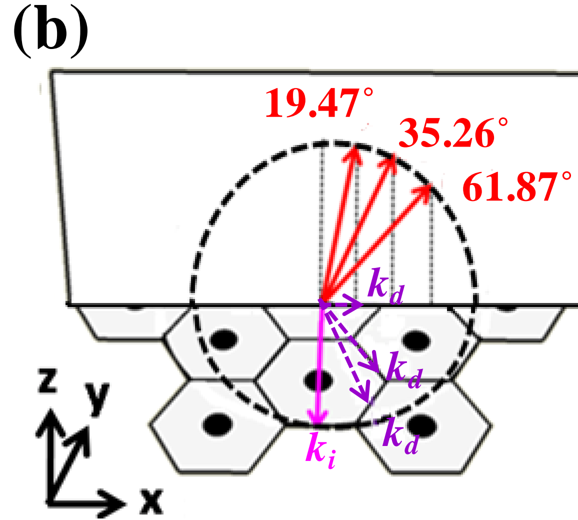

Figure 4. 6 Wave vector diagram of (a) in-plane and (b) vertical direction at point (F) (or M3 mode); k_i and k_d indicate incident and diffracted light wave.

Diffraction pattern of 2-D PhC [10]

In the previous section, we show the Bragg diffraction mechanism causing different PhC lasing resonance routes including Γ mode and high order modes in K space. Furthermore, in this section, we will discuss about the "continuous" Bragg diffraction extraction mechanism causing different diffraction lines in the diagram of angular-resolved μ-PL system. Each direction of emission (or extraction) is associated with a given in-plane wave vector, $k_{//}$, or effective index $n_{eff} = (k_{//})/k_0$, where k_0 is the wave vector of light in vacuum [11]. Therefore, the diagram by angular-resolved μ-PL system can be discussed and classified into four different parts by n_{eff} as shown in Figure 4.7(a). The parts of the spectrum with effective index $n_{eff} < 1$ are extracted directly. These propagate in all directions in air and represent only 10% of the whole radiated power. The parts with $1 < n_{eff} < 1.7$ are delocalized modes. These are produced by evanescent waves emitted by the dipole, and their contribution to the total radiated power is about 40%. The peaks in the dipole power spectrum with $1.7 < n_{eff} < 2.5$ are associated with guided modes and also induced by the dipole emission of evanescent waves. They carry slightly more than 45% of the total emission. The components with $n_{eff} > 2.5$ are purely evanescent and do not contribute in the radiative intensity.

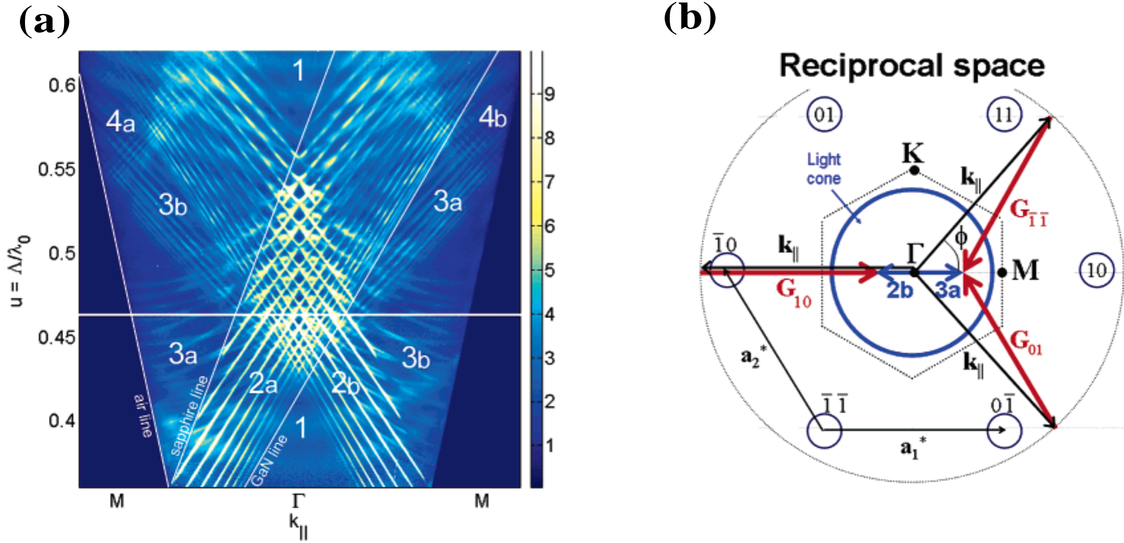

Figure 4. 7 (a)Normalized far-field PL spectrum of the PhC-assisted QD structure; (b) Reciprocal lattice associated with the 2-D PhC and origin of extracted guided modes. The blue and gray circles indicate the light cone and the trace of points with identical $k_{//}$, respectively. The gray hexagon is the first Brillouin zone boundary.

For each reduced frequency, the measurement results covers all possible $k_{//}$ values in the light cone delimited by the air light line and seen clearly in this plot because no light can emit below the light line. Another characteristic line arises from the presence of the cutoff frequency for any given guided mode. This occurs when $k_{//}$ reaches the sapphire line, defined by $k_{//} = 1.7k_0$. For any given frequency, there is a discrete number of guided modes carried by the planar cavity, with $1.7 < n_{eff} <$ 2.5. The lowest order mode has $n_{eff} < 2.5$. This mode almost perfectly follows the GaN line, defined by $k_{//} = 2.5k_0$. The number of guided modes as measured with this sample is in accordance with the simulation photonic band diagram. To explain all of the effects caused by a 2-D PhC particular in the effects related to polarization, the field, associated with a guided modes for example, should be described as a Bloch mode: $E(r) = \Sigma_G E_G * \exp [i (k_{//} + G) \bullet r]$, where E_G is the electric field component corresponding to harmonic G, and $k_{//}$ is the in-plane wave vector of the Bloch mode. With our PhC structure, the reciprocal lattice (RL) in K space is a 2-D triangular lattice rotated by 30° with respect to the direct lattice (DL) in real space and RL vectors can be written as: $G = ha_1^* + ka_2^*$, where h and k are integers, and a_1^* and a_2^* are the two RL basis vectors. Harmonics of the Bloch mode are extracted if their in-plane wave vectors are within the light cone: $|k_{//} + G| < k_0$. The most striking feature observed in Figure 4. 7(a) is the detection of the radiative components of

guided modes. The sets of lines labeled 2a and 2b are induced by the radiative harmonics of the TE-polarized guided modes propagating in the Γ-M direction with in-plane wave vectors $k_{//} + G_{10}$ and $k_{//} + G_{-10}$ (shown in Figure 4. 7(b)), where shown only a radiative harmonic associated with set 2b, for clarity; 2a is obtained by symmetry. The sets of lines labeled 3a and 3b are formed by the combination of two harmonics (as shown in Figure 4. 8 for a line associated with set 3a). These radiative harmonics are not associated with guided modes propagating in the Γ-M direction but in directions about ±60°. The measurement of these components constitutes direct evidence of 2-D PhC-assisted light extraction [12].

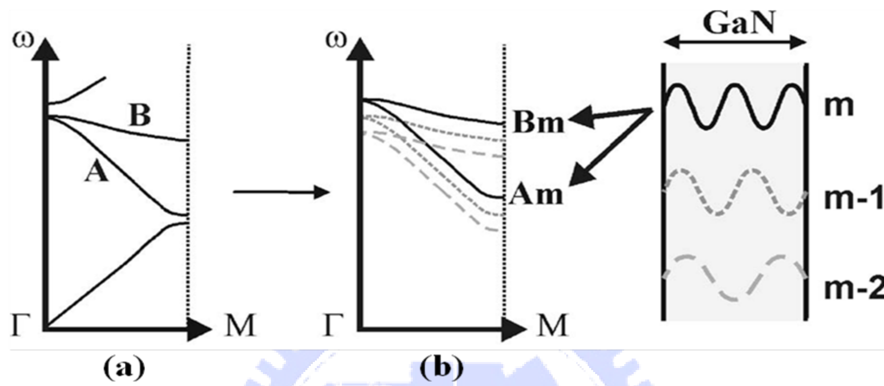

Figure 4. 8 2-D band structure of a PhC in the Γ-M direction; (b) Corresponding band structure in a multimode waveguide: mode *m* gives rise to two PhC bands, Am and Bm.

4-2 Couple wave theory [13,14]

Distributed feedback lasers do not utilize the conventional cavity mirrors, but provide feedback via backward Bragg scattering from periodic perturbations of the refractive index or the gain of the medium. Distributed feedback structures are compact and provide a high degree of spectral selection. In this section, we are focus more on the electromagnetic aspects of light wave propagation, particularly for our photonic structures. We revolve around couple-wave theory to approximately solve the complex equations, which would be addressed numerically.

1-D Couple Wave Theory

In order to use these approaches, we generally know at least that some of eigenmodes of a relatively simple waveguide configuration. The trick is to express the solution to some perturbed or more complex configuration in terms of these original basis set of eigenmodes. Then we can get general form of any dimension couple-wave equation.

To get started, we recall the fundamental wave equation to help us understand it. In a

homogeneous, source-free and lossless medium, any time dependent harmonic electric field satisfy the vector wave equation

$$\nabla^2 \vec{E} + k_0{}^2 n^2 \vec{E} = 0 \tag{4. 3}$$

where the time dependence of the electric field is assumed to be e^{jwt} , n is the refractive index and k_0 is the free space propagation constant. And the electric field must satisfy the homogeneous wave equation such that:

$$\frac{\delta^2}{\delta z^2} E + k^2 E = 0 \tag{4. 4}$$

Consider a multi-dielectric stack in which periodic corrugations are formed along one boundary as illustrated in Figure 4. 9.

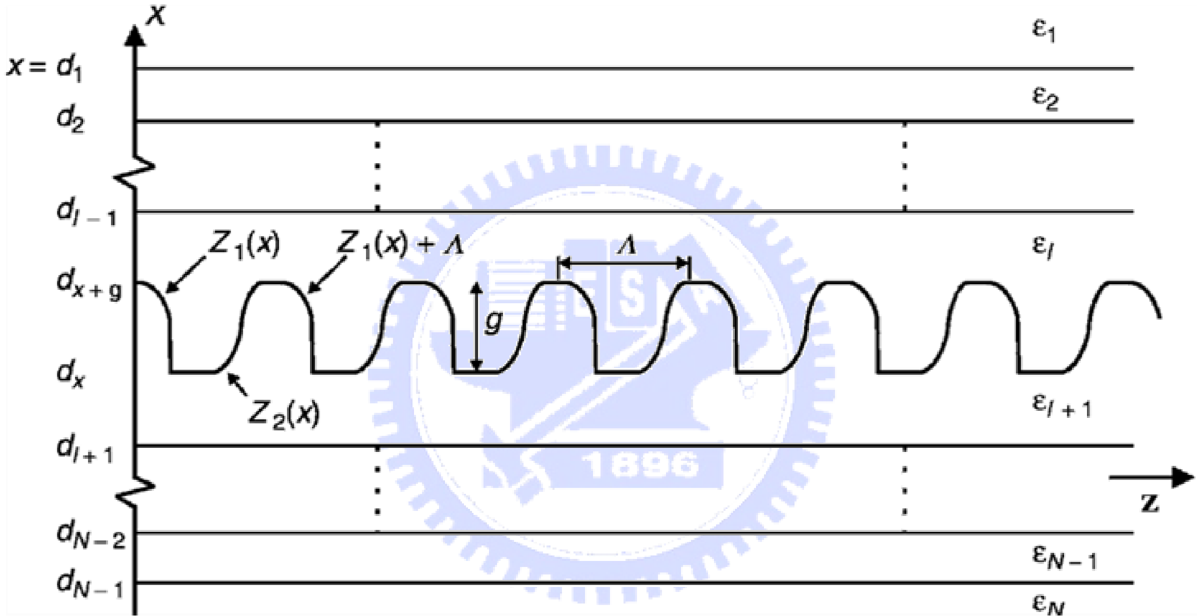

Figure 4. 9 General multi-dielectric layers show the perturbation of refractive index and amplitude gain. $Z_1(x)$ and $Z_2(x)$ are two corrugated functions.

The material complex permittivity in each layer is denoted as ε_j while g and Λ are the height and the period of corrugation, respectively. With corrugations extending along the longitudinal direction, the wave propagation constant, $k(z)$, could be written as

$$k^2(z) = w^2 \mu \varepsilon' \tag{4. 5}$$

where w is the angular frequency and ε' is the complex permittivity. When the radiation frequency is sufficiently close to the resonance frequency, Eq. (4. 5) becomes

$$k^2 = k_0^2 n^2(z)\left(1 + j\frac{2\alpha(z)}{k_0 n(z)}\right) \tag{4. 6}$$

where $n(z)$ and $\alpha(z)$ are the refractive index and the amplitude gain coefficient, respectively. Within the grating region $dx \le x \le dx + g$, perturbation is considered so the refractive index and gain coefficient can be expressed in a Fourier form as

$$n(z) = n_0 + \Delta n \cos(2\beta_0 z + \Omega) \tag{4. 7}$$

and

$$\alpha(z) = \alpha_0 + \Delta\alpha \cos(2\beta_0 z + \Omega + \theta) \tag{4. 8}$$

Here, n_0 and α_0 are the steady-state values of the refractive index and amplitude gain, respectively. Δn and $\Delta\alpha$ are the amplitude perturbation terms, β_0 is the propagation constant and Ω is the non-zero residue phase at the z-axis origin. In the Eq. (4. 8), θ express the relative phase difference between perturbations of the refractive index and amplitude gain. Assume there is an incident plane wave entering the periodic and lossless waveguide at an angle of Φ as shown in Figure 4. 10.

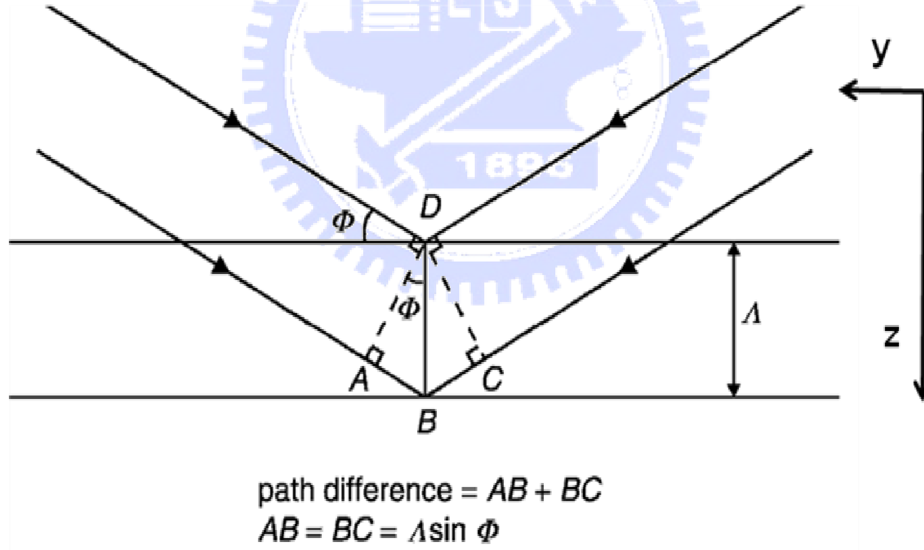

Figure 4. 10 A simple model used to explain Bragg conditions in a periodic waveguide.

At each periodic interval of Λ, the incident wave will experience the same degree of refractive index change so that the incident wave will be reflected in the same direction. For a waveguide that consists of N periodic corrugations, there will be N reflected wavelets. In order that any two reflected wavelets add up in phase or interfere constructively, the phase difference between

the reflected wavelets must be a multiple of 2π. In other words,

$$\beta_0(AB+BC)=\beta_0(2\Lambda\sin\Phi)=2m\pi \tag{4. 9}$$

where m is an integer. If the incident wave is now approaching more or less at a right angle to the wavefront (i.e. $\Phi\approx\pi/2$), Eq. (4. 9) becomes

$$2\beta_0\Lambda=2m\pi \tag{4. 10}$$

This is known as the Bragg condition and β_0 becomes the Bragg propagation constant. The integer m shown in the above equation defines the order of Bragg diffraction. Unless otherwise stated, first-order Bragg resonance (m =1) is assumed. Since a laser forms a resonant cavity, the Bragg condition must be satisfied [13]. Rearranging Eq. (4. 10) gives

$$\beta_0\equiv\frac{2\pi n_0}{\lambda_B}\equiv\frac{n_0 w_B}{c}=\frac{\pi}{\Lambda} \tag{4. 11}$$

where λ_B and w_B are the Bragg wavelength and the Bragg frequency, respectively. From Eq. (4. 11), it is clear that the Bragg propagation constant is related to the grating period. By altering the grating period, the Bragg wavelength can be shifted according to the specific application.

Using small signal analysis, the perturbations of the refractive index and gain are always smaller than their average values, i.e.

$$\Delta n<<n_0,\quad \Delta\alpha<<\alpha_0 \tag{4. 12}$$

Substituting Eq. (4. 7) and Eq. (4. 8) into Eq. (4.6) using the above assumption, generates

$$k^2(z)=k_0{}^2 n_0{}^2+j2k_0n_0\alpha_0+2k_0[k_0n_0+j\alpha_0]\Delta n\cos(2\beta_0 z+\Omega)$$
$$+2jk_0n_0\Delta\alpha\cos(2\beta_0 z+\Omega+\theta) \tag{4. 13}$$

With k_0n_0 replaced by β and $\alpha_0<\beta$, the above equation becomes

$$k^2(z)\approx\beta^2+2j\beta\alpha_0+2\beta[\frac{\pi\Delta n}{\lambda}+j\frac{\Delta\alpha}{2}e^{j\theta}]e^{j(2\beta 0z+\Omega)}$$
$$+2\beta[\frac{\pi\Delta n}{\lambda}+j\frac{\Delta\alpha}{2}e^{-j\theta}]e^{-j(2\beta 0z+\Omega)} \tag{4. 14}$$

For the case when $\theta=0$, one can simplify Eq. (4. 13) to[15]

$$k^2\approx\beta^2+2j\beta\alpha_0+4\beta\left[\frac{\pi\Delta n}{\lambda}+j\frac{\Delta\alpha}{2}\right]\cos(2\beta_0 z+\Omega) \tag{4. 15}$$

By controlling all the perturbed terms, one can define a parameter k[13,15] such that

$$k=\frac{\pi\Delta n}{\lambda}+j\frac{\Delta\alpha}{2}=k_i+jk_g \tag{2.13}$$

Here k_i includes all contributions from the refractive index perturbation whilst k_g covers all contributions from the gain perturbation. The parameter k introduced in the above equation is

known as the coupling coefficient. After a series of simplifications, Eq.(4. 15) becomes

$$k^2 \approx \beta^2 + 2j\beta\alpha_0 + 4k\beta\cos(2\beta_0 z + \Omega) \tag{4. 16}$$

On substituting the above equation back into the wave equation, one ends up with

$$\frac{d^2E}{dz^2} + \{\beta^2 + 2j\beta\alpha_0 + 2k\beta e^{j(2\beta 0z+\Omega)} + 2k\beta e^{-j(2\beta 0z+\Omega)}\}E = 0 \tag{4. 17}$$

where the cosine function shown in Eq. (4. 16) has been expressed in phase form. A trial solution of the scalar wave equation could be a linear superposition of two opposing traveling waves such that

$$E(z) = A(z)e^{-jkunz} + B(z)e^{jkunz} \tag{4. 18}$$

with

$$k^2{}_{un} = \beta^2 + 2j\beta\alpha_0 \approx (\beta + j\alpha_0)^2 \quad (\because \alpha_0 << \beta) \tag{4. 19}$$

In order to satisfy the Bragg condition shown earlier in Eq. (4. 11), the actual propagation constant, β, should be sufficiently close to the Bragg propagation constant, β_0, to make the absolute difference between them much smaller than the Bragg propagation constant. In other words,

$$|\beta - \beta_0| << \beta_0 \tag{4. 20}$$

Such a difference between the two propagation constants is commonly known as the detuning factor or detuning coefficient, δ, which is defined as

$$\delta = \beta - \beta_0 \tag{4. 21}$$

The trial solution can be expressed in terms of the Bragg propagation constant, i.e.

$$E(z) = C(z)e^{-\delta z}e^{-j\beta 0z} + D(z)e^{\delta z}e^{j\beta 0z} = R(z)e^{-j\beta 0z} + S(z)e^{j\beta 0z} \tag{4. 22}$$

where $R(z)$ and $S(z)$ are complex amplitude terms. Since the grating period Λ in a DFB semiconductor laser is usually fixed and so is the Bragg propagation constant, it is more convenient to consider Eq. (4. 22) as the trial solution of the scalar wave equation. By substituting Eq. (4. 22) into Eq .(4. 17), one ends up with the following equation

$$\begin{aligned}&(R''-2j\beta_0R'-\beta_0{}^2R+\beta^2R+2j\beta\alpha_0R)e^{-j\beta 0z}\\&+(S''+2j\beta_0S'-\beta_0{}^2S+\beta^2S+2j\beta\alpha_0S)e^{j\beta 0z}\\&+2k\beta(e^{2j\beta 0z}e^{j\Omega}+e^{-2j\beta 0z}e^{-j\Omega})\cdot(\mathrm{R}e^{-j\beta 0z}+Se^{j\beta 0z})=0\end{aligned} \tag{4. 23}$$

where R' and R" are the first- and second-order derivatives of R. Similarly, S' and S" represent the first- and second-order derivatives of S. With a 'slow' amplitude approximation, high-order derivatives like R" and S" become negligible when compared with their first-order terms. By separating the above equation into two groups, each having similar exponential dependence, one

can get the following pair of coupled wave equations

$$-\frac{dR}{dz}+(\alpha_0-j\delta)R=jkSe^{-j\Omega} \tag{4. 24}$$

$$\frac{dS}{dz}+(\alpha_0-j\delta)S=jk\,\mathrm{Re}^{j\Omega} \tag{4. 25}$$

Eq. (4. 24) collects all the $exp(-j\beta_0 z)$ phase terms propagating along the positive z direction, whilst Eq. (4. 25) gathers all the $exp(j\beta_0 z)$ phase terms propagating along the negative direction. Since $|\delta|<<\beta$, other rapidly changing phase terms such as $exp(\pm j3\beta_0 z)$ have been dropped. In deriving the above equations, the following approximation has been assumed

$$\frac{\beta^2-\beta_0{}^2}{2\beta_0}\approx\beta-\beta_0=\delta \tag{4. 26}$$

Following the above procedures, one ends up with a similar pair of coupled wave equations for a non-zero relative phase difference between the refractive index and the gain perturbation (i.e. $\theta\neq 0$) such that

$$-\frac{dR}{dz}+(\alpha_0-j\delta)R=jk_{RS}\,\mathrm{Re}^{-j\Omega} \tag{4. 27}$$

$$\frac{dS}{dz}+(\alpha_0-j\delta)S=jk_{SR}\,\mathrm{Re}^{j\Omega} \tag{4. 28}$$

where

$$k_{RS}=k_i+jk_g e^{-j\theta} \tag{4. 29}$$

is the general form known as the forward coupling coefficient and

$$k_{SR}=k_i+jk_g e^{j\theta} \tag{4. 30}$$

is the backward coupling coefficient.

It is contrary to Fabry-Perot lasers, where optical feedback is come from the laser facets. Optical feedback in DFB lasers is originated from along the active layer where corrugations are fabricated. From the above scalar equation, the couple-wave equation can be established in the general form, which is for one dimensional situation. Following we will discuss two dimensional optical coupling based on above couple- wave theory. For our GaN-based photonic structure, we assume that since the carriers in the InGaN layers are confined in the wall, they do posses a significant in-plane dipole, which can couple to TE mode. Therefore, we centered on TE like mode in square lattice for 2-D case.

2-D couple-wave model

Preliminary numerical works have been done by Sakai, Miyai, and Noda [16,17]. Here, we cite their papers as references to help us understand the 2-D couple-wave model. The 2-D PC structure investigated here consists of an infinite square lattice with circular air holes in the *x* and *y* directions, as shown in Figure 4. 11. The structure is assumed to be uniform in the z direction. We don't consider the gain effects during calculation. We do calculate the resonant mode frequency as a function of coupling coefficient. The scalar wave equation for the magnetic field *Hz* in the TE mode can be written as [18]

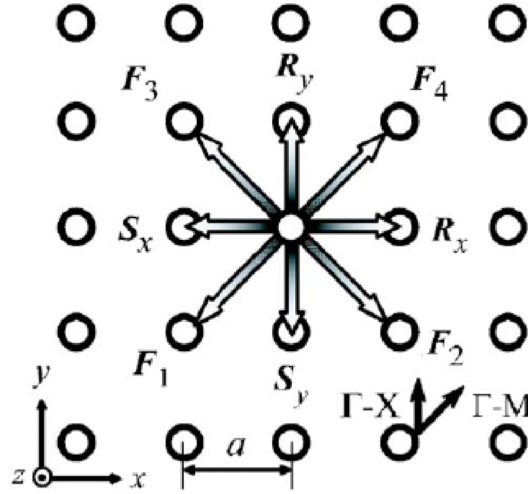

Figure 4. 11 Schematic diagram of eight propagation waves in square lattice PC structure.

$$\frac{\partial^2 Hz}{\partial x^2}+\frac{\partial^2 Hz}{\partial y^2}+k^2 Hz=0 \tag{4. 31}$$

where [19]

$$k^2=\beta^2+2j\alpha\beta+2\beta\sum_{G\neq 0}k(G)\exp[j(G\cdot r)] \tag{4. 32}$$

G=($m\beta_0$, $n\beta_0$) is the reciprocal lattice vector, m and n are arbitrary integers, $\beta_0=2\pi/a$ where a is the lattice constant, $\beta=n_{av}w/c$ where n_{av} is the averaged refractive index, $k(G)=\pi n_G/\lambda$ is the coupling constant, where n_G is the Fourier coefficient of the periodic refractive-index modulation and λ is the Bragg wavelength given by $\lambda=an_{av}$. In the Eq. (4. 32), we set $\alpha,\alpha_G<<\beta_0$, $n_G<<n_0$. We do consider Γ point, in which when it is satisfy the second order Bragg diffraction, it will induce 2-D optical coupling and result in surface emission. The coupling constant $\kappa(G)$ can be expressed as

$$\kappa(G) = \frac{\pi}{\lambda} n(G) + j\frac{1}{2}\alpha(G) \quad (4.\ 33)$$

where $n(G)$ is the Fourier coefficient of periodic refractive index modulation and λ is the Bragg wavelength given by $\lambda = an_{av}$.

In Eq. (4. 32), the periodic variation in the refractive index is included the small perturbation in third term through the Fourier expansion. In the Fourier expansion, the periodic perturbation terms generates an infinite set of diffraction orders. However, as the cavity mode frequency is sufficient close to the Bragg frequency, only the second order diffraction and below can do significant contribution, others can consider to be neglected. Therefore, we focus on diffraction order with $|m| + |n| \le 2$ to discuss. The corresponding coupling coefficient constant κ_j (j=1, 2, 3) are denoted as

$$\kappa_1 = \kappa(G) \| G | = \beta_0$$
$$\kappa_2 = \kappa(G) \| G | = \sqrt{2}\beta_0 \quad (4.\ 34)$$
$$\kappa_3 = \kappa(G) \| G | = 2\beta_0$$

while considering infinite structure, the magnetic field can be described by the Bloch mode [18],

$$Hz(r) = \sum_G h_G \exp[j(k + G) \cdot r] \quad (4.\ 35)$$

h_G is the amplitude of each plane wave, k is the wave vector in the first Brillouin zone and when it is the Γ point, it comes to zero. However, in the case of finite structure, h_G is not a constant but a function of vector space. For 2-D case, there are eight propagating waves in PC structure denoted as Rx, Sx, Ry, Sy, F_1, F_2, F_3, F_4 showed in Figure 4. 11, those are the amplitudes of four propagating waves in the x, $-x$, y, $-y$ directions and four propagating waves in Γ-M direction, respectively. Those correspond to h_G in Eq. (4. 35). Here, we do consider these basic wave vectors along the Γ-X directions with $|\kappa + G| = \beta_0$ and Γ-M directions with $|\kappa + G| = \sqrt{2}\beta_0$. The contribution of the higher order waves with $|\kappa + G| \ge 2\beta_0$ are considered to be negligible. We should note that the basic waves and higher order waves are partial waves of the Bloch mode, so they have the same eigenvalue β for specific resonant cavity mode.

The magnetic field in this case can be rewritten as

$$Hz = Rx(x,y)e^{-j\beta 0x} + Sx(x,y)e^{j\beta 0x} + Ry(x,y)e^{-j\beta 0y} + Sy(x,y)e^{j\beta 0y}$$
$$+ F_1 e^{j\beta 0x + j\beta 0y} + F_2 e^{-j\beta 0x + j\beta 0y} + F_3 e^{j\beta 0x - j\beta 0y} + F_4 e^{-j\beta 0x - j\beta 0y} \quad (4.\ 36)$$

Put Eq. (4. 36) and Eq. (4. 32) into the wave Eq. (4. 31), and comparing the equal exponential

terms, we obtain eight wave equations:

$$(\beta-\beta_0)Rx+\kappa_3 Sx-\kappa_1(F_2+F_4)=0 \tag{4. 37a}$$

$$(\beta-\beta_0)Sx+\kappa_3 Rx-\kappa_1(F_1+F_3)=0 \tag{4. 37b}$$

$$(\beta-\beta_0)Ry+\kappa_3 Sy-\kappa_1(F_3+F_4)=0 \tag{4. 37c}$$

$$(\beta-\beta_0)Sy+\kappa_3 Ry-\kappa_1(F_1+F_2)=0 \tag{4. 37d}$$

$$(\beta-2\beta_0)\frac{F_1}{2}-\kappa_1(Sx+Sy)=0 \tag{4. 37e}$$

$$(\beta-2\beta_0)\frac{F_2}{2}-\kappa_1(Rx+Sy)=0 \tag{4. 37f}$$

$$(\beta-2\beta_0)\frac{F_3}{2}-\kappa_1(Sx+Ry)=0 \tag{4. 37g}$$

$$(\beta-2\beta_0)\frac{F_4}{2}-\kappa_1(Rx+Ry)=0 \tag{4. 37h}$$

In the above equations, we assume $\beta/\beta_0\approx 1$, since we take optical coupling at Γ point as an example.

These derivations illustrate the coupling among the propagating waves in square lattice PC structure. We take Eq. (4. 37) for example. It describes the net wave superposition along the x-axis, including the coupling of two waves propagating at opposite directions, *Rx* and *Sx*, with a coupling coefficient κ_3. And the coupling of higher order waves F_2 and F_4, with a coupling coefficient κ_1. The coupling κ_3 provides the main distributed feedback. From above derivations, we know that the orthogonal couplings occur via intermediate coupling of the basic and higher order waves. One thing we should noted that the coupling coefficient κ_2 does not exist in Eq. (4. 37). In the numerical view which describes the basic waves directly couple to orthogonal directions. This physically can be explained in this way: ways of TE modes have their electric field parallel to the PC plane, so that the electric field directions of the two waves propagating in the perpendicular directions are orthogonal to one another, hence the overlap integral of the two waves vanishes.

By using 2-D plane wave expansion method, the band dispersion curves for TE like modes in Figure 4. 12 can be obtained. The condition is limited at the vicinity near Bragg frequency.

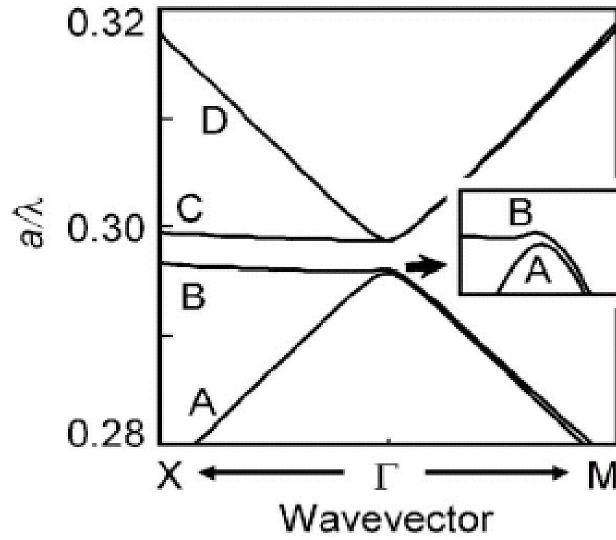

Figure 4. 12 Dispersion relationship for TE like modes, calculated using the 2-D PWEM

By solving Eq. (4. 37), the cavity mode frequency can be obtained. There are three cavity mode frequencies denoted as w_A, w_B, w_C, and w_D with one degenerated.

$$w_A = \frac{c}{n_{av}}(\beta_0 - \kappa_3)\left(1 - \frac{8\kappa_1^2}{\beta_0^2 - \kappa_3^2}\right)$$

$$w_B = \frac{c}{n_{av}}(\beta_0 - \kappa_3) \tag{4. 38}$$

$$w_{C,D} = \frac{c}{n_{av}}(\beta_0 + \kappa_3)\left(1 - \frac{4\kappa_1^2}{\beta_0^2 - \kappa_3^2}\right)$$

The frequencies w_A and w_B at the lower band-edges are non-degenerated, while two of the frequencies w_c and w_D at higher band-edge are degenerated. In the physical meaning, the resonant mode symmetries are different. The resonant mode at band-edge C and D are symmetric, which allows this mode to couple to external field more easily. The characteristics of these resonant modes are essentially leaky [20]. The resonant mode at band-edge A and B are anti-symmetric, resulting in less coupling to the external field. Therefore, the quality factor for band-edge A and B are higher than C and D. It is expected that the lasing behavior is occurred at either A or B. However, band B is flat around Γ point in the Γ-X direction. Light at band-edge B can couple to leaky mode with a wave vector slightly shifted from Γ point, resulting in coupling to the external field. Thus, band-edge B becomes leaky.

According to previous descriptions, we have understood the fundamental couple-wave theory and how to calculate their cavity mode frequency. For our GaN-based PCSELs, we design the

triangular lattice with TE-like mode to tell the differences between square lattice structures. Therefore, in next section, we develop a new model to explain the DFB feedback mechanism based on couple-wave theory. According to our measurement, we found that the lasing action occurred at Γ1, K2, M3 point band-edges. We tried to solve the wave equations at these band-edges and derive the coupling coefficients. All of the detail information will be described numerically in next section.

Couple-wave model for triangular lattice PCSELs

Light at the photonic band-edge has zero group velocity and forms a standing wave due to 2-D DFB effect. Laser oscillation is expected to occur at any band-edge, if the gain threshold is achieved. Therefore, we focus on the coupling waves at Γ1, K2, M3 band-edges according to our lasing behaviors.

I. Γ1 numerical results

The 2-D PC structure investigated here consists of an infinite triangular lattice with circular air holes in the x and y directions, as shown in Figure 4. 13. The structure is assumed to be uniform in the z direction. We don't consider the gain effects during calculation. While considering infinite structure, the magnetic field can be described by the Bloch mode [18],

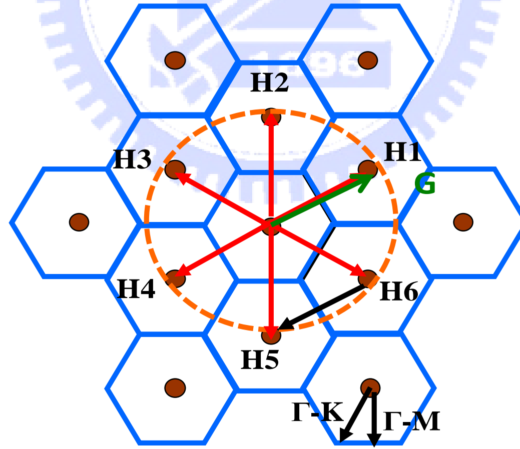

Figure 4. 13 Schematic diagram of six propagation waves in triangular lattice for Γ1 point.

$$Hz(r)=\sum_{G} h_G \exp\left[j(k+G)\cdot r\right] \tag{4. 35}$$

where

$$Hz = H_1 e^{-i\beta 0\hat{x}} + H_2 e^{-i\beta 0(\frac{1}{2}\hat{x}\mp\frac{\sqrt{3}}{2}y)} + H_3 e^{-i\beta 0(\frac{-1}{2}x+\frac{\sqrt{3}}{2}y)}$$

$$+H_4 e^{i\beta 0\hat{x}} + H_5 e^{-i\beta 0(\frac{-1}{2}\hat{x}-\frac{\sqrt{3}}{2}\hat{y})} + H_6 e^{-i\beta 0(\frac{1}{2}\hat{x}-\frac{\sqrt{3}}{2}\hat{y})} \quad (4.\ 39)$$

put Eq. (4. 39) and Eq. (4. 32) into the wave Eq. (4. 31), and comparing the equal exponential terms, we obtain six wave equations

$$-\frac{\partial}{\partial x}H_1 + (-\alpha - i\delta)H_1 = -i\frac{\kappa_1}{2}(H_2 + H_6) + i\frac{\kappa_2}{2}(H_3 + H_5) + i\kappa_3 H_4 \quad (4.\ 40a)$$

$$-\frac{1}{2}\frac{\partial}{\partial x}H_2 - \frac{\sqrt{3}}{2}\frac{\partial}{\partial y}H_2 + (-\alpha - i\delta)H_2 = -i\frac{\kappa_1}{2}(H_1 + H_3) + i\frac{\kappa_2}{2}(H_4 + H_6) + i\kappa_3 H_5 \quad (4.\ 40b)$$

$$-\frac{1}{2}\frac{\partial}{\partial x}H_3 - \frac{\sqrt{3}}{2}\frac{\partial}{\partial y}H_3 + (-\alpha - i\delta)H_3 = -i\frac{\kappa_1}{2}(H_2 + H_4) + i\frac{\kappa_2}{2}(H_1 + H_5) + i\kappa_3 H_6 \quad (4.\ 40c)$$

$$\frac{\partial}{\partial x}H_4 + (-\alpha - i\delta)H_4 = -i\frac{\kappa_1}{2}(H_3 + H_5) + i\frac{\kappa_2}{2}(H_2 + H_6) + i\kappa_3 H_1 \quad (4.\ 40d)$$

$$\frac{1}{2}\frac{\partial}{\partial x}H_5 + \frac{\sqrt{3}}{2}\frac{\partial}{\partial y}H_5 + (-\alpha - i\delta)H_5 = -i\frac{\kappa_1}{2}(H_4 + H_6) + i\frac{\kappa_2}{2}(H_1 + H_3) + i\kappa_3 H_2 \quad (4.\ 40e)$$

$$-\frac{1}{2}\frac{\partial}{\partial x}H_6 + \frac{\sqrt{3}}{2}\frac{\partial}{\partial y}H_6 + (-\alpha - i\delta)H_6 = -i\frac{\kappa_1}{2}(H_1 + H_5) + i\frac{\kappa_2}{2}(H_2 + H_4) + i\kappa_3 H_3 \quad (4.\ 40e)$$

where, H_1, H_2, H_3, H_4, H_5, and H_6 express the envelope magnetic field distributions of individual light waves propagating in the six equivalent Γ-M directions: 0°, +60°, +120°,+180°, +240°, and +300° with respect to the x-axis. κ_1, κ_2, and κ_3 are the coupling coefficients between light waves propagating at 60° to each other (H_1 and H_2, H_2 and H_3, and so on), at 120° (H_1 and H_3, H_2 and H_4, and so on), and at 180° (H_1 and H_4, H_2 and H_5, and so on), respectively. δ is the deviation of the wave number β (expressed as $2\pi v/c$, where v is the frequency and c is the velocity of light) from the fundamental propagation constant β_0 (equal to $4\pi/\sqrt{3}a$, where a is the lattice constant) for each cavity mode, and expressed as $\delta = (\beta^2 - \beta_0{}^2)/2\beta_0$, α is the corresponding threshold gain.

By solving Eq. (4. 40), a cavity frequency v for each band-edge mode and the corresponding threshold gain α for a given set of coupling coefficients, κ_1, κ_2, and κ_3, can be obtained. When only the cavity mode frequencies are required, the derivation terms and the threshold gain α in Eq. (4. 40) can be set to zero, and the individual cavity frequencies can then be derived as follows:

$$v_1 = \frac{c}{2\pi n_{eff}}(\beta_0 - \kappa_1 - \kappa_2 + \kappa_3) \quad (4.\ 41a)$$

$$v_2 = \frac{c}{2\pi n_{eff}}(\beta_0 - \frac{1}{2}\kappa_1 + \frac{1}{2}\kappa_2 - \kappa_3) \quad (4.\ 40b)$$

$$v_3 = \frac{c}{2\pi n_{eff}}(\beta_0 + \kappa_1 - \kappa_2 - \kappa_3) \quad (4.\ 41c)$$

$$\nu_4 = \frac{c}{2\pi n_{eff}}(\beta_0 + \frac{1}{2}\kappa_1 + \frac{1}{2}\kappa_2 + \kappa_3) \quad (4.\ 41d)$$

where, c is the velocity of a photon in vacuum, and n_{eff} is the effective refractive index of the device structure. There are four cavity mode frequencies, $\nu_1 - \nu_4$, which correspond to the four band-edge, including two degenerate modes ν_2 and ν_4. Once the cavity mode frequency at the individual band-edges can be obtained, we can derive the coupling coefficients κ_1, κ_2, and κ_3 from Eq. (4. 41) as follows:

$$\kappa_1 = \frac{-\nu_1 - \nu_2 + \nu_3 + \nu_4}{\nu_1 + 2\nu_2 + \nu_3 + 2\nu_4} 2\beta_0 \quad (4.\ 42a)$$

$$\kappa_2 = \frac{-\nu_1 + \nu_2 - \nu_3 + \nu_4}{\nu_1 + 2\nu_2 + \nu_3 + 2\nu_4} 2\beta_0 \quad (4.\ 42b)$$

$$\kappa_3 = \frac{\nu_1 - 2\nu_2 - \nu_3 + 2\nu_4}{\nu_1 + 2\nu_2 + \nu_3 + 2\nu_4} 2\beta_0 \quad (4.\ 42c)$$

By comparing the value of coupling coefficients κ_1, κ_2, and κ_3 based on actual device parameters, we can determine which kind of DFB mechanism provide the major significant contribution to support the lasing oscillation.

II. K2 numerical results

The 2-D PC structure investigated here consists of an infinite triangular lattice with circular air holes in the x and y directions, as shown in Figure 4. 14. The structure is assumed to be uniform in the z direction. We don't consider the gain effects during calculation. While considering infinite structure, the magnetic field can be described by the Bloch mode [18],

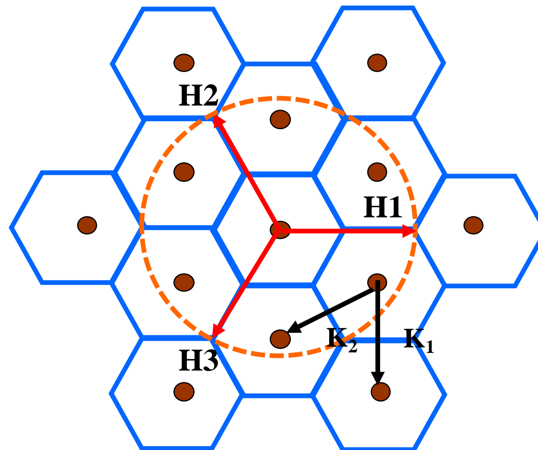

Figure 4. 14 Schematic diagram of three propagation waves in triangular lattice for K2 point

$$Hz(r) = \sum_G h_G \exp\left[j(k+G)\cdot r\right] \tag{4. 35}$$

where

$$Hz = H_1 e^{-i\beta 0 \hat{x}} + H_2 e^{-i\beta 0(\frac{-1}{2}\hat{x}+\frac{\sqrt{3}}{2}\hat{y})} + H_3 e^{-i\beta 0(\frac{-1}{2}\hat{x}-\frac{\sqrt{3}}{2}\hat{y})} \tag{4. 43}$$

put Eq. (4. 43) and Eq. (4. 32) into the wave Eq. (4. 31), and comparing the equal exponential terms, we obtain three wave equations :

$$-\frac{\partial}{\partial x}H_1 + (-\alpha - i\delta)H_1 = i\frac{\kappa}{2}(H_2 + H_3) \tag{4. 44a}$$

$$-\frac{1}{2}\frac{\partial}{\partial x}H_2 - \frac{\sqrt{3}}{2}\frac{\partial}{\partial y}H_2 + (-\alpha - i\delta)H_2 = i\frac{\kappa}{2}(H_1 + H_3) \tag{4. 44b}$$

$$\frac{1}{2}\frac{\partial}{\partial x}H_3 + \frac{\sqrt{3}}{2}\frac{\partial}{\partial y}H_3 + (-\alpha - i\delta)H_3 = i\frac{\kappa}{2}(H_1 + H_2) \tag{4. 44c}$$

where, H_1, H_2, H_3 express the envelope magnetic field distributions of individual light waves propagating in the three equivalent Γ-K directions: 0°, 120°, 240° with respect to the x axis. κ is the coupling coefficient between light waves propagating at 120° to each other (H_1 and H_2, H_2 and H_3, H_1 and H_3), δ is the deviation of the wave number β (expressed as $2\pi v/c$, where v is the frequency and c is the velocity of light) from the fundamental propagation constant β_0 (equal to $8\pi/3a$, where a is the lattice constant) for each cavity mode, and expressed as $\delta = (\beta^2 - \beta_0{}^2)/2\beta_0$, α is the corresponding threshold gain.

By solving Eq. (4. 44), a cavity frequency v for each band-edge mode and the corresponding threshold gain α for a given set of coupling coefficients, κ can be obtained. When only the cavity mode frequencies are required, the derivation terms and the threshold gain α in Eq. (4. 40) can be set to zero, and the individual cavity frequencies can then be derived as follows:

$$v_1 = \frac{c}{2\pi n_{eff}}(\beta_0 - \kappa) \tag{4. 45a}$$

$$v_2 = \frac{c}{2\pi n_{eff}}(\beta_0 + \frac{1}{2}\kappa) \tag{4. 45b}$$

where, c is the velocity of a photon in vacuum, and n_{eff} is the effective refractive index of the device structure. There are two cavity mode frequencies, v_1 and v_2 corresponding to the two band-edge including one degenerate modes v_2. When the cavity mode frequencies at the individual band-edges are obtained, we can derive the coupling coefficients κ from Eq. (4. 45) as follows:

$$\kappa = \frac{\nu_2 - \nu_1}{\nu_1 + 2\nu_2} 2\beta_0 \tag{4. 46}$$

From the 2-D couple-wave model, we know light at K2 band-edge can couple to each other and form the triangular feedback close loop via DFB effect.

III. M3 numerical results

The 2-D PC structure investigated here consists of an infinite triangular lattice with circular air holes in the *x* and *y* directions, as shown in Figure 4. 15. The structure is assumed to be uniform in the *z* direction. We don't consider the gain effects during calculation. While considering infinite structure, the magnetic field can be described by the Bloch mode [18],

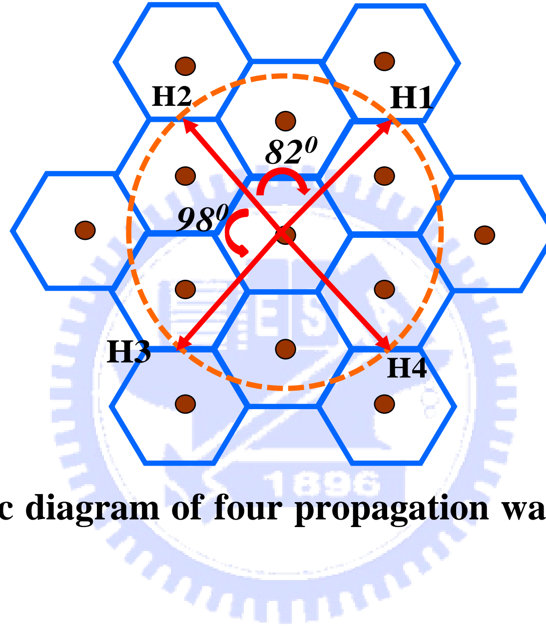

Figure 4. 15 Schematic diagram of four propagation waves in triangular lattice for M3 point

$$Hz(r) = \sum_G h_G \exp[j(k+G)\cdot r] \tag{4. 35}$$

where

$$Hz = H_1 + H_2 + H_3 + H_4 \tag{4. 47}$$

It needs to note that the angle between two propagating waves has been estimated and shown in Figure 4. 15. Here, the phase term will not describe in detail.

put Eq. (4. 47) and Eq. (4. 32) into the wave Eq.(4. 31) ,and comparing the equal exponential terms. Then, we obtain four wave equations:

$$(\beta_0 - \delta)H_1 = -\kappa_1 H_2 + +\kappa_3 H_3 + \kappa_2 H_4 \tag{4. 48a}$$

$$(\beta_0 - \delta)H_2 = -\kappa_1 H_1 + \kappa_2 H_3 + \kappa_3 H_4 \tag{4. 48b}$$

$$(\beta_0 - \delta)H_3 = \kappa_3 H_1 + \kappa_2 H_2 - \kappa_1 H_4 \tag{4. 48c}$$

$$(\beta_0 - \delta)H_4 = \kappa_2 H_1 + \kappa_3 H_2 + \kappa_1 H_3 \quad \text{4. 48d)}$$

where, H_1, H_2, H_3, and H_4 express the envelope magnetic field distributions of individual light waves propagating in the four directions: κ_1, κ_2, and κ_3 are the coupling coefficients between light waves propagating at 82° to each other (H_1 and H_2, H_3 and H_4), at 98° (H_1 and H_4, H_2 and H_3), and at 180° (H_1 and H_3, H_2 and H_4), respectively. δ is the deviation of the wave number β (expressed as $2\pi v/c$, where ν is the frequency and c is the velocity of light) from the fundamental propagation constant β_0 (equal to $4.7\pi/\sqrt{3}a$, where a is the lattice constant) for each cavity mode, and expressed as $\delta = (\beta^2 - \beta_0{}^2)/2\beta_0$, α is the corresponding threshold gain. By solving Eq. (4. 48), a cavity frequency v for each band-edge mode and the corresponding threshold gain α for a given set of coupling coefficients, κ_1, κ_2, and κ_3, can be obtained. When only the cavity mode frequencies are required, the derivation terms and the threshold gain α in Eq. (4. 40) can be set to zero, and the individual cavity frequencies can then be derived as follows:

$$v_1 = \frac{c}{2\pi n_{eff}}(\beta_0 + \kappa_1 - \kappa_2 - \kappa_3) \quad (4.\ 49a)$$

$$v_2 = \frac{c}{2\pi n_{eff}}(\beta_0 - \kappa_1 + \kappa_2 - \kappa_3) \quad (4.\ 49b)$$

$$v_3 = \frac{c}{2\pi n_{eff}}(\beta_0 - \kappa_1 - \kappa_2 + \kappa_3) \quad (4.\ 49c)$$

$$v_4 = \frac{c}{2\pi n_{eff}}(\beta_0 + \kappa_1 + \kappa_2 + \kappa_3) \quad (4.49d)$$

where, c is the velocity of a photon in vacuum, and n_{eff} is the effective refractive index of the device structure. There are four cavity mode frequencies, $v_1 - v_4$, which correspond to the four band-edge. Once the cavity mode frequency at the individual band-edges can be obtained, we can derive the coupling coefficients κ_1, κ_2, and κ_3 from Eq. (4. 49) as follows

$$\kappa_1 = \frac{v_1 - v_2 - v_3 + v_4}{v_1 + v_2 + v_3 + v_4}\beta_0 \quad (4.\ 50a)$$

$$\kappa_2 = \frac{-v_1 + v_2 - v_3 + v_4}{v_1 + v_2 + v_3 + v_4}\beta_0 \quad (4.\ 50b)$$

$$\kappa_3 = \frac{-v_1 - v_2 + v_3 + v_4}{v_1 + v_2 + v_3 + v_4}\beta_0 \quad (4.\ 50c)$$

By comparing the value of coupling coefficients κ_1, κ_2, and κ_3 based on actual device parameters, we can determine which kind of DFB mechanism provide the most significant

contribution to support the lasing oscillation. So far, the couple-wave model for different band-edge has been established.

4-3 Design of GaN-based 2-D PCSELs

In this section, we focus on the design for our GaN-based 2-D PCSELs. First, we use the as-grown samples consisted of a 150nm-thick p-GaN layer, 10-pair $In_{0.2}Ga_{0.8}N$(2.5 nm)/GaN(12.5 nm) multi-quantum wells (MQWs), a 560 nm-thick n-GaN layer, a 29-pair distributed Bragg reflector (DBR), and a 2 μm-thick u-GaN layer on 2-inch sapphire substrates. Among of as-grown samples, the active region composed of a p-GaN layer, MQWs, and a n-GaN layer has 5-lamda optical thickness and the DBR layer plays the role of a low refractive index layer that can confine the optical field in the active region and enhance the coupling between the optical field and photonic crystal nanostructure at the same time. That is, it can further decrease the threshold gain and become easy to observe the fundamental and high order lasing modes in our PhC laser devices.

Initially, we calculate the TE-like mode dispersion band diagram to determine the normalized frequency which we choose for specific band-edge groups. Normalized frequency is the ratio of the lasing wavelengths of optical modes and the PhC lattice constants. Once the lasing wavelength is determined, the lattice constant is certain to be determined. The lasing wavelength is located within the emission of the active layer. According to the theory described in section 4.1 and 4.2, the surface emitting laser in the photonic crystal grating structure could only happen as the Bragg condition is satisfied. In additional, the Bragg condition is satisfied at Brillouin zone boundary including Γ, K and M points. At these points, light waves have opportunity to diffract normally to the sample surface which was described in section 4.1. Therefore, we can design a GaN-based 2-D PCSEL operating at the designed lasing wavelength with the optimized PhC lattice constant at Brillouin zone boundary, Γ, K and M point, which can be defined in the photonic band diagram.

In this study, we fix the parameter, r/a, to be 0.28 for calculating the band diagram of PhC using 2-D plan wave expansion method (PWEM). In fact, the 2-D PWEM couldn't precisely evaluate the photonic band diagram of our 3-D structure. That means we should do some modification to parameters describing our structure and then bring them into the 2-D PWEM to approximate real condition. Therefore, according to reference [8], we further bring two parameters including confinement factor (Γ_g) and effective refractive index (n_{eff}) into our calculation. Γ_g is the ratio of the light field confined within the 2-D PhC structure to the light inside the whole device, and n_{eff} is the effective refractive index of the entire device with PhC that take into account the effects of partial modal overlap of electromagnetic fields. Γ_g and n_{eff} could be used to estimate the effective dielectric constant of nano-hole (ε_a) and the background (ε_b) for 2-D PWEM calculation to further

approximate the 3-D structure. These two parameters can be obtained by solving the distribution of the electric field in the in-plane direction. The Γ_g and n_{eff} for describing our structure are estimated to be 0.563 and 2.495 considering fundamental mode, respectively. It is first estimated by transfer matrix method and shown in Figure 4. 16.

Then, we could determine ε_a and ε_b using two conditions:

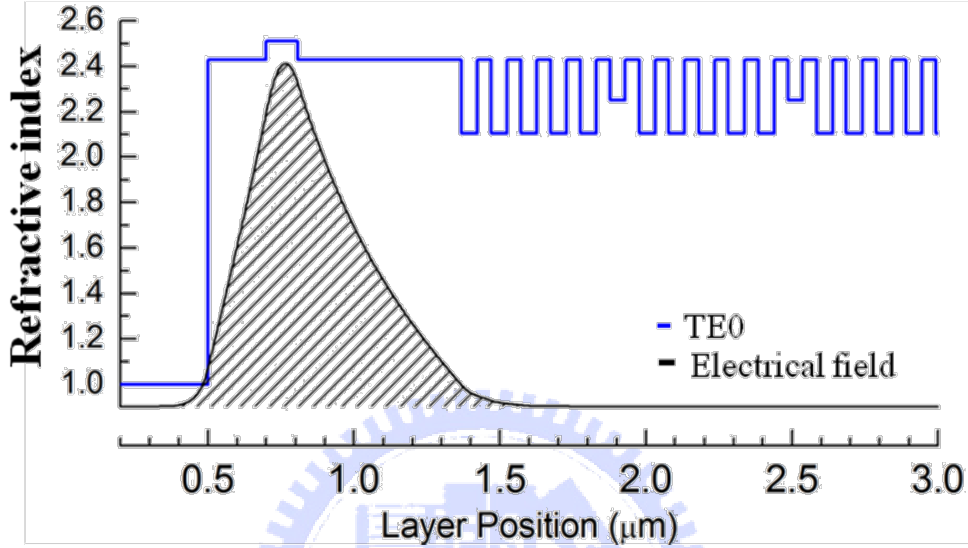

Figure 4. 16 The lowest guided mode optical field distribution, where the confinement factor Γ_g=0.73 and n_{eff}=2.44.

$$n_{eff}^{2} = f\varepsilon_a + (1-f)\varepsilon_b \tag{4. 51}$$

$$\Delta\varepsilon = \varepsilon_b - \varepsilon_a = \Gamma_g(\varepsilon_{mat} - \varepsilon_{air}) \tag{4. 52}$$

where the f is a filling factor, ε_{mat} is the dielectric constant of semiconductor, and ε_{air} is the dielectric constant of air. For a triangular-lattice PhC, f is written as:

$$f = \frac{2\pi r^2}{\sqrt{3}a^2} \tag{4. 53}$$

Therefore, the value of ε_a and ε_b in unit cell for our PhC device could be obtained the values of about 4.11 and 7.07, respectively. To bring ε_a and ε_b into the calculation, a band diagram of the 2-D PhC structure with triangular lattice for TE-like mode with r/a=0.28 on our sample structure could be estimated as shown in Figure 4. 17. The figure shows that the dispersion curve of each mode would cross and splits at specific band-edges, and the mode density is higher at those boundaries. Light at these areas can propagate along different direction and have chance to couple and form a laser cavity. According to the theory described in section 4.1, the surface emitting behavior in the photonic crystal grating structure could only happen when the Bragg condition is satisfied.

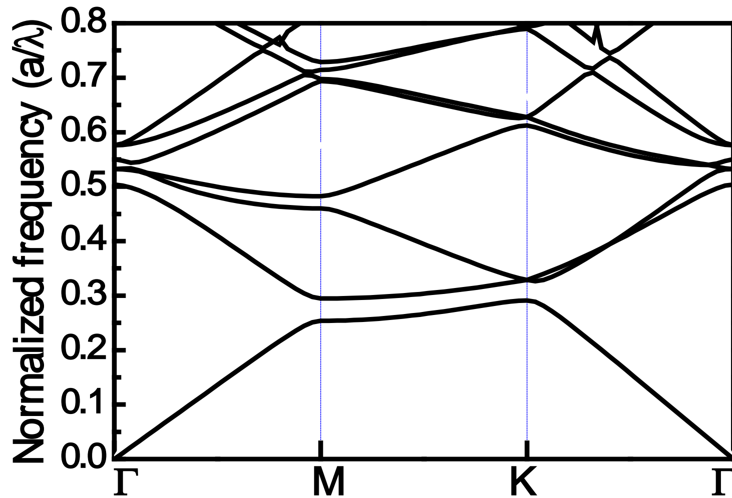

Figure 4. 17 The band diagram of the 2-D triangular-lattice PhC structure on our sample structure. The value of *r*/*a* here is 0.28.

In order to get a high opportunity of those band edge modes satisfying Bragg condition, the lattice constants of photonic crystal were determined between 190 nm and 300 nm correspond to the normalized frequency ranging from 0.45 to 0.7, considering a PL peak wavelength of as-grown samples ranging from 380 nm to 460 nm.

4-4 Fabrication of GaN-based PCSELs

Recently, photonic crystal (PhC), which are periodic patterns with sizes of nano-scale, are usually fabricated by different technologies including E-beam lithography (EBL), holograph lithography, and nanoimprint method. However, holograph lithography has the limitation of the PhC pattern including PhC lattice constant and radius of PhC hole. The nanoimprint method has the difficulties to fabricate PhC imprint masks, lift-off PR/PMMA films from the samples, and expensive instruments. Therefore, the most popular method to fabricate the PhC pattern is the E-beam lithography because of these advantages including cheaper instruments, higher resolution, and easy to design and fabricate PhC patterns.

Fabrication Technique – Electron-Beam Lithography

The EBL is a technique using electron beam to generate patterns on a surface with a resolution limited by De Broglie relationship (λ < 0.1 nm for 10-50 KeV electrons), which is far smaller than the light diffraction limitation. Therefore, it can beat the diffraction limit of light to create a pattern which only has a few nanometers line-width without any mask. The first EBL machine, based on

SEM system, was developed in the 1960s. The EBL system usually consists of an electron gun for generating electron beam, a beam blanker for controlling the electron beam, electron lenses for focusing the electron beam, a stage and a computer control system as shown in Figure 4. 18.

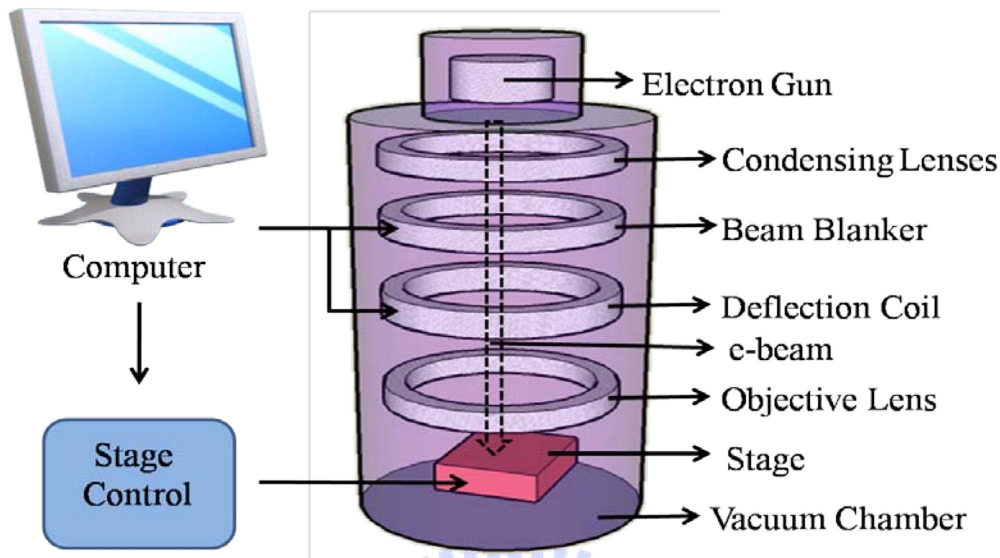

Figure 4. 18 The typical schematic diagram of EBL system.

In the process of EBL, the specific Polymethylmethacrylate (PMMA) is required and used to form patterns via exposure of electron beam. In the experiment, we used a special positive PMMA, A3, to form patterns. These parameters for EBL here are described as below.

1. **Spin coating PMMA (A3):**
   a. first step : 1000 rpm for 10 sec.
   b. second step : 5000 rpm for 90 sec.
2. **Hard bake :** hot plate 120 ^{o}C, 1 hr.
3. **Exposure :**
   Beam voltage : 10 KeV
   Writefield size : 50 μm
   Dot dose : 0.08 pAs
4. **Development :** dipping in IPA : MIBK(3 : 1) 50 sec.
5. **Fixing :** rising in IPA 30 sec.
6. **Hard bake :** hot plate 120 ^{o}C, 4 min.

<u>Fabrication processes for GaN-based VCSELs</u>

The PCSELs was fabricated by following process steps as shown in Figure 4. 19. In the beginning, the hard mask SiN_x 200 nm was deposited on as-grown samples by PECVD. Then PMMA layer (150 nm) was spun by spinner and exposed using E-beam writer to form soft mask.

The pattern on soft mask was transferred to SiN_x film to form the hard mask by using ICP-RIE (Oxford Plasmalab system 100), and then the PMMA layer was removed by dipping ACE. The pattern on hard mask was transferred to GaN by using ICP-RIE (SAMCO RIE-101PH) to form the PC layer. In order to remove the hard mask, the sample is dipped in BOE. Finally, the PCSEL devices have been fabricated as shown in Figure 4. 20.

Figure 4. 21 shows the plane-view (a) and the cross section (b) of SEM images of our photonic crystal surface emitting lasers.

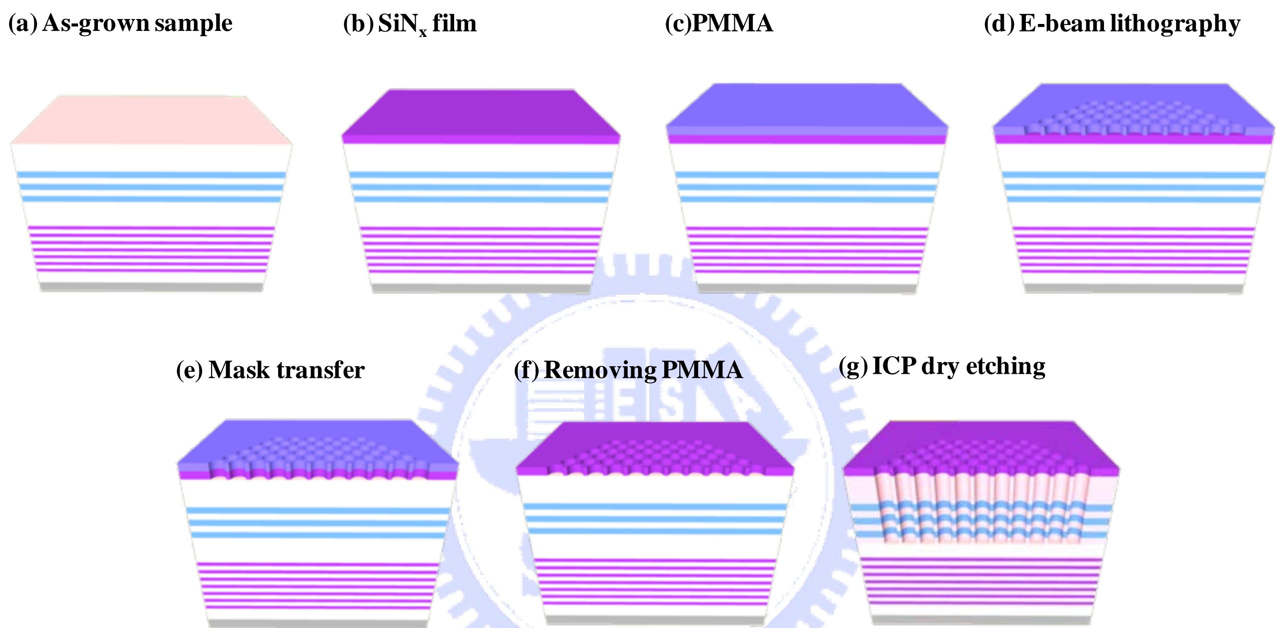

Figure 4. 19 PCSEL fabrication flowcharts: (a) as-grown sample structure, (b) deposit SiNx film by PECVD, (c) spin on PMMA, (d)E-beam lithography, (e) PC patter transfer to SiN_x layer, (f) remove PMMA by Acetone, and (g) PC patterns transfer to GaN layer.

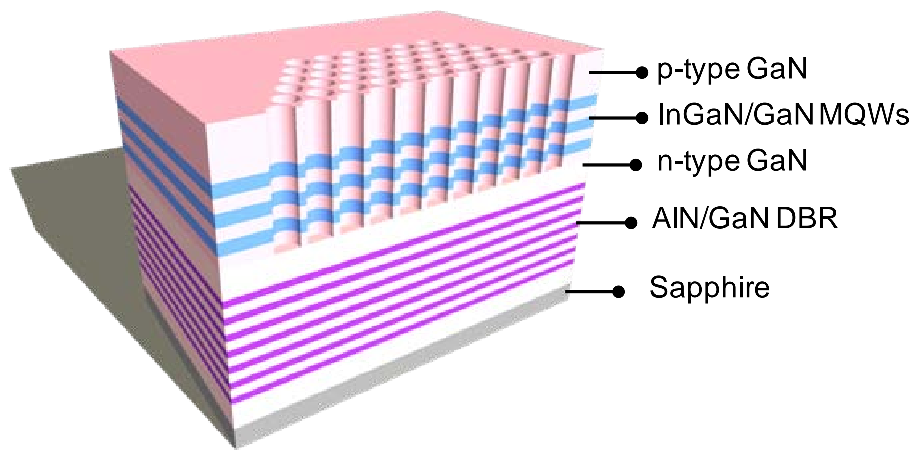

Figure 4. 20 The GaN-based PCSEL devices with AlN/GaN DBRs

(a)

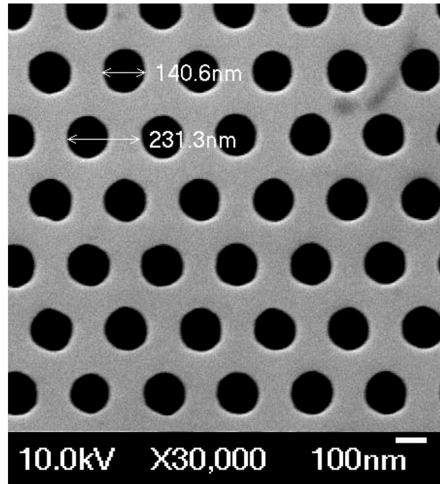

(b)

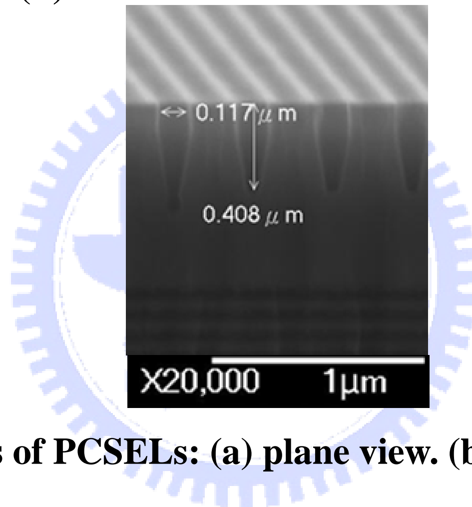

Figure 4. 21 SEM images of PCSELs: (a) plane view. (b) cross-section view.

Reference.

[1] M. Imada, S. Noda, A. Chutinan, T. Tokuda, M. Murata, and G. Sasaki, *Appl. Phys .Lett*., **75**, 316 (1999)

[2] S. Noda, M. Yokoyama, M. Imada, A. Chutinan, and M. Mochizuki, *Science,* **293**, 1123 (2001)

[3] H. Y. Ryu, S. H. Kwon, Y. J. Lee, and J. S. Kim, *Appl. Phys. Lett,.* **80**, 3467 (2002)

[4] G. A. Turnbull, P. Andrew, W. L. Barns, and I. D. W. Samuel, *Appl. Phys. Lett.,* **82**, 313 (2003)

[5] K. Sakai, E. Miyai, T. Sakaguchi, D. Ohnishi, T. Okano, and S. Noda, *IEEE J. Sel. Areas Commun.,* **23**, 1335 (2005)

[6] M. Imada, A. Chutinan, S. Noda and M. Mochizuki *Phys. Rev. B,* **65**, 195306 1 (2002)

[7] M. Yokoyama and S. Noda *Opt. Express,* **13**, 2869 (2005)

[8] M. Imada, A. Chutinan, S. Noda, M. Mochizuki, *Phy. Rev. B*, **65**, 195306 (2002)

[9] M. Notomi, H. Suzuki, and T. Tamamura, *Appl. Phys. Lett.*, **78**, 1325 (2001)

[10] Fre´de´ric S. Diana, Aure´lien David, Ines Meinel, Rajat Sharma, Claude Weisbuch, Shuji Nakamura and Pierre M. Petroff, *Nano Lett.*, **6**, 1116 (2006)

[11] Soller, B. J.; Stuart, H. R.; Hall, D. G. *Opt. Lett.*, **26**, 18, 1421 (2001)

[12] A. David, C. Meier, R. Sharma, F. S. Diana, S. P. DenBaars, E. Hu, S. Nakamura, C. Weisbuch, H. Benisty, *Appl. Phys. Lett.*, **87**, 101107 (2005)

[13] H. Kogelnik and C. V. Shank *Appl. Phys. Lett.* **43**, 2327 (1972)

[14] Distributed Feedback Laser Diodes and Optical Tunable Filters

[15] W. Streifer, R. D. Burnham, and D. R. Scifres, *IEEE J. Quantum Electron.* **QE11**, 154 (1975).

[16] K. Sakai, E. Miyai and S. Noda, *Optics Express*., **15**, 3981, (2007)

[17] K. Sakai, E. Miyai and S. Noda, *Appl. Phys. Lett.*, **89**, 021101 (2006)

[18] Plihal and A. A. Maradudin, *Phys. Rev. B,* **44**, 8565 (1991)

[19] H. Kogelnik, *Bell Syst. Tech. J.*, **48**, 2909 (1969)

[20] T. Ochiai and K.Sakoda *Phys. Rev. B,* **63**, 125 107-1-125 107-7, (2001)

Chapter 5

Characteristics of Optical Pumped GaN-based 2-D PCSELs

5-1 Band-edge modes in dispersion curves

In this section, we will simulate the dispersion curves of photonic crystal nanostructure by plane wave expansion method (PWEM). From the dispersion curves, there are two axis including normalized frequencies (ratio of photonic crystal lattices and wavelength) and in-plane *k* vector directions ($K_0 sin\theta$) showing different PhC band-edge modes such as Γ, K, and M. According to the position of normalized frequencies of the dispersion curves, we can distinguish the relation between lasing wavelengths and what the PhC laser modes are.

<u>Optical pumping system (Angle-resolved *μ*-PL)</u>

The angle-resolved μ-PL (AR μ-PL) system is designed for multiple choices. As shown in Figure 5. 1, we have two optical pump sources, two optical pump incidence paths, two collecting PL method and two way to collect sample surface image. The two optical pump sources are: one is frequency tripled Nd:YVO_4 355 nm pulsed laser with a pulse width of ~0.5ns at a repetition rate of 1KHz; the other is 325 nm He-Cd continuous wavelength laser. The samples are optically pumped by laser beam with an incident angle of 0 degree or 60 degree to the sample. The laser spot size is about 50 μm in diameter so that covering the whole PhCs pattern area. The PL is collected by a 15 X objective lens and straightly collected by spectrometer with a charge-coupled device (Jobin-Yvon iHR320 Spectrometer) or collected by a fiber with a 600 μm core, which rotating in the normal plane of the sample, and also coupled into spectrometer. The spectral resolution is about 0.07 nm for spectral output measurement. Figure 5. 1 shows the setup of our AR μ-PL system. The GaN-based PCSELs were placed in a cryogenics controlled chamber for performing PL experiment under low temperature (in order to prevent damage caused by heat). The temperature of the chamber can be controlled from room temperature (300 K) down to 77 K via the liquid nitrogen. We can also monitor the image and spatial

distribution on the sample surface by charge-coupled device (CCD) and beam view, respectively.

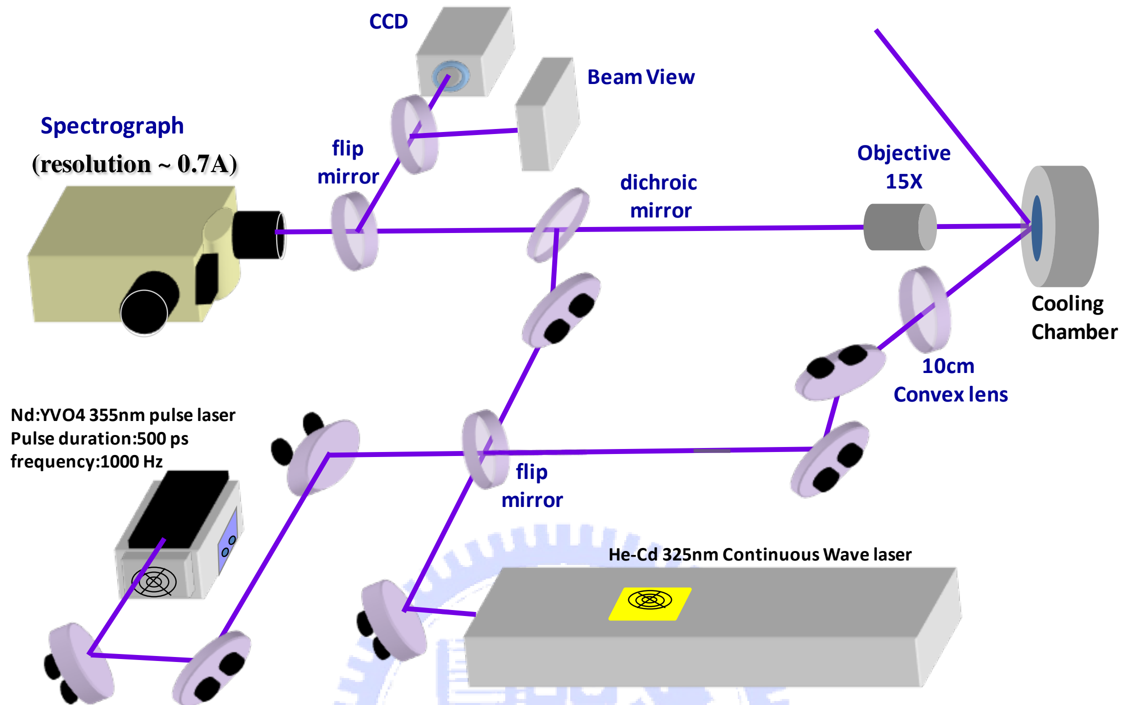

Figure 5. 1 The angular-resolved μ-PL (AR μ-PL) system

Photoluminescence of the PCSEL structure

The typical photoluminescence (PL) spectrum of as-grown samples, as shown in Figure 5. 2, had a peak centered at a wavelength of 425 nm with a linewidth of 25 nm. At normal incidence at room temperature, the DBR showed the highest reflectivity of 99 % at the center wavelength of 430 nm, with a stopband width of about 30 nm, measured by an *n&k* ultraviolet-visible spectrometer as shown in Figure 5. 3. Here, we used the circular hole diameter *r* chosen such that *r/a* is about 0.28. After the PMMA layer was removed by acetone, we used ICP-RIE to etch down the as-grown sample to about 400 nm deep. The etching penetrated the MQWs active regions and created the PC patterns in the nitride layers. Finally, the SiN_x hard mask was removed by buffered oxide etch dipping. The structure of GaN-based 2-D photonic crystal surface emitting lasers (PCSEL) with bottom AlN/GaN distributed Bragg reflectors (DBR) are as shown in section 4.4.

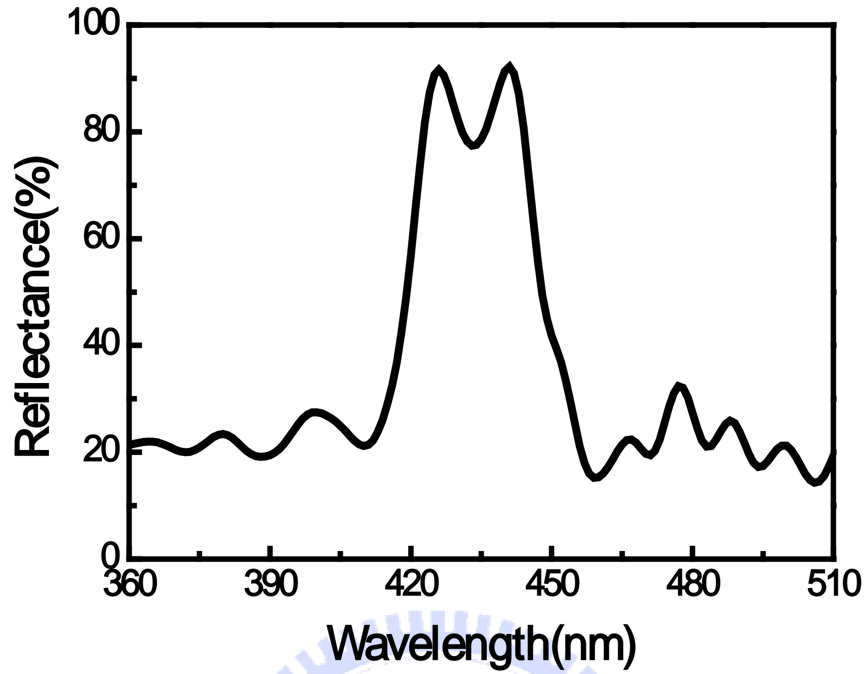

Figure 5. 2 Reflectivity spectrum of the half structure with 35 pairs of GaN/AlN DBRs measured by N&K ultraviolet-visible spectrometer with normal incident at room temperature.

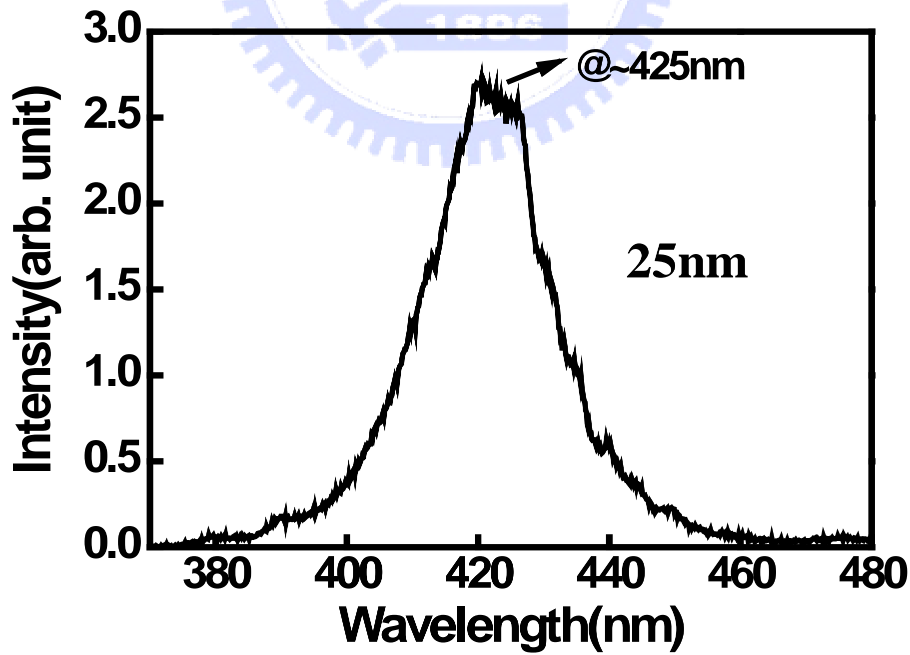

Figure 5. 3 The u-PL spectrum of as-grown sample

Threshold characteristics

In our PCSEL devices, the lasing action was clearly observed in several different devices with different lasing wavelength from 395 nm to 425 nm. Take the PC lattice constant 254 nm for example. Figure 5. 4 shows the output emission intensity as a function of the pumping energy density. The clear threshold characteristic is observed at the threshold pumping energy density of 2.8 mJ/cm2, with a peak power density of 5.6 MW/cm^2. Then the laser output intensity increases abruptly and linearly with the pumping energy above the threshold energy. Figure 5. 5 shows the excitation energy dependent emission spectrums from 0.8 E_{th} to 1.3 E_{th}. These spectrums clearly show the transition behavior from spontaneous emission to stimulated emission. Above the threshold, we can observe only one dominant peak wavelength of 419.7 nm with a linewidth of 0.19 nm.

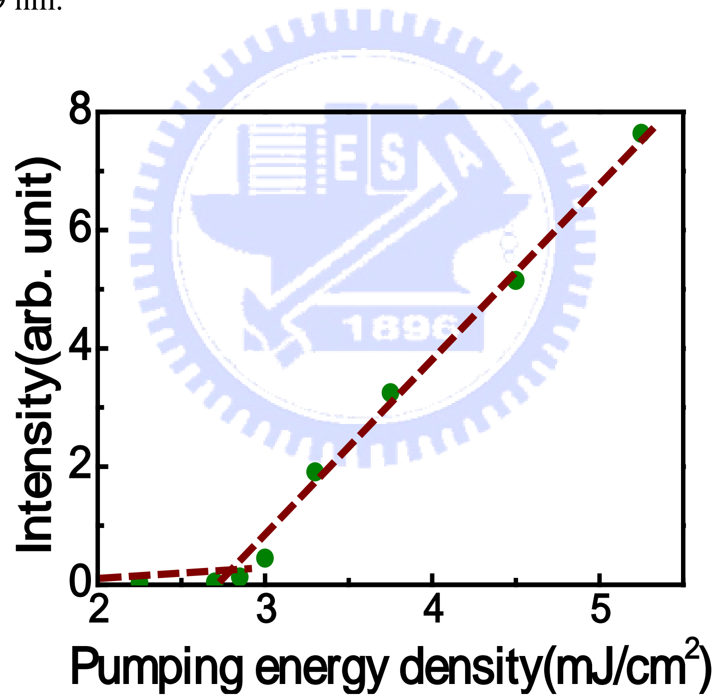

Figure 5. 4 Laser intensity as a function of pumping energy density

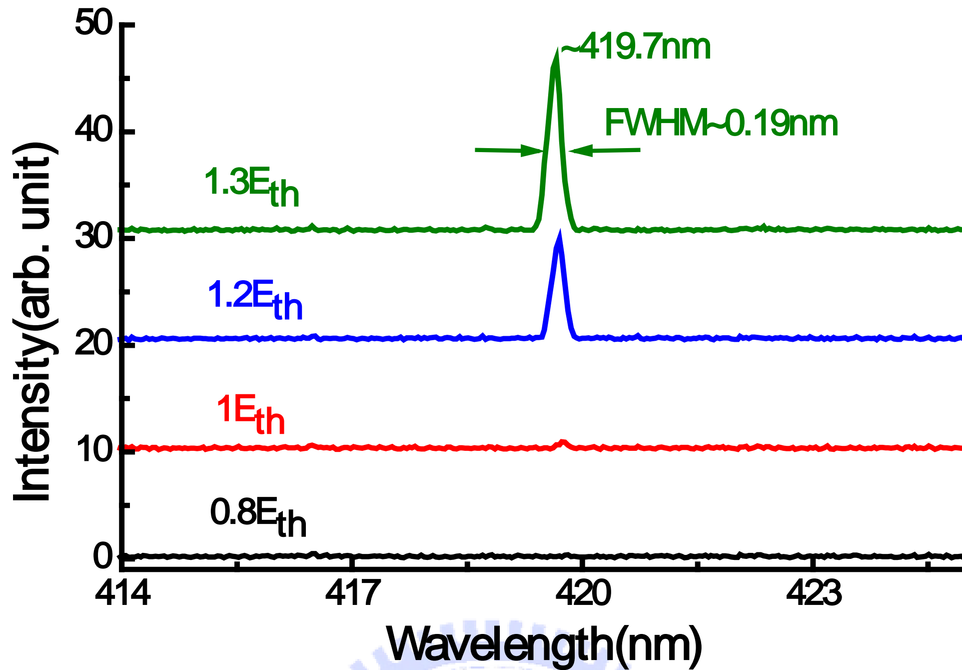

Figure 5. 5 The lasing spectrums under different pumping energy densities

It's worth noting that the single mode lasing phenomenon only occurs in the area with PC patterns. On the other hand, multiple lasing peaks were occurred when the area without PC patterns was pumped at the threshold energy density two-order of magnitude higher. The normalized frequency (lattice constant over wavelength, a/λ) for the lasing wavelength emitted from our PC lasers with different lattice constants were plotted as shown in Figure 5. 6(a). All the PhC lasers have lasing peaks in a range from 401 nm to 425 nm. It can be seen that the normalized lasing frequency (dotted points in the figure) increased with the lattice constant in a discontinues and step-like fashion. To calculate the band diagram of the hexagonal PhC patterns in this structure, we employ the plane-wave expansion method in two-dimensions with an effective index approach that took into account the effects of partial modal overlap of electromagnetic fields with the PhC structures [1]. As a starting point, the ratio of light confined within the 2-D PhC structure to light extended in the entire device, Γ_g, and the effective refractive index of the entire device n_{eff} were first estimated by the transfer matrix method. The calculation shows that the lowest order guided mode has the highest confinement factor for both PC and MQW

regions and the Γ_g, and n_{eff} are estimated to be 0.563 and 2.495, respectively. Then, we determine the effective dielectric constants of the two materials in the unit cell, ε_a and ε_b, using $n_{eff}{}^2 = f\varepsilon_a + (1-f)\varepsilon_b$ and $\Delta\varepsilon = \varepsilon_b - \varepsilon_a = \Gamma_g(\varepsilon_{mat} - \varepsilon_{air})$, where, the $f = \dfrac{2\pi r^2}{\sqrt{3}a^2}$ is a filling factor and ε_{mat} and ε_{air} are dielectric constants of GaN (= 2.5^2) and air (= 1^2), respectively. The values of ε_a (4.11) and ε_b (7.07) thus obtained were then put into the calculation of the band diagram for the 2-D hexagonal-lattice structure with $r/a = 0.28$.

Figure 5. 6(b) shows the calculated dispersion curve of the 2-D hexagonal-lattice structure for transverse-electric mode. It can be expected that the lasing occurs at special points such as at Brillouin-zone boundary near the band edges, because the Bragg condition is satisfied and the density of states is higher in these points [1]. At these lasing points, wave can propagate in different directions and couple with each other. The dotted lines are guides for band edges calculated in Figure 5. 6(b) and extended horizontally to Figure 5. 6(a) with the same normalized frequency. It can be seen that different groups of the normalized frequency observed in the PC samples with different lattice constants occur exactly at band edges such as Γ, M, and K points, indicating that the laser operation was provided by multidirectional distributed feedback in the 2-D PC nanostructure [2]. The characteristics of Γ, M, and K points lasing can be further identified by the polarization angle of the output emission shown in the following section [3]. Note that the output intensity is higher when some of the lasing frequencies are in the stopband of DBR, which could be due to that the bottom DBR here could be treated as a high reflectivity reflector, facilitating top-emission efficiency.

The lasing area of the GaN-based 2-D PCSEL, obtained by a CCD camera is relatively large which covers almost whole area of PhC pattern with only one dominant lasing wavelength as shown in Figure 5. 7. It’s interesting to note that the threshold power density of GaN-based 2-D PCSEL is in the same order of or even better than the threshold for GaN-based VCSEL we demonstrated recently [4]. Unlike the small emission spots observed in the GaN-based VCSELs, the large-area emission in 2-D PCSEL has great potential in applications required high power output operation.

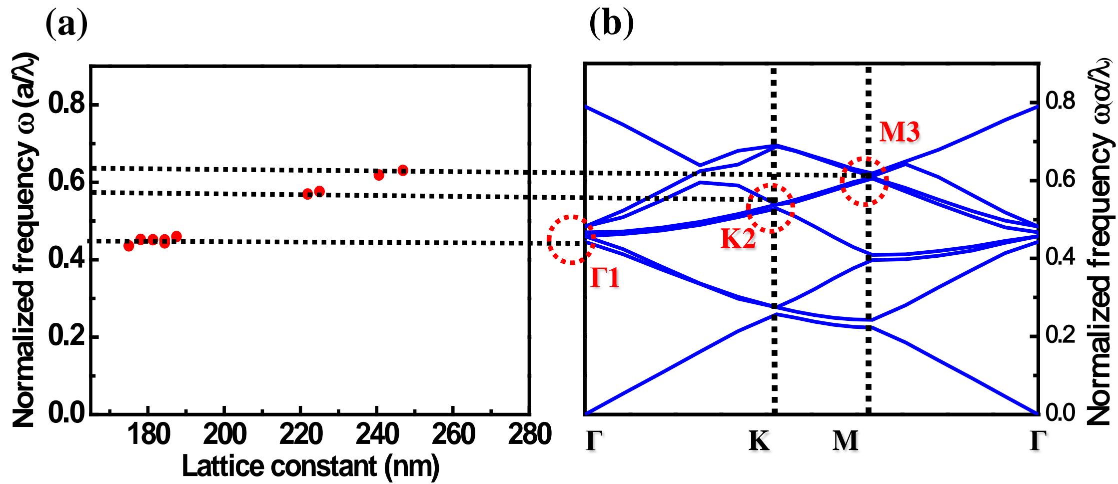

Figure 5. 6 (a) Normalized frequency as a function of the lattice constant. The solid circle points are the lasing wavelengths from the different PhC structures. (b) Calculated band diagram of the 2-D hexagonal-lattice structure. The dotted lines are guides for band edges.

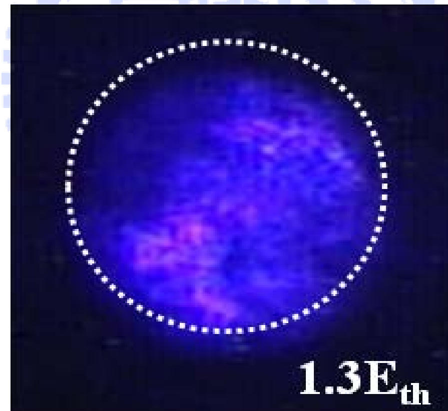

Figure 5. 7 The lasing CCD image is at 1.3 E_{th} and the dash circle is the PhC nanostructure region of about 50μm

The coupling efficiency of spontaneous emission (*β*)

In order to understand the *β* of this PhC cavity, we plotted the L-I curve in a logarithm scale as shown in Figure 5. 8. The spontaneous emission coupling efficiency *β* value is about $5*10^{-3}$.

This value of the PCSEL is similar to the value of VCSEL but one order of magnitude higher than that of the typical edge emitting semiconductor lasers (normally

about 10^{-5}) [5], , indicating the enhancement of the spontaneous emission into a lasing mode by the high quality factor microcavity effect in the PCSEL structure.

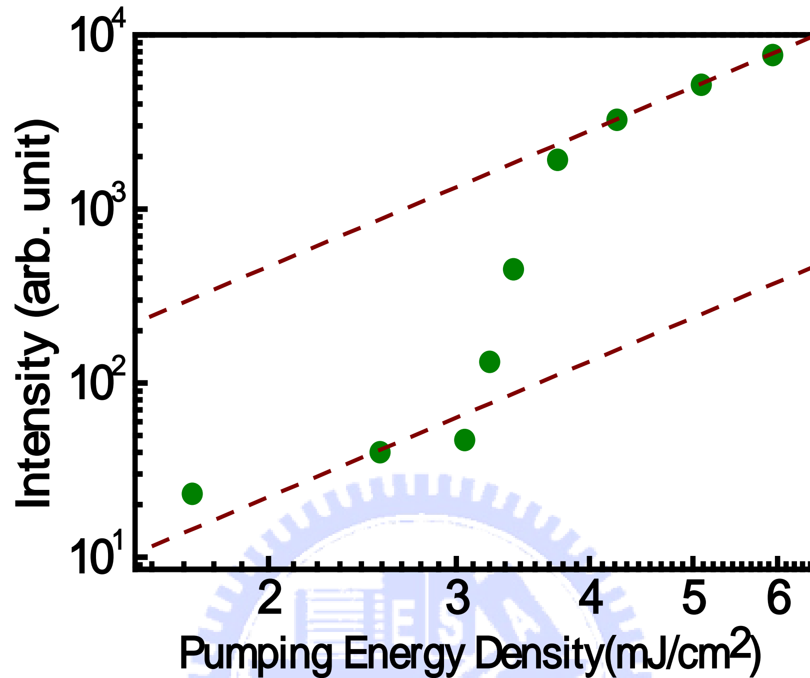

Figure 5. 8 The spontaneous emission coupling factor of GaN-based 2-D PCSEL

<u>**Quality factor of the VCSEL structure**</u>

In general, the cavity quality factor is defined as $Q = \frac{\lambda}{\Delta\lambda}$, where λ is the wavelength emitted from cavity and $\Delta\lambda$ is the FWHM of the emission peak. In our experiment, we cannot obtain the Q value of our PCSEL structure because our PCSEL devices operate at the band-edge modes of the dispersion curve. Therefore, the devices have more loss paths. According to the following equation, the value can be estimated but have some inaccuracies because the theoretical estimation doesn't consider the fabrication problems and non-uniform of InGaN material in the MQWs region. First, the spontaneous emission coupling factor is estimated of about $5*10^{-3}$ and then we can calculate the Purcell factor of about $5*10^{-3}$ as shown in Eq. (5. 1), where F_p is Purcell factor. In Eq. (5. 2), n is the GaN refractive index of about 2.5 and V_C is the optical volume of laser emission. Here, the PhC fabrication area with a PhC lattice constant of

about 234nm is a 50-µm circle in diameter. Then, *Vc* has a volume of about 47 μm^3 and lasing wavelength is about 402 nm. Finally, we can calculate the quality factor (*Q*) about 743.

$$\beta = \frac{F_p}{1 + F_p} \qquad (5.\ 1)$$

$$F_p = \frac{3Q\lambda^3}{4\pi^2 n^3 V_c} = 5\times 10^{-3} \Rightarrow Q = \frac{4\pi^2 n^3 V_c F_p}{3\lambda^3} \qquad (5.\ 2)$$

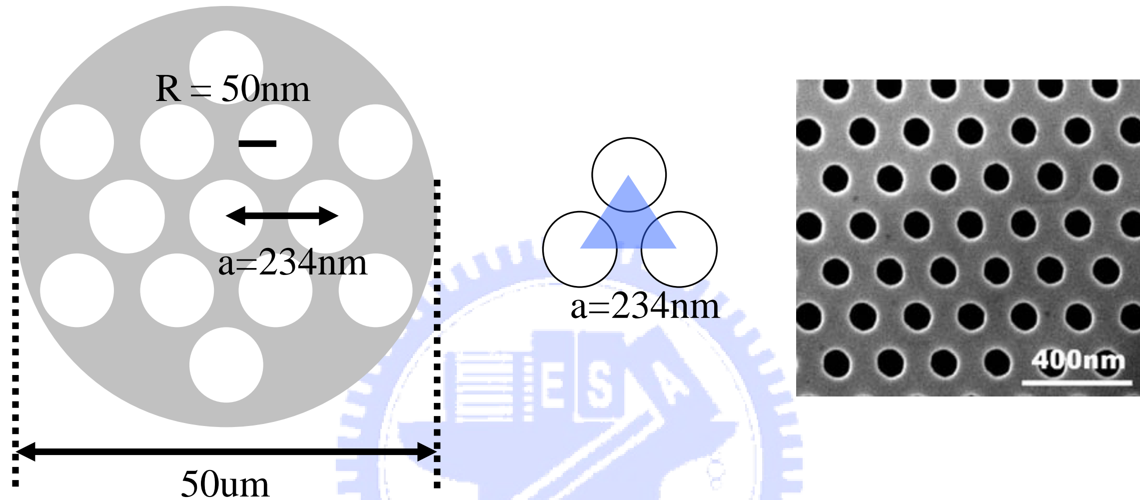

Figure 5. 9 The calculation schematic diagram and the plane-view SEM image

Characteristic Temperature

Figure 5. 10 shows the seminatural-logarithm plots of the dependence of the threshold pumping energy (*In* (E_{th}) on the operation temperature (T_0). The threshold energy gradually increased as the operation rose from 100 K to 300 K. The relationship between the threshold energy and the operation temperature could be characterized by the equation: $E_{th}=E_o*exp\ (T/T_o)$, where T_o is the characteristic temperature and E_o is a constant. Therefore, we obtain a characteristic temperature of about 148 K by linear fitting of the experiment data, which is close to the value reported for GaN-based edge emitting lasers [6]

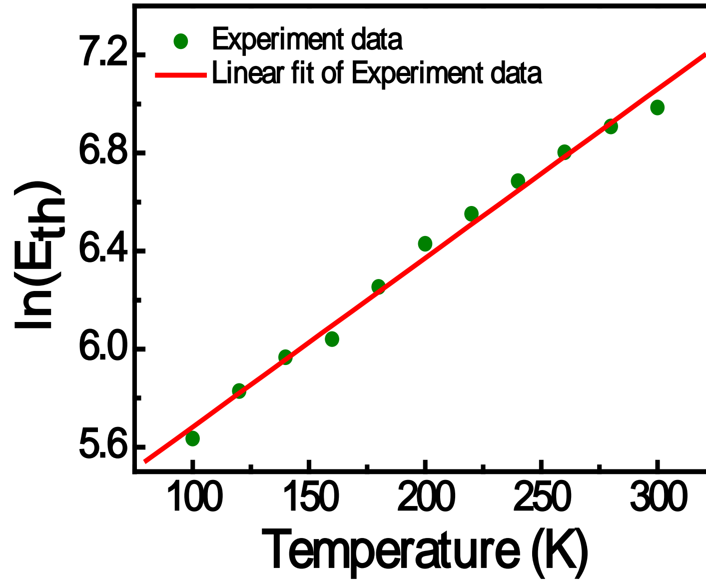

Figure 5. 10 Temperature dependence of the lasing threshold pumping energy (E_{th}).

Far field pattern (FFP)

The far-field patterns (FFP) of the laser were detected by an angular-resolved optical pumped system as shown in Figure 5. 11. In this figure, the lasing far field profiles with different distances from the sample surface were measured. When we increased the measurement distance, the lasing spot sprits into four points with two axes, Γ-M and Γ-K directions, indicated the lasing has strong direction and energy concentration properties in real space. Then, we re-plotted the lasing spot sizes as a function of the measurement distance as shown in Figure 5. 11. From the figure, it shows the divergence angle of PCSEL determined by the distance of two lasing spot axes of about 5.6 degree which is smaller than edge emitting laser (~10^0~20^0) and VCSEL(8^0).

Increase the measurement distance from the sample surface

Figure 5. 11 The far field pattern with different distance from the sample surface collected by objective lens

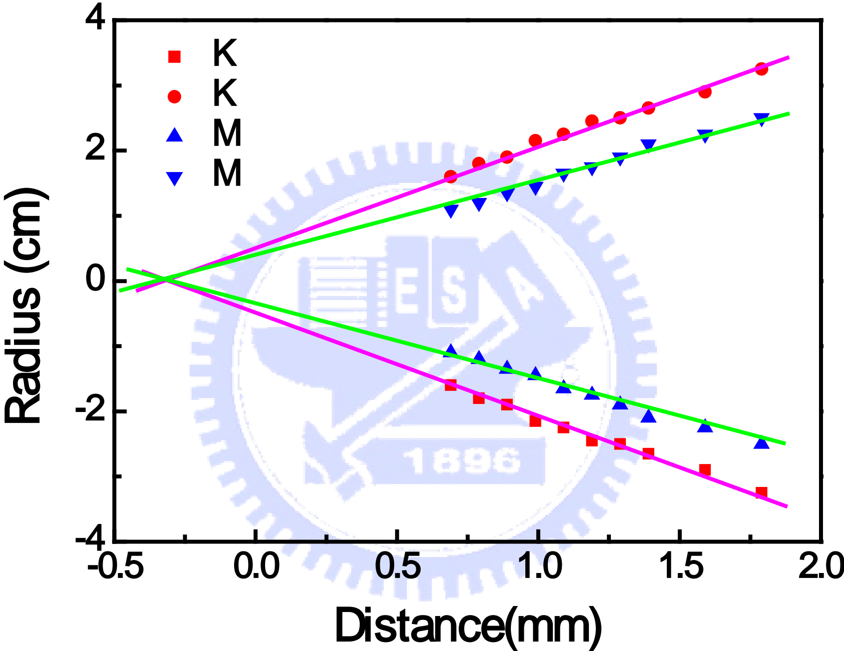

Figure 5. 12 The divergence angle between the two axes.

5-2 Threshold power characteristics with different coupling coefficients

In our experiment, we had measured fundamental mode and other high order modes has different threshold pumping powers. In order to understand the physical mechanism, we applied the couple-wave model in our PCSEL devices and discussed the operation principle in section 4.2 for triangular PhC lattice. In the following section, we will calculate the coupling coefficient at Γ1, K2 M3 band- edge modes and figure out the relation between the calculated coupling coefficient and the experimental threshold

pumping power.

Γ1 numerical results

The design for lasing action at Γ1 device which parameters are described as follows:

$$r/a=0.25,\ a=180\text{nm},\ n_b=2.65,\ n_a=1.87,\ n_{eff}=2.495$$

put these parameters in R-soft software and plot the dispersion curve for TE-like mode as shown in Figure 5. 13

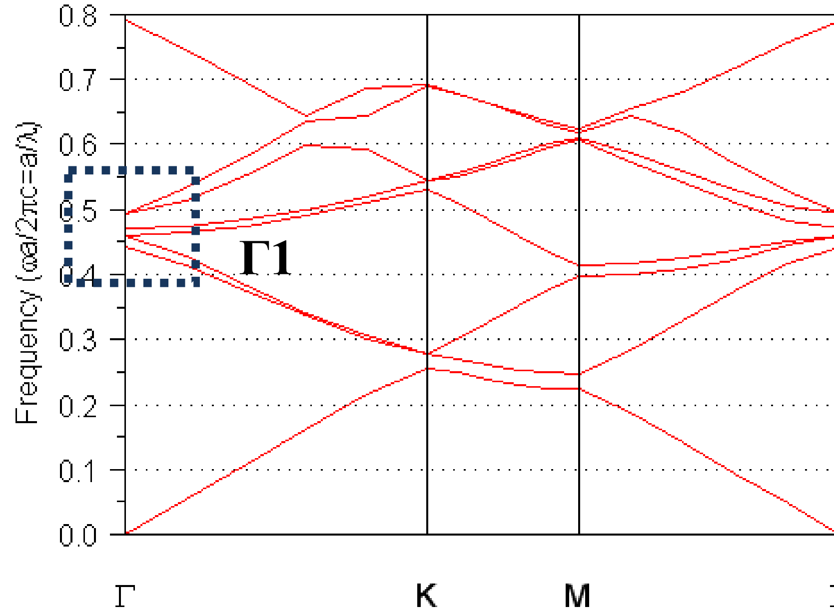

Figure 5. 13 Dispersion curve for TE like mode for Γ1 case

For the band-edge Γ1, there are four cavity mode frequencies, two are degenerated. T The cavity mode frequency can be obtained via simple transform of the normalized frequency which derived from R-soft. The normalized frequency values from lower to higher are 0.448, 0.460, 0.4704, and 0.4930. Once the cavity mode frequency at the individual band-dges can be obtained, we can derive the coupling coefficients κ_1, κ_2, and κ_3 from Eq. (4. 42) and its values are 17480 cm^{-1}, 11240 cm^{-1} and 11248 cm^{-1}, respectively. Therefore, for Γ1, the lasing oscillation forms a hexagonal cavity which provided the major significant contribution to support the lasing action.

K2 numerical results

The design for lasing action at K2 device which parameters are described as follows:

r/a=0.26, a=220nm, n_b=2.63, n_a=2.0, n_{eff}=2.495

put these parameters in R-soft software and plot the dispersion curve for TE-like mode as shown in Figure 5. 14.

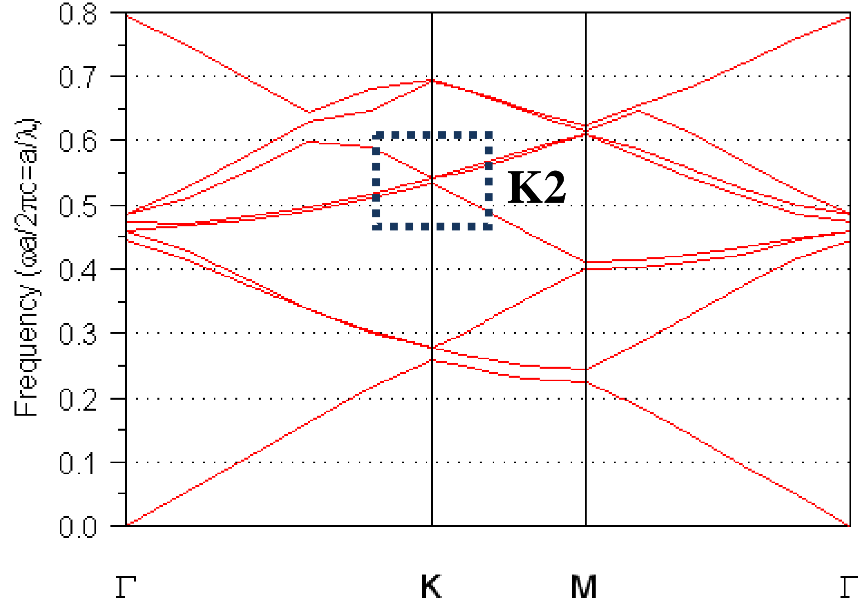

Figure 5. 14 Dispersion curve for TE like mode for K2 case

For the band-edge K2, there are two cavity mode frequencies, one is degenerated. The cavity mode frequency can be obtained via simple transform of the normalized frequency which derived from R-soft. The normalized frequency values from lower to higher are 0.5326 and 0.5413. Once the cavity mode frequency at the individual band-edges can be obtained, we can derive the coupling coefficients κ from Eq. (4. 46) is 4089 cm^{-1}. Therefore, for K2, the lasing oscillation forms a triangular cavity which provided energy to support the lasing action.

<u>M3 numerical results</u>

The design for lasing action at M3 device which parameters are described as follows:

r/a=0.266, a=247nm, n_b=2.64, n_a=2.01, n_{eff}=2.495

put these parameters in R-soft software and plot the dispersion curve for TE-like mode as shown in Figure 5. 15

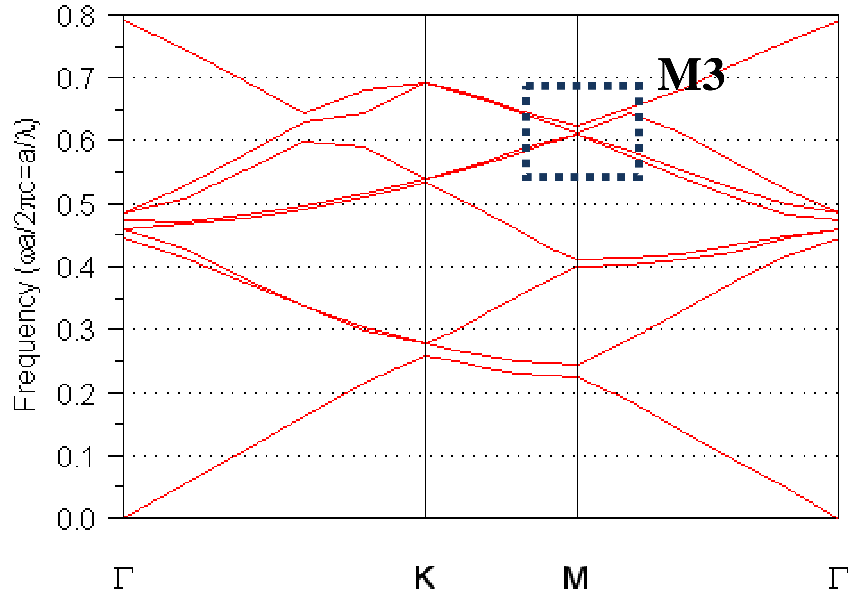

Figure 5. 15 Dispersion curve for TE like mode for M3 case

For the band-edge M3 mode, there are four cavity mode frequencies. The cavity mode frequency can be obtained via simple transform of the normalized frequency which derived from R-soft. The normalized frequency values from lower to higher are 0.60898, 0.60943, 0.61409, and 0.62335. Once the cavity mode frequency at the individual band-edges can be obtained, we can derive the coupling coefficients κ_1, κ_2, and κ_3 from Eq. (4. 50) and its values are 1241 cm^{-1},1356 cm^{-1} and 2683 cm^{-1}, respectively. Therefore, we know the lasing oscillation back and forth provided the major significant contribution to support the lasing action.

The threshold gain is determined by two factors, one is the gain medium and the other is coupling coefficient. It is expected that the lasing action occurs at Γ1 band edge should have the lowest threshold gain due to the largest coupling coefficient. Therefore, we analyze the threshold gain of PCSELs with its r/a, ranges from 0.25 to 0.26, as a function of normalized frequency as shown in Figure 5. 16. It is obvious to see the Γ1 indeed has the lowest threshold gain and M3 has highest threshold gain which is corresponding to our expectation. In the future, for the electrical pump PCSELs fabrication, one can follow this rule and design for Γ1 group to achieve lasing action.

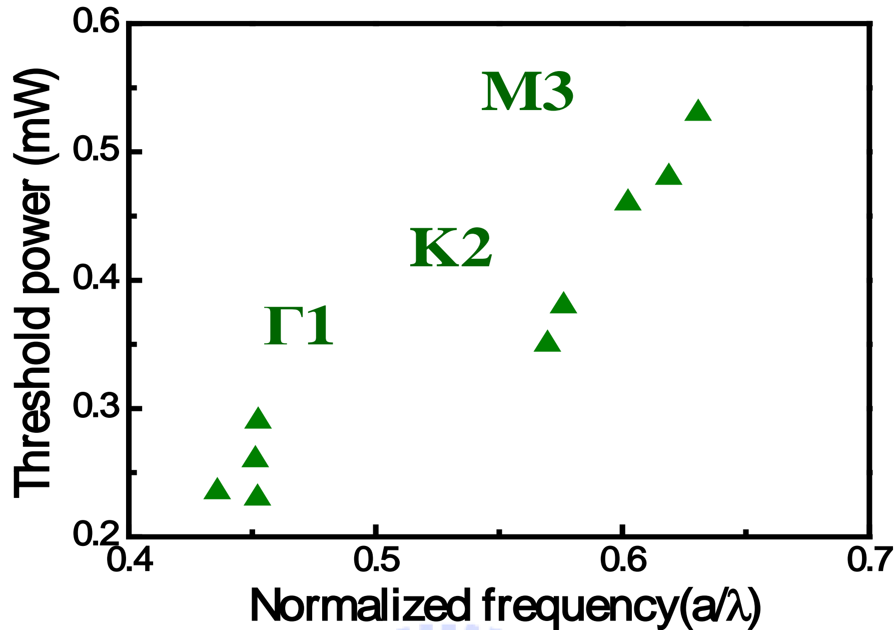

Figure 5. 16 The threshold power versus normalized frequency for Γ1 K2 M3 groups

The normalized frequencies as a function of *r*/*a* ratio were plotted as square points in Figure 5. 17. On the other hand, we apply the plane-wave expansion method in two-dimensions with an effective index model considering the effects of partial modal overlap of electromagnetic fields with the PhC structures to calculate the band diagram of the hexagonal PhC patterns in this structure[7]. The solid (black), dot (red), and dash (green) lines are the calculated band edge frequencies at the Γ, K, and M Brillouin-zone boundaries as a function of *r*/*a* ratio, which were in accordance with the measured results.

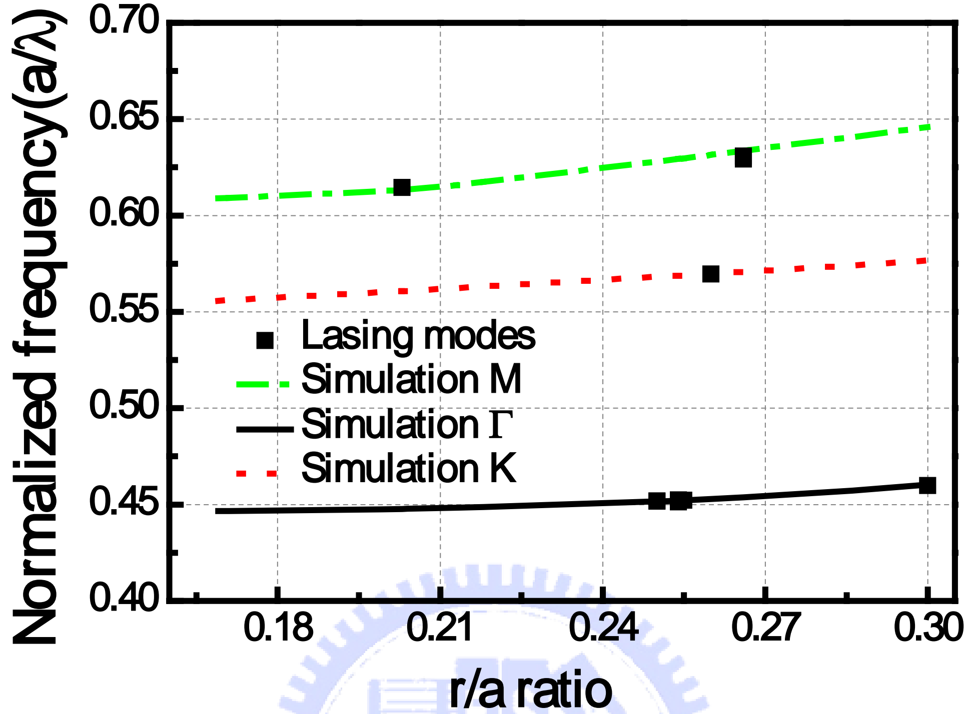

Figure 5. 17 Normalized frequency verses *r*/*a* ratios. The solid, dot, and dash lines represent the simulation results of Γ, K, and M lasing groups by PWEM. The square points, inserted in the diagram, present the experiment results mapped and compared with the simulation results.

5-3 Polarization characteristics at different band edge modes

In this section, we will discuss the characteristics of GaN-based PCSELs and demonstrate the specific lasing characteristics at different band edges: Γ, K, and M points calculated by using the plane-wave expansion method. The lasing modes corresponding to the different points of Brillouin-zone boundary can be confirmed by the polarization directions of the laser emissions.

<u>Polarization</u>

The measured polarization curves for different band edge lasers grouped into Γ(circle points and solid line), K(triangle points and dot line), and M(square points and dash line) boundaries calculated by the PWEM are shown in Figure 5. 18(a) and the

degree of polarization from the emission defined as $(I_{max}-I_{min})/(I_{max}+I_{min})$ was somehow around 50%. The polarization angles from the emissions of devices with different normalized frequencies grouped into Γ, K or M band edge lasers were different. Since the photonic crystal lattices provide the optical feedback, which is the origin of the band edge laser operation, the direction and the polarization of the laser light will strictly follow the photonic crystal lattice vectors. The symmetric feedback directions provided by the 2-D lattice vectors could result in a relatively low degree of polarization if the measurement of the polarization is from the top of the device [8]. As a result, it should be rather difficult to distinguish the specific polarization directions in PCSELs when they are categorized as Γ, K or M band edge lasers. However, the feedback beams could not be equally diffracted by photonic crystal lattices probably due to some disorders or imperfections in the structure. This will result in some beams diffracted in specific directions having higher intensity. The ideally symmetric polarization directions will also be broken. The main polarization directions and the main diffracted laser beams, which are normal to the main polarization directions, can be drawn in a K-space map corresponding to our hexagonal PhC lattice as shown in Figure 5. 18(b). These main diffracted laser beams, shown as dash lines in Figure 5. 18(b), point exactly to the Γ(solid line), K(dot line) and M(dash line) boundaries. The distinct polarization directions provide solid evidence that the lasing actions of our photonic crystal laser originate from different band edges.

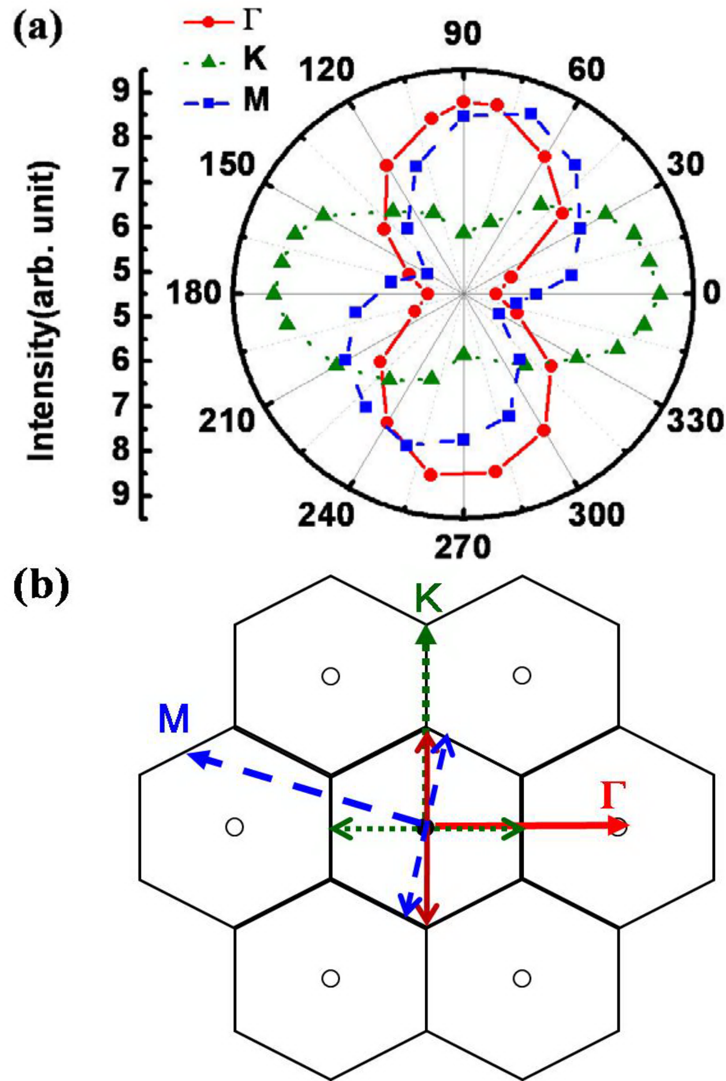

Figure 5. 18 (a) The measured polarization curves for different band edge lasers grouped into Γ(circle points and solid line), K(triangle points and dot line), and M(square points and dash line) boundaries calculated by the plane-wave expansion method. (b) The main polarization directions obtained in (a) and their corresponding diffracted laser beams, which are normal to the polarization directions in a K-space map corresponding to our hexagonal PhC lattice.

5-4 Angular-resolved optical characteristics at different band-edge modes

Data normalization

We set up a rotational stage just under the sample stage to measure the light field distribution which emitted by PCSELs. In this way, the rotation center would match the sample center roughly. We have a detected arm connected the rotational stage and the fiber detector. Rotating the rotational stage, the fiber could collect PL spectrum at different angle. Therefore, we have a series of PL spectra distributed in continuous space, we named these spectra as "angle-resolved μ-PL" (AR μ-PL).

After measurements, we transformed the AR μ-PL spectrum to obtain the guided modes dispersion relation (reduced frequency $u=\Lambda/\lambda_0$ as y-axis versus in-plane wave vector, $k_{//}$, as x-axis), by using the relation $k_{//}= k_0*sin\theta$. In addition, each wavelength, $I_{PL}(\tilde{o})$, is normalized relative to its integrated intensity[9]. The normalized AR μ-PL diagram reveals the clear dispersion relation of guided modes and figures out the detail information about the relative excitation and out-coupling efficiency.

AR μ-PL diagram

Figure 5. 19 shows the measured dispersion diagram at Γ1 mode pumped by the YVO_4 pulse laser and pumped by the He-Cd laser. The dash lines represent the simulated photonic band diagram around Γ1 mode. Since YVO_4 pulse laser has a higher pumping energy intensity, which can overpass the threshold of the stimulated emission provided by the PhC in-plane resonance routes to observe the lasing phenomenon from the devices in Figure 5. 19(a), it can be clearly seen that the PC laser shows the vertical emission near the normal direction to the sample surface. However, except for the lasing peaks, the diffracted lines in this figure cannot be observed clearly due to high intensity of laser peaks. Alternatively, we used a CW He-Cd laser which has a constant average power but a lower pumping intensity to collect diffracted emissions from our PCSEL structures. So the diffracted pattern can be more clearly revealed in the measured dispersion diagram shown in Figure 5. 19(b). It should be noted that the transverse upward curving lines (indicated by black arrows in Figure 5. 19(b)) are resulted from the Fabry-Perot effect provided by the vertical device structure of the p-/n-GaN layers and modulated by the

interference of the DBR layers. Besides, the obvious diffraction lines can be observed with narrow line widths in the measured dispersion diagram, which are resulted from the in-plane PhC diffraction. In order to explain the observed diffraction patterns caused by a PhC, particular for the guided modes in devices, the electric field propagating in the PhC structure could be described as a Bloch mode: $E(r) = \Sigma_{\boldsymbol{G}} E_{\boldsymbol{G}} \times \exp\,[i(k_{//} + G) \bullet r]$, where $E_{\boldsymbol{G}}$ is the electric field component corresponding to harmonic reciprocal lattice vector G, and $k_{//}$ is the in-plane wave vector of the Bloch mode. In our PhC structure, the reciprocal lattice in K space is a 2-D hexagonal lattice rotated by 30° with respect to the direct lattice in real space and reciprocal lattice vectors can be written as: $G = q_1K_1 + q_2K_2$, where q_1 and q_2 are integers, and K_1 and K_2 are the two reciprocal lattice basis vectors. Harmonics of the Bloch mode are extracted if their in-plane wave vectors are within the light cone: $|k_{//} + G| < k_0$, where k_0 is defined as $2\pi/a$.

In Figure 5. 19(b), we can observe several groups with different slopes of diffraction lines in the dispersion diagram. The diffraction lines with different slopes represent different dispersion modes, which can be well matched to calculated dispersion curves shown as dashed lines. The parallel diffraction lines with the same slope represent different guide modes in the in-plane direction. Since the lasing peak will occur near the Γ1 band edge, by comparing between Figure 5. 19(a) and Figure 5. 19(b), the lasing actually occurs at the third guided mode. It's interesting to note that instead of lasing at the fundamental guided mode, the third guided mode may benefit from the lower scattering loss resulted from the rough interfaces at the PhC hole boundaries in this PCSEL device. On the other hand, though several band edges would appear in the calculated dispersion curves as shown in Figure 5. 19(a), only one dominant lasing peak was observed at the second lowest band edge mode and one small peak was observed at the lowest band edge mode.

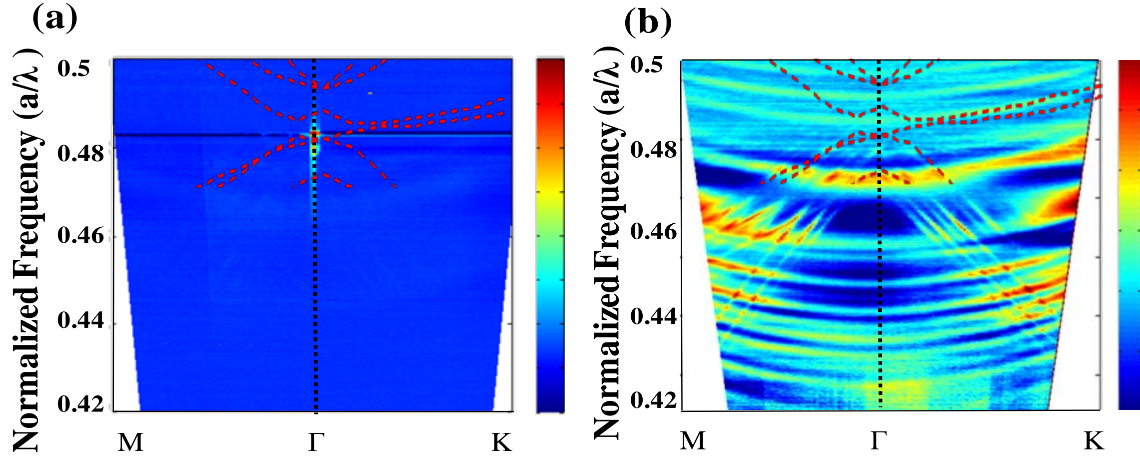

Figure 5. 19 The measured AR-PL diagram near the Γ1 mode ((a) pumped by YVO_4 pulse laser; (b) pumped by He-Cd laser), the dash lines represent the calculated photonic band dispersion curves.

If we enlarge the calculated dispersion curves near the Γ1 band edge as shown in Figure 5. 20(a), the different Γ1 band edges will correspond to different field distribution patterns in one unit cell. The magnetic field in one unit cell for each Γ1 mode was simulated and shown in Figure 5. 20(b). The orange dash circle indicates the PhC air hole and blue and green areas correspond to positive and negative magnetic fields perpendicular to the plane. Since the PhC air holes were etched through the MQW region in this PCSEL device, the optical gain did not exist in the PhC air holes. As a result, we can only observe the two lowest Γ1 band edge modes, for which the magnetic fields cover larger gain regions in the PCSEL structures in comparison to the two higher order Γ1 band edge modes, which the magnetic fields locate mostly in air hole region with no optical gain at all, as shown in Figure 5. 20(b).

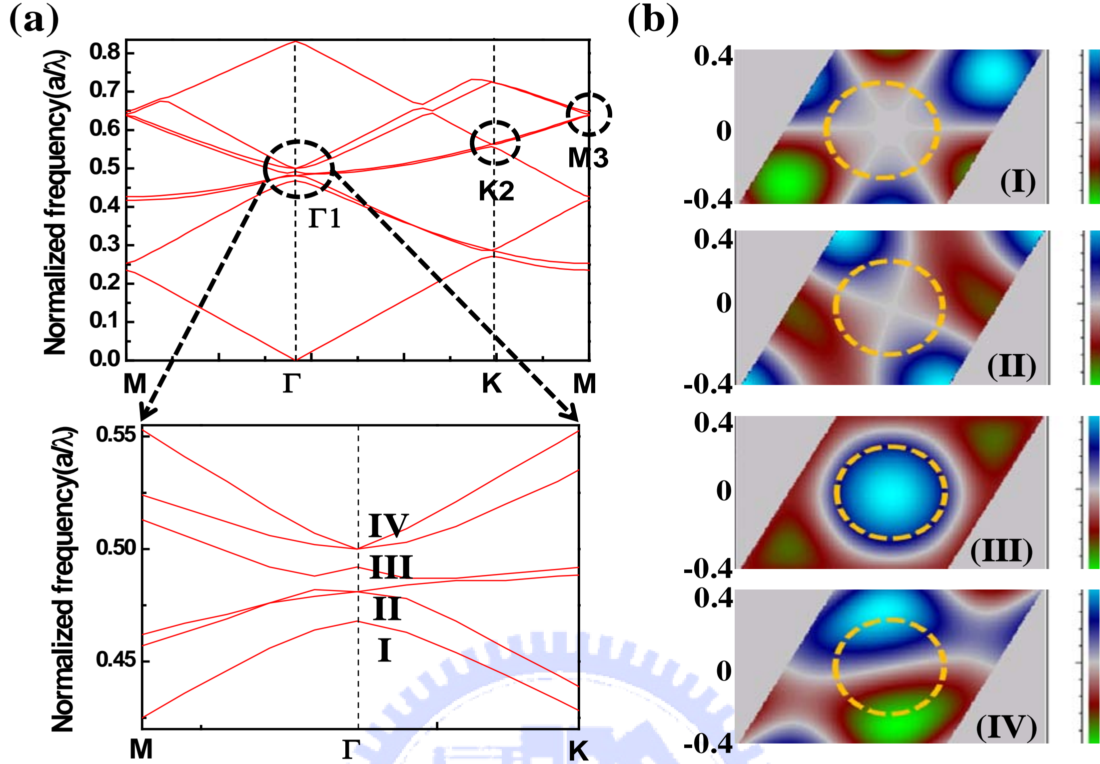

Figure 5. 20(a) The enlarged dispersion curves near the Γ1 band edge. Labels (I) to (IV) correspond to four different Γ1 band edge modes. (b) (I)-(IV) are the magnetic field distributions in one unit cell for the band edge modes labeled in (a). Blue and green areas represent positive and negative magnetic fields perpendicular to the plane. dash circles indicate the PhC air holes.

Figure 5. 21 show the measured AR-PL diagrams of another PCSEL device with different PC structure near the K2 modes along the Γ-K direction. Fig. 7(a) shows lasing peaks in the ARPL diagram by using YVO4 pulse laser pumping. In addition, the AR-PL diagram in Figure 5. 21(b) was obtained by using CW He-Cd laser pumping. Except for the upward curving lines, the diffracted lines can be observed and well matched to the calculated 2-D TE-like photonic band diagram shown as the dash lines in Figure 5. 21, by using parameters of r/a = 0.285, a = 210 nm, n_b = 2.560, n_a = 2.343, and n_{eff} = 2.498 for calculation. In addition, the emission angle of lasing beam was about 29 degree off from the normal along the Γ-K direction, which was quite matched to the estimated value (30

degree) derived in the previous section. Finally, we measured another PCSEL device exhibited characteristics of M3 band edge mode along the Γ-M direction. The measured dispersion diagrams pumped by YVO_4 pulse laser and by He-Cd laser are shown in Figure 5. 22(a) and (b), respectively. The lasing peaks can be clearly seen in Figure 5. 22(a). The diffracted patterns can be observed in Figure 5. 22(b) and well matched to the calculated 2-D TE-like photonic band diagram shown as the dash lines in Figs. 8, by using parameters of r/a = 0.204, a = 230 nm, n_b = 2.617, n_a = 1.767, and n_{eff} = 2.498. The emission angle of lasing beam was about 59.5 degree off from the normal along the Γ-K direction, which was also quite matched to one of the estimated values (61.87 degree) derived in the previous section. The reason only one emission angle was obtained could be due to that we only measured the AR-PL diagram alone one Γ-M direction.

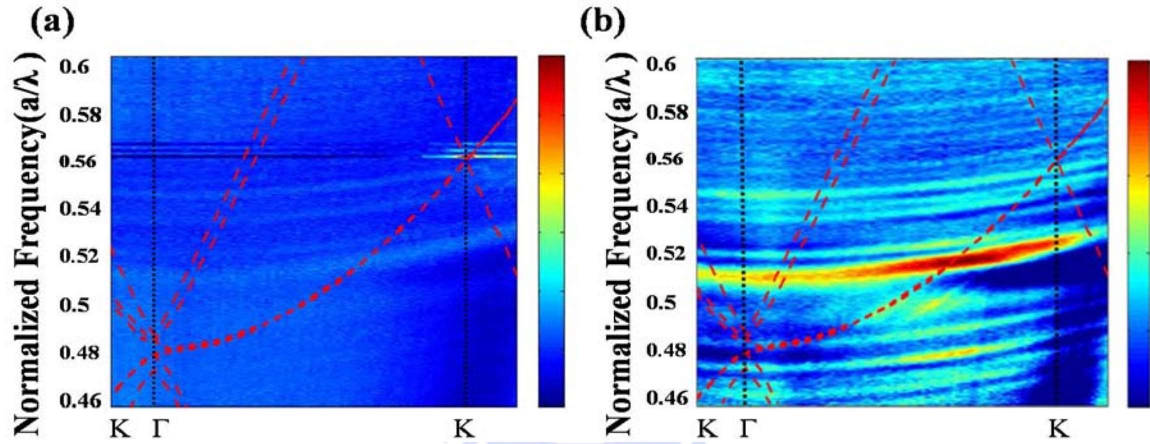

Figure 5. 21 The measured AR-PL diagram near the K2 mode ((a) pumped by YVO_4 pulse laser; (b) pumped by He-Cd laser). The dash lines represent the calculated photonic band dispersion curves.

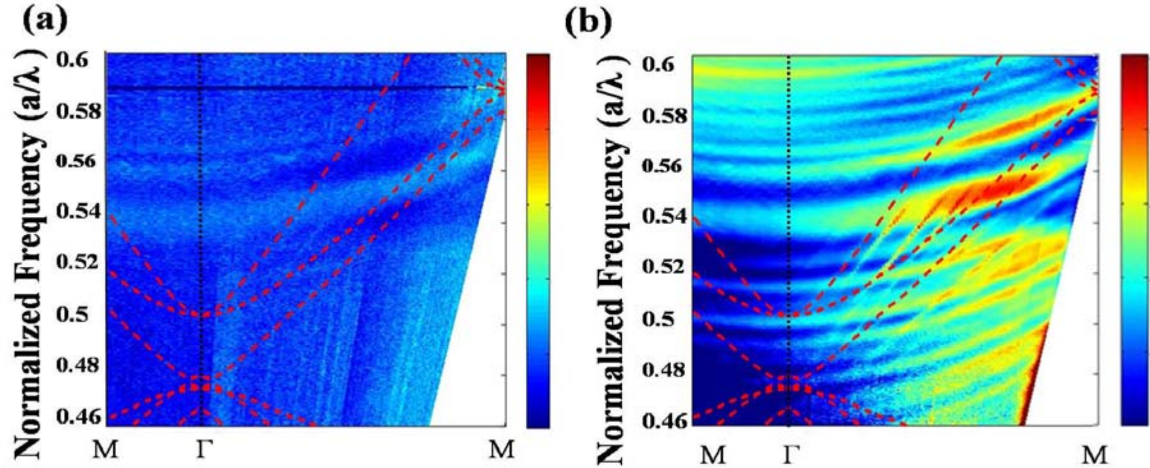

Figure 5. 22 The measured AR-PL diagram near the M3 mode ((a) pumped by YVO_4 pulse laser; (b) pumped by He-Cd laser). The dash lines represent the calculated photonic band dispersion curves.

From Figure 5. 19(a), Figure 5. 21(a), and Figure 5. 22(a), each of PhC band-edge modes exhibited specific emission angle by different type of wave coupling mechanism. Figure 5. 23 shows the divergence angles of Γ1, K2, and M3 band-edge modes on the normal plane from the sample surface despite the measurements were along different directions. The lasing emission angles are (0˚, 29˚, 59.5˚) and the divergence angles of laser beams are (1.2˚, 2.5˚, 2.2˚) for (Γ1, K2, M3) band edge modes, respectively. It should be noted that the measured emission angles might have some offset values (about 1˚ to 2˚) due to the alignment difficulties in the AR-PL system. However, from the above observation of our PCSEL devices, not only the higher band edge modes were determined but their characteristics can be properly matched to the Bragg diffraction mechanism in 2-D PhC structure.

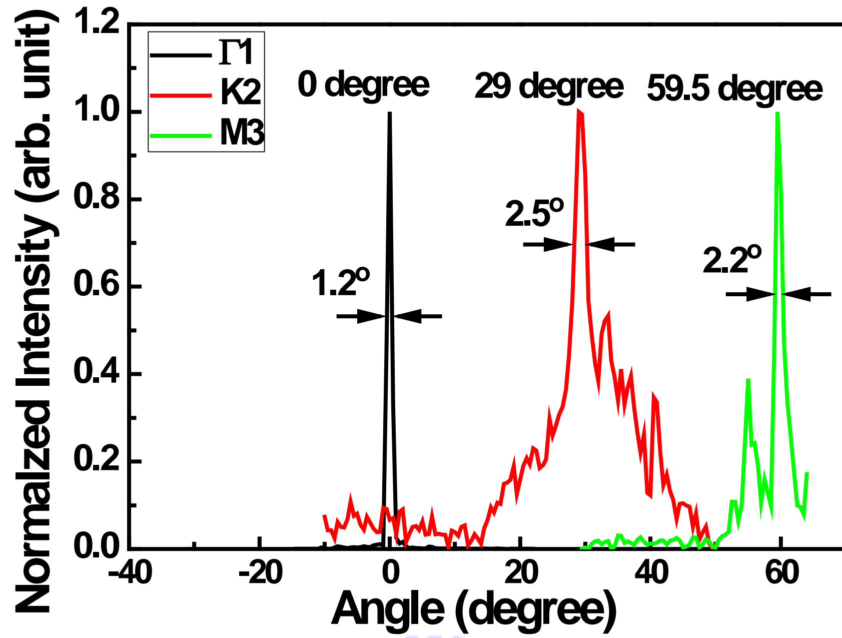

Figure 5. 23 The emission angles and divergence angles of Γ1, K2, and M3 band-edge modes on the normal plane from the sample surface.

References.

[1] M. Imada, A. Chutinan, S. Noda, and M. Mochizuki, *Phys. Rev. B,* **65**, 195306, (2002)

[2] M. Notomia, H. Suzuki, and T. Tamamura, *Appl. Phys. Lett.*, **78**, 1325, (2001)

[3]S. W. Chen, T. C. Lu, and T. T. Kao, *IEEE J. Selected Topics in Q. Elec.*, **15**, 885 (2009)

[4] S. C. Wang, T. C. Lu, C. C. Kao, J. T. Chu, G. S. Huang, H. C. Kuo, S. W. Chen, T. T. Kao, J. R. Chen, and L. F. Lin, *Jpn. J. Appl. Phys.*, **46**, 5397, (2007)

[5] T. Tawara, H. Gotoh, T. Akasaka, N. Kobayashi, and T. Saitoh, *Appl. Phys. Lett.*, **83**, 830 (2003)

[6] C. Skierbiszewski, P. Perlin, I. Grzegory, Z. R. Wasilewski, M. Siekacz, A. Feduniewicz, P. Wisniewski, J. Borysiuk, P. Prystawko, G. Kamler, T. Suski, and S. Porowski, *Semicond. Sci. Technol*., **20**, 809 (2005)

[7] T. C. Lu, S. W. Chen, L. F. Lin, T. T. Kao, C. C. Kao, P. Yu, H. C. Kuo, and S. C. Wang, *Appl. Phys. Lett*, **92**, 011129 (2007)

[8] H. Y. Ryu, S. H. Kwon, Y. J. Lee, Y. H. Lee, and J. S. Kim, *Appl. Phys. Lett.* **80**, 3476(2002)

[9] F. S. Diana, A. David, I. Meinel, R. Sharma, C. Weisbuch, S. Nakamura, and P. M. Petroff, *Nano Lett.* **6**, 1116 (2006)

Chapter 6
Conclusion and Future Work

6.1 Conclusion

In the thesis, we have demonstrated the CW current operation of GaN-based vertical cavity surface emitting lasers (VCSEL) with hybrid mirrors at room temperature and the optical pumped GaN-based photonic crystal surface emitting lasers (PCSEL) with AlN/GaN distributed Bragg reflectors. Therefore, we will summarize the works contributed from the research.

First, we have demonstrated the CW RT operation of GaN-based vertical cavity surface emitting lasers with hybrid mirrors. The laser structure is composed of a 29-pair high-reflectivity AlN/GaN bottom DBR (99.3 %), a 7-lamda cavity region, a transparent conduct layer (ITO), and a 10-pair SiO_2/Ta_2O_5 dielectric DBR (99%). Among of the structure, the laser has a thin Indium-Tin-Oxide layer of 30 nm as the transparent conducting layer combining with a thin heavily doped p-type InGaN contact layer to reduce the optical loss while maintaining good current spreading capability. An AlGaN electric blocking layer on the top of the InGaN multiple quantum well is also inserted to prevent the carrier overflow. At 300 K, the quality factors of VCSEL devices with 30 nm ITO layer are about 1600 below threshold current, lower than the devices without ITO layer of about 1900, but higher than the devices with 210 nm ITO layer of about 700 due to the optical absorption in ITO layer. Above threshold current, the laser has a threshold current at 9.7 mA corresponding to 12.4 kA/cm^2. The laser emission wavelength is 412 nm with a linewidth of about 0.5 nm. The laser has an estimated spontaneous emission coupling factor of about 5×10^{-3} . The degree of polarization, and divergence angle of the laser are measured to be 55 % and 8 degree, respectively. Furthermore, the laser device has better electrical characterisitics such as the series resistance of about 180 Ω, roll over current density of about 13 kA/cm^2, and damage current density of about 43 kA/cm^2.

Second, the optical pumped of GaN-based 2-D photonic crystal surface emitting lasers are fabricated. The laser has a 29-pair bottom distributed Bragg reflectors plays the role of a low refractive index layer to enhance the coupling between photonic crystal nanostructure and electrical field in the whole cavity. Therefore, the lasing action is

achieved under the optical pumping system. Each of these laser devices emits only one dominant wavelength between 395 nm and 425 nm. Normalized frequency of PhC lasing wavelength can be well matched to these three band-edge frequencies (Γ1, K2, M3) indicated the lasing action can only occur at specific band-edges. Polarization directions can further confirm the existence of lasing modes. These three band-edge frequencies (Γ1, K2, M3) has different emission angles in the normal direction (0°, 29°, 59.5°) measured by angular-resolved μ-PL system and further confirmed by the Bragg theory. The divergence angles of the (Γ1, K2, M3) modes are about (1.2°, 2.5°, 2.2°). Besides, the characteristic temperature and the far field pattern of Γ1 mode are about 148 K and symmetric due to the PhCs' symmetric pattern design.

Moreover, the coupling coefficient at different band-edge (Γ1, K2, M3) can be obtained based on 2-D couple-wave model. The threshold gain at Γ1 is the lowest which corresponds to the highest coupling coefficient. All the experiment results indicate that GaN-based PCSELs could be the highly potential optoelectronic device for the next generation lasers.

6.2 Future work

According to the study of VCSEL in this thesis, there are several works for our group to continue and improve the optical and electrical characteristics. One is the heat dissipation problem due to worse thermal conductivity of p-type GaN and sapphire substrate. If we package the laser devices into TO cans or bond them on heat dissipation substrates, we can avoid large thermal effect to destroy the laser devices. Another one is to get better optical confinement according to large refractive index different. The other one is used better current confined layer to decrease the current density that laser devices use. To solve these problems, we have design the new VCSELs structure shown in Figure 6. 1 and Figure 6. 2. In Figure 6. 1, these isolation layers of lower refractive index, such as the implantation area and the AlN layer, can efficiently upgrade both in the current and optical confinement. Figure 6. 2(a) and (b) show the device OM image and the schematic diagram of VCSEL with double dielectric mirrors.

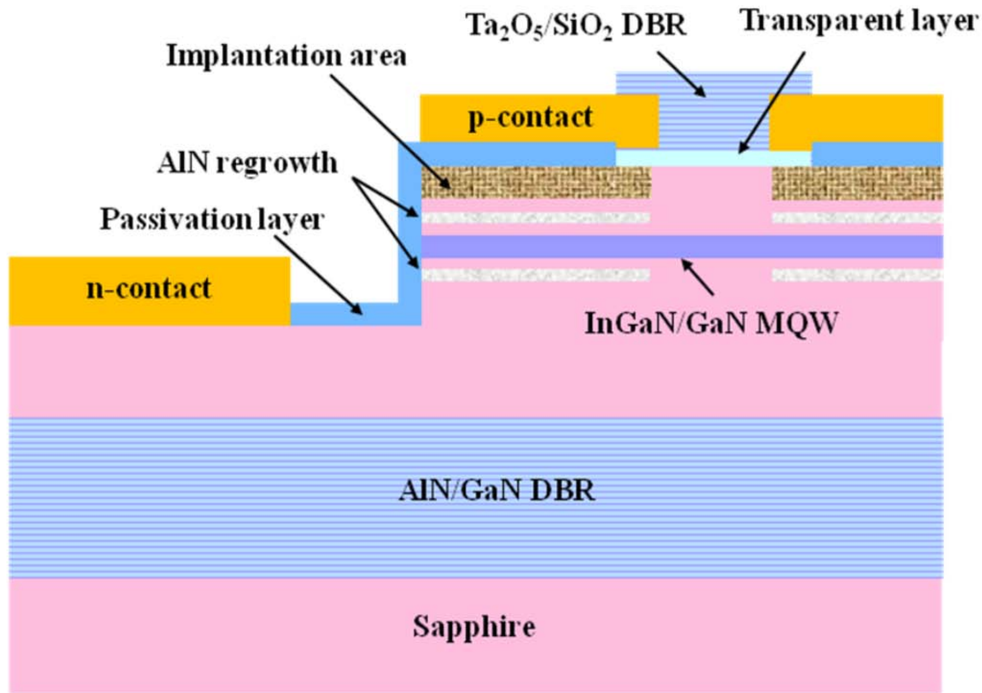

Figure 6. 1 Electrical pumped of GaN-based VCSEL with optical and current confined layer

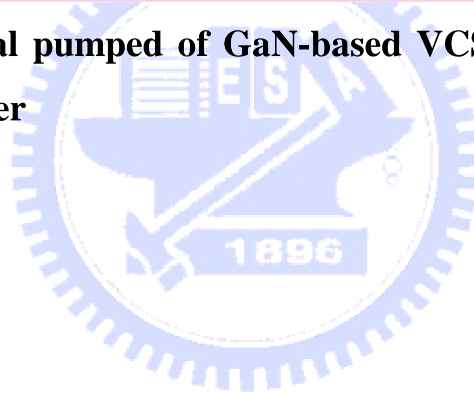

Figure 6. 2 (a) The image for EL GaN-based VCSELs with double dielectric mirrors; (b) the schematic diagram of EL GaN-based VCSELs with double dielectric mirrors.

About PCSEL, We will further improve the fabrication techniques of GaN PCSEL to achieve the better laser operation whether in optical pumped and electrically pumped as shown in Figure 6. 3. In Figure 6. 3(a), the research of GaN-based defect mode PhC

laser becomes a hot topic according to its specific advantages compared with band-edge mode PhC laser. Therefore, we will also investigate the characteristics of GaN-based defect mode PhC laser. Besides, in order to improve the PhC characteristics, we will further fabricate photonic crystal nanostructure on a thin-GaN bonding structure due to the better epitaxial quality and easy to fabricate electrical devices as shown in Figure 6. 4. According to these advantages, we expect these structures can finally reduce the threshold condition for both of VCSEL and PCSEL devices.

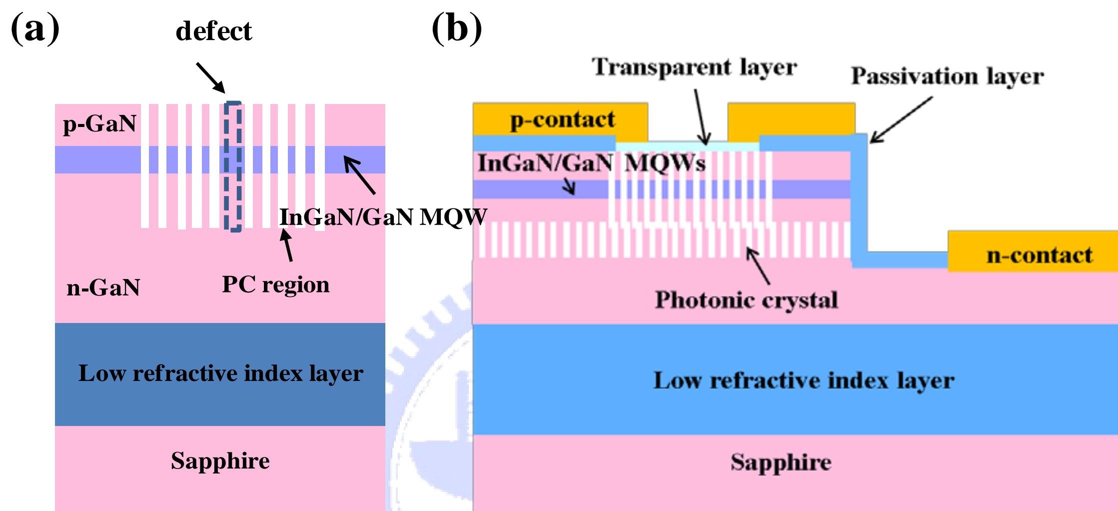

Figure 6. 3 (a) GaN-based photonic crystal defect laser; (b) electrically pumped GaN-based photonic crystal band-edge laser

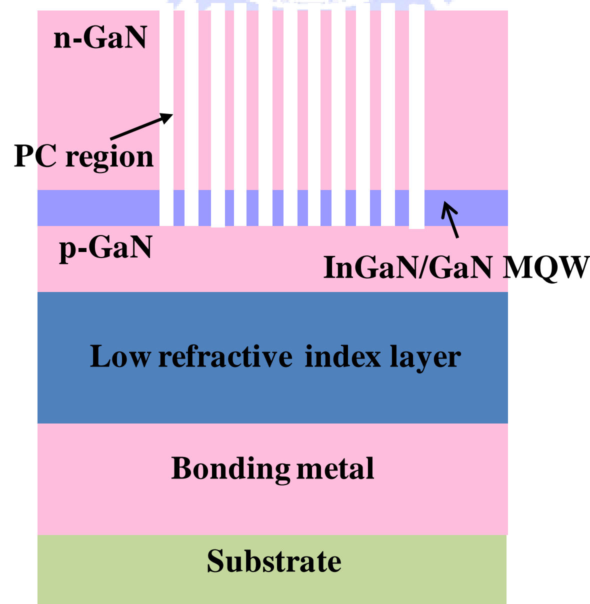

Figure 6. 4 The schematic diagram of thin-GaN PCSEL devices

Publication lists.

International Journal:

1. T. C. Lu**, <u>S. W. Chen</u>**, T. T. Wu, P. M. Tu, C. K. Chen, C. H. Chen, Z. Y. Li, H. C. Kuo, and S. C. Wang, "Continuous wave operation of current injected GaN vertical cavity surface emitting lasers at room temperature", accepted by Appl. Phys. Lett, (2010)
2. **<u>S. W. Chen</u>**, T. C. Lu, Y. J. Hou, T. C. Liu, H. C. Kuo, and S. C. Wang, "Lasing characteristics at different band edges in GaN photonic crystal surface emitting lasers", Appl. Phys. Lett. 96, 071108 (2010)
3. **<u>S. W. Chen</u>**, T. C. Lu, and T. T. Kao, "Study of GaN-based photonic crystal surface-emitting lasers (PCSELs) with AlN/GaN distributed Bragg reflectors", IEEE J. Selected Topics in Qua. Elec., 15, 885 (2009)
4. T. C. Lu, J. R. Chen, **<u>S. W. Chen</u>**, H. C. Kuo, C. C. Kuo, C. C. Lee, and S. C. Wang, "Development of GaN-Based vertical-cavity surface-emitting lasers", IEEE J. Selected Topics in Qua. Elec., 15, 850 (2009)
5. **<u>S. W. Chen</u>**, T. T. Kao, C. C. Kao, J. T. Chu, L. F. Lin, H. W. H., T. C. Lu, H. C. Kuo, and S. C. Wang, "Effects of inhomogeneous gain and loss on nitride-based vertical-cavity surface emitting lasers", Jpn. J. Appl. Phys., 48, 04C127 (2009)
6. Z. Y. Li, M. H. Lo, C. T. Hung, **<u>S. W. Chen</u>**, T. C. Lu, H. C. Kuo, and S. C. Wang, "High quality ultraviolet AlGaN/GaN multiple quantum wells with atomic layer deposition grown AlGaN barriers", Appl. Phys. Lett, 93, 131116 (2008)
7. T. C Lu, **<u>S. W. Chen,</u>** T. T. Kao, T. W. Liu, "Characteristics of GaN-based photonic crystal surface-emitting lasers", Appl. Phys. Lett, 93, 111111 (2008)
8. T. C. Lu, **<u>S. W. Chen</u>**, L. F. Lin, T. T. Kao, C. C. Kao, P. Yu, H. C. Kuo, and S. C. Wang, "GaN-based two-dimensional surface-emitting photonic crystal lasers with AlN/GaN distributed Bragg reflector", Appl. Phys. Lett, 92, 011129 (2008)
9. T. C. Lu, J. T. Chu, **<u>S. W. Chen</u>**, B. S. Cheng, H. C. Kuo, and S. C. Wang, "Lasing behavior, gain property, and strong coupling effects in GaN-based vertical-cavity surface emitting lasers", Jpn. J. Appl. Phys. 47, 6655 (2008)
10. S. C. Wang, T. C. Lu, C. C. Kao, J. T. Chu, G. S. Huang, H. C. Kuo, **<u>S. W. Chen</u>**, T. T. Kao, J. R. Chen, and L. F. Lin, "Optically pumped GaN-based vertical cavity

surface emitting lasers: technology and characteristics", Jpn. J. Appl. Phys. 46, 5397 (2007)

11. J. S. Hwang, Z. S. Hu, T. Y. Lu, L. W. Chen, **S. W. Chen**, T. Y. Lin, C. L. Hsiao, K. H. Chen, and L. C. Chen, "Photo-assisted local oxidation of GaN using an atomic force microscope", Nanotechnology, 17, 3299 (2006)

International Conference:

1. T. C. Lu, **S. W. Chen**, T. T. Wu, C. K. Chen, C. H. Chen, P. M. Tu, Z. Y. Li, H. C. Kuo, and S. C. Wang, "CW current injection of GaN-based vertical cavity surface emitting laser with hybrid mirrors at room temperature". ISLC 2010

2. **S. W. Chen**, T. C. Lu, Y. J. Hou, T. C. Liu, H. C. Kuo, and S. C. Wang, "Angular-resolved lasing characteristics at different band edges in GaN photonic crystal surface emitting lasers", CLEO 2010

3. T. C. Lu, **S. W. Chen**, T. T. Kao, T. C. Liu, C. K. Chen, Y. J. Hou, C. H. Chen, P. S. Weng, Z. Y. Li, H. C. Kuo, and S. C. Wang, "GaN-based two dimensional photonic crystal surface-emitting lasers with AlN/GaN DBR", OPTO/SPIE 2010

4. **S. W. Chen**, T. C. Lu, T. T. Kao, Y. J. Hou, T. C. Liu, P. S. Weng, Z. Y. Li, H. C. Kuo, and S. C. Wang, "The lasing characteristic of GaN-based photonic crystal surface-emitting lasers", MOC 2009

5. **S. W. Chen**, T. T. Kao, Y. J. Hou, P. S. Weng, T. C. Liu, T. W. Liu, T. C. Lu, H. C. Kuo, and S. C. Wang, "Coupled wave model for GaN-based 2-D photonic crystal surface-emitting lasers", SSDM 2009

6. **S. W. Chen**, C. K. Chen, T. T. Kao, C. H. Chen, M. H. Lo, Z. Y. Li, T. C. Lu, H. C. Kuo, and S. C. Wang, "Fabrication of high qualify factor of GaN-based vertical-cavity light emitting diodes with AlN/GaN and Ta2O5/SiO2 hybrid mirrors", SSDM 2009

7. J. S. Hwang, K. Y. Chen, W. S. Syu, **S. W. Chen**, S. J. Hong, H. P.Chiang, S. Chattopadhyay, K. H. Chen, and L. C. Chen, "Silver nano-crystal decorated silica nanowires on quartz as versatile surface-enhanced Raman scattering substrate", CLEO/PR 2009

8. **S. W. Chen**, T. T. Kao, T. C. Lu, H. C. Kuo, S. C. Wang, "Progress of GaN-based

vertical cavity surface emitting lasers", APWS 2009.

9. S. C. Wang, T. C. Lu, H. C. Kuo, **S. W. Chen**, T. T. Kao, "GaN-based vertical cavity surface emitting laser and photonic crystal surface emitting laser", ACP 2009.

10. T. C. Lu, T. T. Kao, **S. W. Chen**, J. R. Chen, C. C. Kao, H. C. Kuo, and S. C. Wang, "Continuous-wave operation of GaN-based vertical cavity surface emitting lasers by current injection", CLEO 2009.

11. **S. W. Chen**, T. T. Kao, T. W. Liu, T. C. Lu, H. C. Kuo, and S. C. Wang, "Lasing characteristics of GaN-based photonic crystal surface-emitting lasers", PR/CLEO 2009.

12. H. C. Kuo, T. C. Lu, **S. W. Chen**, T. T. Kao, Z. Y. Li, and S. C. Wang, "Current injection of GaN-based vertical-cavity surface-emitting lasers at 77K", PR/CLEO 2009.

13. **S. W. Chen**, C. H. Chiu. T. T. Kao, L. F. Lin, T. C. Lu, H. C. Kuo,S. C. Wang, "Light output enhancement of GaN-based photonic crystal LED with AlN/GaN DBR", SSDM 2008.

14. **S. W. Chen**, T. T. Kao, C. C. Kao, J. T. Chu, L. F. Lin, H. W. Huang, T. C. Lu, H. C. Kuo, S. C. Wang, "Effects of inhomogeneous gain and loss on nitride-based vertical cavity surface emitting lasers", SSDM 2008.

15. **S. W. Chen**, T. T. Kao, T. C. Lu , C. C. Kao, L. F. Lin, T. W. Liu, H. C. Kuo, and S. C. Wang," The lasing action of GaN-based two dimensional surface-emitting photonic crystal laser", APOC/SPIE 2008.

16. T. C. Lu, **S. W. Chen**, T. T. Kao, C. C. Kao, L. F. Lin, T. W. Liu, H. C. Kuo, and S. C. Wang, "Performance of GaN-based surface-emitting photonic crystal Laser", IWN 2008.

17. H. C. Kuo, **S. W. Chen**, T. T. Kao, C. C. Kao, J. R. Chen, T. C. Lu, and S. C. Wang, "Blue GaN-based vertical cavity surface emitting lasers by CW current injection at 77K", OPTO/SPIE 2008.

18. T. C. Lu, T. T. Kao, **S. W. Chen**, C. C. Kao, H. C. Kuo, S. C, Wang, "Fabrication and performance of GaN-based two dimensional photonic crystal surface emitting lasers", ISLC/LEOS 2008.

19. T. C. Lu, T. T. Kao, **S. W. Chen**, T. W. Liu, P. Yu, H. C. Kuo, S. C. Wang,

"GaN-based two dimensional photonic crystal surface emitting lasers", CLEO 2008.

20. M. H. Lo, **S. W. Chen**, Z. Y. Li. T. C. Lu, H. C. Kuo and S. C. Wang, "AlGaN/GaN multiple quantum wells grown by atomic layer deposition Lasers", CLEO 2008.

21. T. C. Lu, T. T. Kao, **S. W. Chen**, C. C. Kao, H. C. Kuo, S. C. Wang, "CW lasing of current injection blue GaN-based vertical cavity surface emitting lasers", CLEO 2008.

22. M. H. Lo, **S. W. Chen**, T. C. Lu, H. C. Kuo, S. C. Wang, "Atomic layer deposition of AlGaN/GaN multiple quantum wells by MOCVD", MRS 2008.

Domestic Journal:

1. **S. W. Chen**, B. S. Cheng, T. C. Lu, H. C. Kuo, "Characteristics of GaN-based photonic crystal light emitting diodes and surface-emitting lasers", 第102期光學工程學會季刊

2. **S. W. Chen**, C. K. Chen, T. C. Liu, C. H. Chen, P. S. Weng, Y. J. Hou, T. T. Kao, T. C. Lu, H. C. Kuo, and S. C. Wang, "The development of GaN-based vertical-cavity surface emitting laser", 2009台灣雷射科技應用協會季刊(VOL.6)

Domestic Conference:

1. **S. W. Chen**, G. L. Ku, C. H. Chen, Y. J. Wu, J. S. Hwang, "Broadband anti-reflection of aligned silicon nanowires", Proceedings of Optics and Photonics Taiwan 2006.

2. C. W. Guo, **S. W. Chen**, L. W. Chen, J. S. Hwang, "Growth and application of Germanium Oxide, Silicon Oxide, and Zinc Oxide nanowires", Proceedings of Optics and Photonics Taiwan 2005.

3. **S. W. Chen**, G. L. Ku, C. H. Chen, Y. J. Wu, J. S. Hwang, "Broadband anti-reflection of aligned silicon nanowires", Annual Meeting of the Physical Society of the Republic of China 2006.

4. **S. W. Chen**, Y. J. Wu, J. S. Hwang, "Broadband anti-reflection of aligned silicon nanowires prepared by electroless metal deposition with etching", Taiwan Nano Tech 2006.

5. C. W. Guo, Z. Y. You, **S. W. Chen**, J. S. Hwang, J. H. Lin, T. H. Huang, J. P. Chu, "A simple method for growth of large quantity silica nano-wires", Annual Meeting of the

Physical Society of the Republic of China 2005.

6. **S. W. Chen**, C. C. Kao, K. F. Yeh, J. T. Chu, W. L. Peng, H. W. Huang, T. C. Lu, H. C. Kuo and S. C. Wang, "Characteristics of nano-roughened GaN light-emitting diodes formed by ICP dry etching and laser lift-off technique", Proceedings of Optics and Photonics Taiwan 2007.

7. **S. W. Chen**, J. S. Hwang, S. H. Hsu, Y. J. Cheng, M. H. Lo, C. H. Chiu, H. C. Kuo, T. C. Lu, S. C. Wang, C. C. Kao, L. F. Lin, "Optical characteristic of aligned silicon nanowires", Proceedings of Optics and Photonics Taiwan 2007.

8. M. H. Lo, **S. W. Chen**, T. C. Lu, H. C. Kuo and S. C. Wang, "Atomic layer deposition of AlGaN/GaN multiple quantum wells by MOCVD", Proceedings of Optics and Photonics Taiwan 2008.

9. S. C. Wang, T. C. Lu, H. C. Kuo, **S. W. Chen**, and Tsung-Ting Kao, "CW lasing of current injection blue GaN-based vertical cavity surface emitting laser", Proceedings of Optics and Photonics Taiwan 2008.

10. T. C. Liu, **S. W. Chen**, T. T. Kao, T. W. Liu, T. C. Lu, H. C. Kuo, and S. C. Wang, "Coupled-wave model for GaN-based 2-D photonic crystal surface-emitting lasers", Proceedings of Optics and Photonics Taiwan 2008.

11. **S. W. Chen**, T. W. Liu, T. C. Liu, C. K. Chen, Z. Y. Li ,T. C. Lu, H. C. Kuo, and S. C. Wang, "GaN-based two-dimensional surface-emitting photonic crystal lasers with AlN/GaN distributed Bragg reflector", Proceedings of Optics and Photonics Taiwan 2008.

12. C. K. Chen, **S. W. Chen**, T. C. Liu, L. F. Lin, T. C. Lu, Z. Y. Li ,H. C. Kuo, S. C. Wang, "Light output enhancement of GaN-based photonic crystal LED with AlN/GaN DBR", Proceedings of Optics and Photonics Taiwan 2008.

13. **S. W. Chen**, M. H. Lo, T. T. Kao, C. C. Kao, J. T. Chu., L. F. Lin, H. W. Huang, T. C. Lu, H. C. Kuo, S. C. Wang, C. C. Kuo, and C. C. Lee, "Effects of inhomogeneous gain and loss on nitride-based vertical-cavity surface emitting Lasers", Proceedings of Optics and Photonics Taiwan 2008.

14. M. C. Liu, T. C. Lu, J. T. Chu, **S. W. Chen**, B. S. Cheng, H. C. Kuo, S. C. Wang, "Temperature dependent gain characteristics in GaN-Based vertical-cavity surface-emitting lasers with InGaN multiple quantum wells", Proceedings of Optics

and Photonics Taiwan 2008.

15. J. S. Hwang, K. Y. Chen, W. S. Syu, **S. W. Chen**, S. J. Hong, H. P. Chiang, S. Chattopadhyay, K. H. Chen, L. C. Chen, "Preparation of silver nano-crystal decorated silica nanowires on quartz as versatile surface-enhanced Raman scattering substrates enabling wide range measurement", Proceedings of Optics and Photonics Taiwan 2008.

16. B. S. Cheng, J. T. Chu, **S. W. Chen**, T. C. Lu, H. C. Kuo, S. C. Wang, "Lasing behavior and analysis in GaN-based vertical-cavity surface-emitting lasers", Proceedings of Optics and Photonics Taiwan 2008.

17. **S. W. Chen**, T. C. Lu, L. F Lin, T. T. Kao, C. C. Kao, P. Yu, H. C. Kuo, and S. C. Wang, "GaN-based two-dimensional surface-emitting photonic crystal lasers with AlN/GaN distributed Bragg reflector", Symposium on Nano Device Technology 2008.

18. H. C. Kuo, **S. W. Chen**, T. T. Kao, C. C. Kao, C. H. Chiu, T. C. Liu, M. C. Liu, C. C. Ke, Y. N. He, T. C. Lu, and S. C. Wang, "CW current injection of blue GaN-based vertical cavity surface emitting lasers at 77K", 第 26 屆光譜研討會

19. **S. W. Chen**, T. T. Kao, L. F. Lin, T. C. Lu, C. C. Kao, P. Yu, H. C. Kuo, and S. C. Wang, "GaN-based two-dimensional surface-emitting photonic crystal lasers with AlN/GaN distributed Bragg reflector", Annual Meeting of the Physical Society of the Republic of China 2009.

20. **S. W. Chen**, T. T. Kao, T. W. Liu, K. W. Hsu, T. C. Lu, H. C. Kuo, and S. C. Wang, "Characteristic of GaN-based photonic crystal surface-emitting lasers", Annual Meeting of the Physical Society of the Republic of China 2009.

21. Y. J. Hou, **S. W. Chen**, T. C. Liu, P. S. Weng, C. H. Chen, C. K. Chen, T. T. Kao, T. C. Lu, H. C. Kuo, Shing-Chung Wang, "The angled resolved study of GaN-based 2-D photonic crystal surface emitting lasers", Proceedings of Optics and Photonics Taiwan 2009.

22. C. H. Chen, **S. W. Chen**, C. K. Chen, P. S. Weng, Y. J. Hou, T. T. Kao, T. C. Lu, H. C. Kuo, and S.C. Wang, "Study of GaN-based VCSELs with different ITO layer structure", Proceedings of Optics and Photonics Taiwan 2009.

Patent:

1. **陳士偉**，盧廷昌，郭浩中，王興宗“利用反射鏡及低折射率層製作光子晶體雷射”(台灣、美國、日本專利申請中)
2. 鄭柏孝，**陳士偉**，邱清華，盧廷昌，郭浩中，王興宗“製作包含透明導電玻璃及無裂縫的氮化鋁/氮化鎵系列反射鏡之可電激發面射型雷射”(台灣、美國、日本專利申請中)